NTNU
Det skapende universitet

# Numeriske beregninger av blodstrømning for diagnostisering av koronarsykdom

En evaluering av én- og tredimensjonal modellering

**Stig Marsteng Nilsen**

Master i produktutvikling og produksjon
Innlevert: juni 2016
Hovedveileder: Leif Rune Hellevik, KT

Norges teknisk-naturvitenskapelige universitet
Institutt for konstruksjonsteknikk

**Department of Structural Engineering**
Faculty of Engineering Science and Technology
**NTNU- Norwegian University of Science and Technology**

ACCESSIBILITY
Open

# MASTER THESIS 2016

| SUBJECT AREA: | DATE: 09.06.16 | NO. OF PAGES: 91 |
|---|---|---|
| Biomechanics | | |

TITLE:

**Numerical Simulations of Blood Flow for Diagnosis of Coronary Artery Disease.**

A Comparison of One- and Three-Dimensional Modeling

BY:

Stig Marsteng Nilsen

SUMMARY:
The main goal of this study has been to investigate methods used for noninvasive diagnosis of ischemia and coronary artery disease.
Numerical simulations have been performed in both one and three dimensions, on geometries obtained from literature as well as from medical images. The overall goal has been to compare the feasibility of one and three-dimensional modeling for various stenotic cases.

For low to moderate Reynolds' numbers, and smooth geometrical transitions, a one-dimensional approach showed acceptable results, with a computational efficiency superior to the 3D CFD simulations. For sharper and more severe stenoses, giving Reynolds' numbers above 500 or more than 50 % reduction of the artery diameter, the pure one-dimensional model failed to capture the pressure loss.

Including a lumped model to the one-dimensional code, using simple geometric features as parameters, improved the pressure correction significantly. This model was validated on generic constriction geometries, and later demonstrated on two patient-specific vessels reconstructed from CT-images. Using CFD validated with pressure wire measurements as the ground truth, the lumped model predicted the pressure drop measure fractional flow reserve (FFR) within 3 % of the CFD results for 6 of 8 test cases containing flow conditions plausible in CT-FFR diagnosis. For cases with flow unexpected flow rates, the lumped model still outperformed the purely one-dimensional model.

An investigation has also been done on side branches from the coronary arteries, the ones too small to be seen on a regular CT image. The flow is predicted using a corollary from Murray's law. Including models for this unseen outflow may change the FFR value prediction significantly.

SUPERVISOR(S): Leif Rune Hellevik

CARRIED OUT AT: NTNU

NTNU
Det skapende universitet

# MASTERKONTRAKT
## - uttak av masteroppgave

### 1. Studentens personalia

| | |
|---|---|
| Etternavn, fornavn<br>**Nilsen, Stig Marsteng** | Fødselsdato<br>**08. jun 1992** |
| E-post<br>**stigmn@stud.ntnu.no** | Telefon<br>**48035604** |

### 2. Studieopplysninger

| | |
|---|---|
| Fakultet<br>**Fakultet for ingeniørvitenskap og teknologi** | |
| Institutt<br>**Institutt for konstruksjonsteknikk** | |
| Studieprogram<br>**Master i produktutvikling og produksjon** | Studieretning<br>**Industriell mekanikk** |

### 3. Masteroppgave

| | |
|---|---|
| Oppstartsdato<br>**15. jan 2016** | Innleveringsfrist<br>**10. jun 2016** |
| Oppgavens (foreløpige) tittel<br>**Numeriske strømningsberegninger av koronararterier for bestemmelse av FFR fra CT-bilder.** | |
| Oppgavetekst/Problembeskrivelse<br>Master thesis proposal<br>The candidate will work as a collaborator in the newly set FFR-project in cooperation with the university hospital, clinicians and technological researchers.<br>Fractional flow reserve (FFR) is the medical measure for pressure drop over a pathological deficiency in an artery. This is today measured by invasive techniques, by inserting a catheter and a pressure probe. The fluid pressure is measured proximal and distal of the suspected area. The long-term goal of the project is to develop novel methods for accurate predictions of the FFR of patients, using non-invasive methods.<br><br>The candidate will perform numerical investigations on blood flow in the coronary arteries, both on real and idealized geometries, with particular focus on the boundary conditions. The significance of unseen outlets will be investigated both in 1D and in 3D, using open source CFD software. The results will be compared with available results from the literature, and analytical solutions when possible. | |
| Hovedveileder ved institutt<br>**Professor Leif Rune Hellevik** | Medveileder(e) ved institutt |
| Merknader<br>**1 uke ekstra p.g.a påske.** | |

# Preface

This thesis is submitted in partial fulfillment of the degree Master of Science in Mechanical Engineering at Norwegian University of Science and Technology (NTNU). The specialization field is Applied Mechanics, and the thesis is submitted to Department of Structural Engineering. The work has been carried out as a part of the research project "KoronarFlow", a joint project including St. Olav's university hospital and the Division of Biomechanics at Department of Structural Engineering at NTNU.

The working load of the thesis is equivalent to 30 ECTS credits, or one semester (20 weeks) of full time studies.

Trondheim, 09/06-2016

Stig Marsteng Nilsen

# Acknowledgment

I would like to thank my supervisor, professor Leif Rune Hellevik, for introducing me to the to the intriguing field of biomechanics, and for valuable guidance and insightful feedback throughout the work with this thesis. His encouragement for the master students to participate in the "KoronarFlow" project meetings, and to share ideas and results there is also highly appreciated.

Thanks also to Vinzenz Eck, Jacob Sturdy and Fredrik E. Fossan, Phd candidates at the Division of Biomechanics, for exchange of new ideas, and helping me with the STARFiSh modifications. A sincere gratitude is also expressed to the involved clinicians at the St. Olavs university hospital, in particular Anders Tjellaug Bråthen, for patiently answering all novice medical questions and providing the chest scan data used in the study on patient specific geometry.

I would also like to thank my fellow master students at division of biomechanics, Johannes Kløve Kjernlie and Hallvard Moian Nydal, for the great working atmosphere and the fruitful discussions, both in the office and in the lunch breaks.

S.M.N.

# Abstract

The main goal of this study has been to investigate methods used for noninvasive diagnosis of ischemia and coronary artery disease. Numerical simulations have been performed in both one and three dimensions, on geometries obtained from literature as well as from medical images. The overall goal has been to compare the feasibility of one and three-dimensional modeling for various stenotic cases.

For low to moderate Reynolds' numbers, and smooth geometrical transitions, a one-dimensional approach showed acceptable results, with a computational efficiency superior to the 3D CFD simulations. For sharper and more severe stenoses, giving Reynolds' numbers above 500 or more than 50 % reduction of the artery diameter, the pure one-dimensional model failed to capture the pressure loss.

Including a lumped model to the one-dimensional code, using simple geometric features as parameters, improved the pressure correction significantly. This model was validated on generic constriction geometries, and later demonstrated on two patient-specific vessels reconstructed from CT-images. Using CFD validated with pressure wire measurements as the ground truth, the lumped model predicted the pressure drop measure fractional flow reserve (FFR) within 3 % of the CFD results for 6 of 8 test cases containing flow conditions plausible in CT-FFR diagnosis. For cases with flow unexpected flow rates, the lumped model still outperformed the purely one-dimensional model.

An investigation has also been done on side branches from the coronary arteries, the ones too small to be seen on a regular CT image. The flow is predicted using a corollary from Murray's law. Including models for this unseen outflow may change the FFR value prediction significantly.

# Sammendrag

Hovedmålet med oppgaven har vært å undersøke metoder for ikke-invasiv diagnostisering av koronarsykdom. Numeriske strømningsberegninger har blitt gjort i én og tre dimensjoner, på geometri funnet i litteraturen og på pasientspesifikk geometri rekonstruert fra røntgenbilder.

For strømninger med Reynolds' nummer lavere enn 500, for blodårer med langsomme tverrsnittsendringer, kan en ren endimensjonal modell gi gode resultater. For høyere Reynoldstall eller bråere tverssnittsendringer klarer ikke den endimensjonale approksimasjonen å beregne trykktapet korrekt.

Ved å inkludere en empirisk redusert modell for trykktap over stenoser i 1D-koden, ble resultatene markant forbedret, både for generisk geometri og for de reelle koronarteriene som ble analysert i studien. Modellen ble validert mot eksperimentelle data for generisk geometri, og mot trykkwire-målinger for den pasientspesifikke geometrien. For FFR-bestemmelse i koronararteriene ga en hybrid 0D/1D modell verdier med mindre enn 3 % avvik fra 3D CFD for 6 av 8 studerte tilfeller.

Undersøkelser ble også gjort på lekkasjer fra koronararterier, til små arterioler for små til å bli fanget opp på et CT-bilde. Ved å bruke en antakelse fra Murrays lov og monoton regresjon ble det estimert et volumetrisk tap til sidegrener på over halvparten av den innkomne strømningsraten.

# Contents

# List of Figures

# List of Tables

# Abbreviations

**CAD** Coronary artery disease

**CA** Coronary angiography

**CFD** Computational fluid dynamics

**CFL** Courant-number

**CT** Computed tomography

**CX** Circumflex coronary artery

**FFR** Fractional flow reserve

**FPR** Filtered back projection

**IR** Iterative reconstruction

**LAD** Left anterior descending coronary artery

**NPV** Negative predictive value

**OF** OpenFOAM

**PCI** Percutaneous coronary intervention

**PPV** Positive predictive value

**QCA** Quantitative coronary angiography

**RCA** Right coronary artery

**Re** Reynolds' number

**RoCA** Rotational coronary angiography

**SF** STARFiSh

**TAG** Transluminal attenuation gradient

**TIMI** Thrombolysis in myocardial infarction

**CT-FFR** Fractional flow reserve computed from CT

# Nomenclature

## Greek letters

| | |
|---|---|
| $\alpha$ | Momentum correction factor |
| $\delta$ | Plaque height from blood vessel wall |
| $\Phi(\gamma)$ | Velocity shape function |
| $\Phi(\mathbf{x}, t)$ | Level set surface function |
| $\gamma$ | Velocity profile shape parameter |
| $\mu$ | Kinematic viscosity ($kg/ms$) |
| $\nu$ | Dynamic viscosity ($m^2/s$) |
| $\rho$ | Mass density ($kg/m^3$) |
| $\sigma$ | Normal stress ($Pa$) |
| $\theta$ | Angular coordinate |
| $\tau$ | Shear stress ($Pa$) |
| $\omega$ | Characteristic wave variables |

## Subscripts

| | |
|---|---|
| $_0$ | Reference conditions |
| $_d$ | Distal (of lesion) |
| $_i$ | Inlet |
| $_o$ | Outlet |
| $_p$ | Proximal (of lesion) |
| $_R$ | At cylinder wall |
| $_w$ | At wall |

## Roman letters

| | |
|---|---|
| $A$ | Cross sectional area ($m^2$) |
| $C$ | Compliance ($m^2/Pa$) |
| $C_1, C_2$ | Integration constants |
| $c$ | Coefficient for Murray's law |
| $d$ | Pipe diameter |
| $\mathbf{F}$ | System flux vector |
| $I$ | Medical image gray scale intensity |
| $k$ | Darcy's porosity constant |
| $K_v, K_t$ | Empirical constants for pressure loss equation |
| $m$ | Mass ($kg$) |
| $\mathbf{M}$ | System matrix |
| $p$ | Pressure ($Pa$) |
| $r, z$ | Radial and axial coordinate |
| $R$ | Pipe radius |
| $Q$ | Volumetric flow rate ($m^3/s$) |
| $t$ | Time ($s$) |
| $\bar{u}$ | Cross sectional mean axial velocity |
| $\mathbf{u}$ | System variable vector |
| $\hat{\mathbf{u}}$ | Intermediate prediction step of $\mathbf{u}$ |
| $u, v, w$ | Velocity components in cartesian coordinates |
| $u_r, u_\theta, u_z$ | Velocity components in cylindrical coordinates |
| $x,\ y,\ z$ | Spatial coordinates |

# Chapter 1

# Introduction

The aim of this thesis is to investigate numerical simulations as a tool applied for noninvasive diagnostics of coronary artery disease (CAD).

In this chapter, an introduction to the medical background for the thesis is given, along with the common diagnostic measures available in the clinic today. A summary of earlier research in the field follows, before an outline for the rest of the present work is presented.

## 1.1 Coronary Artery Disease

Cardiovascular diseases are the main cause of death in the world [69]. Coronary artery disease (CAD) make up the major part of this group [42]. Accurate diagnosing of severity of the CAD is today expensive and unavailable at local hospitals. Noninvasive diagnosis of severity of CAD would greatly improve survival for a large patient group, and liberate resources for hospitals.

### 1.1.1 Anatomy

The coronary arteries are the arteries that branch out of the aorta immediatly above the aortic valves that separates the aorta from the left ventricle of the heart. This segment is called the proximal aorta. The coronary arteries provide blood to the heart muscles, and can be seen in figure 1.1. Generally, one divide the external coronary arteries into three. The Right Coronary Artery (RCA) runs from the right side of the aorta, and downwards on the outside of the right ventricle. On the left side of the proximal aorta, the Left Coronary Artery (LCA) breaks out. This

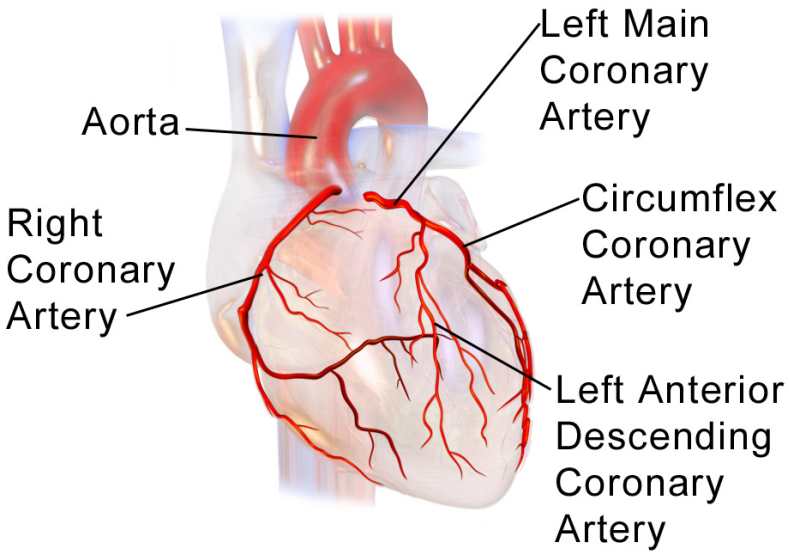


Figure 1.1: Coronary Arteries on hearth. [14]

vessel then splits into the Left Anterior Descending artery (LAD) and the Circumflex Artery (CX). In some humans, the LAD and CX branches directly off the aorta, with no common segment of the LCA. The volume occupied by fluid in blood vessels is called the *lumen*, and the lumen will be the computational domain in the simulations performed in this study.

Thus, 3 main coronary arteries are defined. supplying the hearth with oxygenrich blood. In addition, there exist smaller vessels, called subendocardial vessels, that runs within the myocardium, the heart chamber walls. The blood flow in these arteries is however not sufficient for the hearth's oxygen demand, and we may conclude that the three main coronary arteries are critical for life [8].

### 1.1.2 CAD

Coronary artery disease is a disease causing occlusion of the coronary arteries, making the blood supply to the heart insufficient. This occlusion is due to atherosclerosis and stenosis formation. *Atherosclerosis* is known as the hardening of blood vessels, or the plaque formation inside them. This plaque is made from lipids and particles in the blood flow, depositing along the vessel wall. *Stenosis* describes the reduction of the lumen cross-sectional area of the artery, often caused by

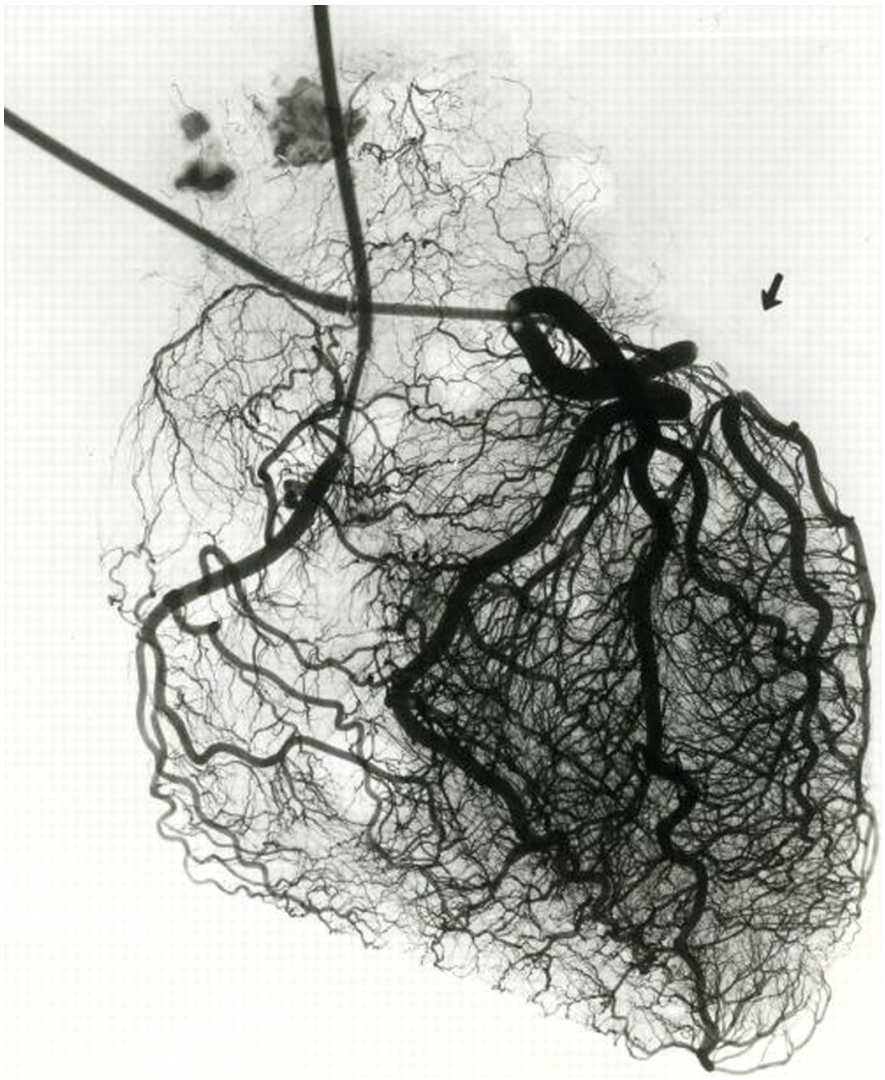

Figure 1.2: Coronary Arteries and arterioles on hearth, acquired with intracoronary injection of contrast agent, known as coronary angiography (CA). Two catheters inserting contrast agent are visible in the upper left corner [6].

atherosclerosis.

Treatment for CAD involves cholesterol lowering drugs, known as statins. Drugs to lower blood pressure or lower the hearth work load is can also be given. Invasive treatment procedures includes stenting, known as percutaneous coronary intervention (PCI) or bypass surgery, both of which are associated with risks.

Accurate diagnistics of CAD is important to give the right treatment to the right patients.

### 1.1.3 Diagnostic Pathway

A few words of today's diagnostic methods are included here to stress the importance of the proposed methods.

Today, CT-scans of the thorax (including the hearth) is performed at low- or low intermediate risk patients. For patients with higher risks, one usually performs invasive angiography or fractional flow reserve (FFR) directly based on *angina*. For the group suitable for CT however, the risks are normally considered to be low, as we are dealing with stable patients.

The CT-images are then inspected by experienced cardiologists. They try to predict the significance of the potential stenoses on the images. This is done by experience in a qualitative way. The cardiologists then suggests invasive angiography or FFR to examine the patients where significant stenosis are suspected.

### 1.1.4 Quantitative Coronary Angiography (QCA) and Fractional Flow Reserve (FFR)

Invasive angiography is carried out by inserting a catheter in the coronary arteries to inject contrast agent with high presicion only in the coronary artery to be studied. Much higher image resolution can then be obtained, and temporal evolution is possible to record. Figure 1.2 is an example of such an image. The clinicians evaluate the significance of the stenosis by visual assessment of how well the contrast agent is transported with the blood flow accross the stenotic region. Terms used to describe healthy coronary arteries include "good filling of the arteries", and "smooth arteries". Efforts have been made to quantify this procedure, and by calibrating images to the cathether with known dimension, accurate measurements of stenosis can

be made. A normal measure for whether a stenosis is significant or not have been set at a 50 % reduction in diameter, which for circular vessels corresponds to a 75 % decrease in lumen cross sectional area.

Unfortunately, the quantitative angiography has not proven to increase specifity in determining risk for ischemia and survivability, compared to the diagnostic performance of Fractional Flow Reserve (FFR) [48]. FFR is a technique where one uses the same catheters as in angiography, but adds a pressure wire which is inserted in the examined artery, downstream of the stenosed region. A pressure measurement is made here and compared to the proximal pressure measured at the catheter in the aortic end, the *ostium* of the artery in question. The FFR measure is computed as:

$$FFR = \frac{p_d}{P_p} \tag{1.1}$$

Where $p_p$ denotes the proximal pressure and $p_d$ the distal pressure. A FFR value below 0.8 is regarded to be a significant stenosis, and is currently the gold standard [47, 60] for predicting which patients will have increased survival rate after invasive treatment such as percutaneous coronary intervention (PCI) or revascularization (by-pass surgery), compared to noninvasive treatment with drugs.

### 1.1.5 Thrombolysis in Myocardial Infarction (TIMI)

In TIMI flow is the ischemia assessed by counting the time frames from the contrast agent is inserted, until the vessel is evenly filled with constrast agent. This is most used for critical patients, as the name infarction implies. The scale is defined to separate totally occluded (grade 1) from partially occluded (grade 2) or non-occluded flow (grade 3), without further refinement of the categories [26].

## 1.2 Non-invasive Prediction of Ischemia

There has been done studies trying to achieve a secure and accurate noninvasive method for determining a patients degree of ischemia. Most attempts have been on predicting the FFR value

from numerical simulations of blood flow, but other approaches have also been investigated.

### 1.2.1 Transluminal Attenuation Gradient

The transluminal attenuation gradient (TAG) method for pedicting ischemia from CT-imaging is based on the temporal aspect in QCA, although only CT-images are used. Here, one tries to extract more than just geometry from the CT-images, but also information about the blood flow rate. The idea is that the constrast agent will transport faster in healthy arteries with higher flow rates, giving a more even reflection, and a more uniform radiodensity, which is measured in Houndsfield units [27], compared with occluded vessels.

The technology has evolved as a result of the development of CT-technology, making CT-machines with more slices, being able to capture the entire coronary system with a single flash of radiation. The foundation was described as early as in 1987 by Wolfkiel et. al. [71] who estimated myocardial blood flow by what they denoted "ultrafast computed tomography". They then used a 16-slice scanner, while scanners today can have 320 or even 640 slices, giving an image quality superior to the smaller scanners [73]. The technique TAG is based on research by Steigner et al [56], who used the radiointensity to predict flow rates in healthy arteries *in vivo* in 2010. Meanwhile Lackner et al. performed an *in vitro* study of flow rate prediction in stenosed arteries. Choi et al [11] were the first to use the gradient for prediction of stenosis severity in 2011. When employing the translumenal attenuation gradient, the radiodensity is sampled along the artery in question. Then a linear regression is performed on the data. The trend is denoted TAG, and takes the unit (HU/10 mm). This will be larger in magnitude for a higher degree of ischemia, indicating a lower blood flow rate. In a comparative study by Wong et al. [72], this technique was compared to both QCA and geometric stenosis evaluation from CT-images, using measured FFR as the gold standard. They found a higher specifity for TAG compared to the geometrical analysis alone, but also a lower sensitivity, meaning a higher positive predictive value (PPV), but a lower negative predictive value (NPV).

Positive predictive value is given as the ratio of true positives to the sum of the true and the false positives from the test prediction, and can be interpreted as the probability that a positive prediction from the text will be a true positive result. In this study both the purely geometrical analysis and TAG outperformed QCA in determining FFR when a 50 % -diameter stenosis (DS)

was considered significant. QCA with a critical value of 70 % DS had higher specificity (82 %) than both TAG and the geometrical analysis.

### 1.2.2 Computational FFR

As FFR stands out as the golden standard for evaluation of hemodynamic significance of stenosis, efforts have been put in to predict this value non-invasively. This is most frequently attempted using a 3D reconstruction of the lumen volume from medical images, and performing computational fluid dynamics (CFD) to compute the FFR.

A research group led by Charlie Taylor at Stanford University has over the past years developed a commercially available CT-FFR software, called HeartFlow, which recieved marketing permission from the United States Food and Drug Administration in November 2013 [21].

The scientific background for this solution was decribed by Taylor et al in 2013 [58]. Their paper demonstrated complex simulations of the entire coronary arterial tree, including the aorta, with lumped models for the boundary conditions. The simulations were run for approximately one hour at a HeartFlow's own cluster.

To evaluate the diagnostic performance, multicenter studies, comparing this computational FFR known as CT-FFR to the invasively measured FFR have been carried out. Studies by Koo et al [35], Min et al [40] and Nørgaard et al [45] played a key role in this approval, and the studies were all partially funded by HeartFlow.

A slightly different approach was taken by Morris et al [41], who in 2013 reported the results of their VIRTU-1 study. They used invasive CT-angiography as a basis for numerical simulations of patients. This gives higher image resulutions, but not a real 3D image aquisition, and a 3D reconstruction must be performed from at least two orthogonal planes, giving a source to geometric errors. Still, the reported diagnostic results were good, with a sensitivity and specifity of 86 % and 100 % respectively.

In the last two years, studies presenting on-site computational FFR predictions were published by Coenen et al [12], Renker et al [50] and DeGeer et al [17]. Their software was developed by Siemens, but is not yet commercially available An advantage for the on-site methods is that patient sensitive data does not have to be transferred outside the hospital, but, as more simplifications must be made, the overall diagnostic performance can be limited, especially with a

Table 1.1: A comparison of diagnostic performance for different noninvasive FFR prediction studies. All studies uses measured FFR as the gold standard. ([a] HeartFlow remote software. [b] on-site Siemens software.)

| Year | 1st Author | Technique | No. of. lesions | Accuracy (%) | Sensitivity (%) | Specificity (%) | PPV (%) | NPV (%) |
|---|---|---|---|---|---|---|---|---|
| 2011 | Koo | CT + CFD [a] | 159 | 84 | 88 | 82 | 74 | 92 |
| 2012 | Min | CT + CFD [a] | 252 | - | 73 | 90 | 54 | 67 |
| 2013 | Morris | RoCA + CFD | 35 | 97 | 86 | 100 | 100 | 97 |
| 2013 | Wong | TAG | 78 | - | 77 | 74 | 67 | 83 |
| 2014 | Nørgaard | CT + CFD[a] | 254 | - | 86 | 79 | - | - |
| 2014 | Renker | CT+ CFD[b] | 67 | - | 85 | 85 | 71 | 93 |
| 2014 | Coenen | Ct + CFD[b] | 189 | 75 | 88 | 65 | - | - |
| 2014 | DeGeer | CT + CFD[b] | 23 | 78 | 83 | 76 | 56 | 93 |

lower specificity, as seen from the review table 1.1. This means that a relatively large fraction of false positives will be passed on to treatment or further diagnostic activities.

Recently, a review published by Secchi et al [53] gives an overview of the current standing of CT-FFR, and Deng et al [18] pooled together results from all available studies up to August 2014, and reported a pooled sensitivity and specificity of 90 % and 72 % respectively, on a per patient level. Per vessel, the pooled sensitivity was 83 % and the pooled specificity 78 %.

Although the CT-FFR has made huge progress in the past few years, there exist challenges not yet fully overcome. The need for off site supercomputers in HeartFlow's solution, or the relatively low specificity of the Siemens solution.

The results reported by Morris et al are remarkably good, but as they used invasive rotational angiography as their image source, it is not feasible to use their protocol for screening of large patient groups. This is due to the resources necessary for invasive angiography, and the increased radiation doses associated with this procedure.

Thus, in this thesis, an investigation will be made on how to make the computed FFR values more accurate with the basis in CT images, that is, how to compute the pressure loss in various pipe-resembling geometries, with constrictions of varying severity.

## 1.3 Hyperemic Flow Conditions

The severity of a stenosis in the coronary arteries gets higher with increased blood flow to the heart, for instance with physical exercise. It is desirable to measure the FFR at the highest flow rate possible, to resemble "worst case".

However, as the traditional invasive FFR measurements are difficult to perform during heavy physical exercise, drugs are given to obtain higher flow rates. The state of drug-induced flow rate increase is called *hyperemia*. When measuring FFR invasive, patients are given adenosine to increase blood flow. This works by lowering the microcirculatory resistance in the capillaries, increasing flow rate.

A dosis of 140 $\mu g kg^{-1} min^{-1}$ of adenosine given intravenously is regarded to give full hyperemia [70], and is widely accepted as gold standard for FFR assessments [60], although later studies have shown that intracoronary adenosine will give similar effects at much lower doses [37, 34].

Full hyperemia was shown by Wilson to give an increase in blood flow velocity of 4.4 times the resting value (SD=0.9) in normal coronary arteries, while arteries with abnormalities, (ie stenoses or aneurysms) showed an increase in blood flow velocity of 2.9 times the resting value (SD=0.4). Bruyne et al [16] found an increase in mean coronary flow velocity from 0.17 m/s at resting conditions to 0.31 m/s at hyperemia, with a 95 % confidence interval of ± 0.17 m/s, indicating a significant individual variability in vasodilation response, but a mean of below 2 times the resting values. Their results were obtained from patients with a measured FFR of 0.70 ± 0.17.

Studies have also shown that the response to vasodilation will be altered by previous strokes [62].

Knowing the exact flow rate at hyperemia is crucial to determine the correct FFR value. Ideally, a measurement of the flow velocity, using doppler ultrasound or other appropriate techniques would increase the diagnostic performance drastically.

In this study, various flow rates with basis in the resting condition will be simulated, and the results' dependence on these conditions will be discussed.

## 1.4 Outline

In Chapter 2, the governing equations for fluid flow will be presented, and modeling in one, two and three dimensions discussed, with focus on the methodology adopted in this study. Murray's law is presented along with lumped models for stenosis resistances. Image segmentation is then treated briefly.

Chapter 3 contains a comparison of one- and three-dimensional simulations on a generic stenosis under physiological flow conditions, benchmarked against experimental data. A lumped model is added to the one-dimensional simulation framework, and the results discussed.

Then, in Chapter 4, a real coronary artery is analyzed, through segmentation and modeling, and numerical simulations in both one and three dimensions, as well as with the hybrid model derived in Chapter 3.

Chapter 5 will treat the volumetric loss from coronary arteries to coronary arterioles, too small to be seen on CT images of normal quality. Methods for estimating the leaks, and modeling them will be presented. In Chapter 6, a summary of the most important results will be given, and a thorough discussion of the validity, strengths and weaknesses of the applied methodology will be performed.

# Chapter 2

# Theory

In this section, a theoretical foundation is formulated. First, the governing equations are derived for three-dimensional fluid flow problems. Then the special case of pipe flows are treated, both by a two-dimensional model and a one-dimensional model for compliant pipe flow. Afterwards, a selection empirical relations for the field of cardiac circulation is presented, Murray's law and a selection of lumped models for stenosis calculations.

## 2.1 Governing Equations in 3 Dimensions

The governing equations for 3D fluid flow problems are two conservation laws, namely the conservation of mass and of linear momentum. Both conservation laws can be derived from the general Reynolds' transport theorem, named after Osborne Reynolds [51].

Reynold's transport theorem for a generic intensive property $b = \rho\beta$, which have an extensive counterpart $B$ can be written for an arbitrary deforming volume $\Omega = \Omega(t)$ as:

$$\frac{\mathrm{d}}{\mathrm{dt}} \int_{\Omega(t)} b(\mathbf{r}, t)\, \mathrm{d}V = \int_{\Omega(t)} \frac{\partial b(\mathbf{r}, t)}{\partial t}\, \mathrm{d}V + \int_{\partial\Omega(t)} b(\mathbf{r}, t)\, (\mathbf{u} \cdot \mathbf{n})\, \mathrm{d}A \tag{2.1}$$

where $\mathbf{u}$ is the velocity of the control surface $\partial\Omega$ and $\mathbf{n}$ the outward pointing normal vector of the same surface.

### 2.1.1 Continuity

Now letting mass of our volume be the extensive property, with the intensive property $\rho$, we write

$$m = \int_{\Omega(t)} \rho(\mathbf{r}, t)\, \mathrm{d}V \tag{2.2}$$

And by demanding mass to be conserved

$$\dot{m} = \frac{\mathrm{d}}{\mathrm{dt}} m = \frac{\mathrm{d}}{\mathrm{dt}} \int_{\Omega(t)} \rho(\mathbf{r}, t)\, \mathrm{d}V = 0 \tag{2.3}$$

Equation 2.1 can then be rewritten as

$$\dot{m} = \frac{\mathrm{d}}{\mathrm{dt}} \int_{\Omega(t)} \rho(\mathbf{r}, t)\, \mathrm{d}V = \int_{\Omega(t)} \frac{\partial \rho}{\partial t}\, \mathrm{d}V + \int_{\partial\Omega(t)} \rho\, (\mathbf{u} \cdot \mathbf{n})\, \mathrm{d}A \tag{2.4}$$

By using the Gauss theorem on the latter integral in Eq. 2.4, the surface integral is transformed to a volume integral on the form

$$\int_{\partial\Omega(t)} \rho\, (\mathbf{u} \cdot \mathbf{n})\, \mathrm{d}A = \int_{\Omega(t)} \nabla \cdot (\rho \mathbf{u})\, \mathrm{d}V \tag{2.5}$$

Now, the two integrals in Eq. 1 2.4 can be written as one:

$$\dot{m} = \frac{\mathrm{d}}{\mathrm{dt}} \int_{\Omega(t)} \rho(\mathbf{r}, t)\, \mathrm{d}V = \int_{\Omega(t)} \frac{\partial \rho}{\partial t} + \nabla \cdot (\rho \mathbf{u})\, \mathrm{d}V \tag{2.6}$$

For this to hold for an arbitrary volume, the integrand must always be zero, and we get the well known continuity equation

$$\frac{\partial \rho}{\partial t} + \nabla \cdot (\rho \tag{2.7a}$$

$$mathbf{u}) = 0 \tag{2.7b}$$

$$\dot{\rho} + u_{i,i} = 0 \tag{2.7c}$$

$$\frac{\partial \rho}{\partial t} + \frac{\partial u}{\partial x} + \frac{\partial v}{\partial y} + \frac{\partial w}{\partial z} = 0 \tag{2.7d}$$

where Eq. 2.7c is on index form, where repeated indices are summed 1-3, and Eq. 2.7d latter form is obtained by assuming incompressible flow, setting
$mathbf{u} = (u\, v\, w)^{\mathrm{T}}$ and letting $x$, $y$ and $z$ denote the spatial coordinates.

### 2.1.2 Momentum

For conservation of momentum, we let the generic property be linear momentum $p$, with the specific counterpart $\rho$
$mathbf{u}$. However, to properly conserve this quantity, we cannot simply set the rate equal to zero. A consequence of Euler's first axiom is that the rate of change of linear momentum equals the net force applied to the control volume.

This can be written

$$\frac{\mathrm{d}}{\mathrm{dt}}\mathbf{p} = \frac{\mathrm{d}}{\mathrm{dt}} \int_{\Omega(t)} \rho \tag{2.8}$$

$$mathbf{u}\, \mathrm{d}V = \mathbf{F} \tag{2.9}$$

where **F** denotes the resultant force vector on the control volume. This resultant can be decomposed into forces acting on the surface $\partial\Omega$, and the ones acting on the entire control volume $\Omega$. We denote the surface forces by **t** and the body forces by **b**.

$$\mathbf{F} = \int_{\partial\Omega} \mathbf{t}\, \mathrm{d}A + \int_{\Omega} \mathbf{b}\, \mathrm{d}V \tag{2.10}$$

Now the conservation of momentum can be written

$$\frac{\mathrm{d}}{\mathrm{dt}}\int_{\Omega(t)}\rho \tag{2.11}$$

$$mathbfu\,\mathrm{d}V = \int_{\partial\Omega}\mathbf{t}\,\mathrm{d}A + \int_{\Omega}\mathbf{b}\,\mathrm{d}V \tag{2.12}$$

Equation 2.12 is known as the integral form of the Cauchy equation of motion. By introducing coordinate stresses and using Cauchy's stress theorem, a differential form can be obtained as

$$\rho\dot{\mathbf{u}} = \frac{\partial\mathbf{T}}{\partial\mathbf{x}} + \rho\mathbf{b} \tag{2.13}$$

where **T** is the coordinate stress tensor

$$\mathbf{T} = \begin{bmatrix} \sigma_x & \tau_{xy} & \tau_{xz} \\ \tau_{yx} & \sigma_y & \tau_{yz} \\ \tau_{zx} & \tau_{zy} & \sigma_z \end{bmatrix} \tag{2.14}$$

with $\sigma$ denoting normal stresses and $\tau$ denoting shear stresses in the coordinate planes.

To further extend the equation for conservation of momentum from Eq. 2.13, we need knowledge of the fluid's properties. For a Newtonian fluid, a constitutive relation can be written [22] as

$$\mathbf{T} = -\left(p + \frac{2}{3}\mu\nabla\cdot\mathbf{u}\right)\mathbf{I} + 2\mu\mathbf{D} \tag{2.15}$$

with **I** the identity matrix and **D** the rate of strain, given as

$$\mathbf{D} = \frac{1}{2}\left[\nabla\otimes\mathbf{u} + (\nabla\otimes\mathbf{u})^{\mathrm{T}}\right] \tag{2.16}$$

where $\otimes$ denotes the outer or *dyadic* vector product between nabla and the velocity vector, to produce a 3 by 3 tensor.

The conservation of momentum for a Newtonian fluid control volume can then be found by

substituting the constitutive relation in Eq. 2.15 into Cauchy's equation of motion, Eq. 2.13.

$$\rho\dot{\mathbf{u}} = \frac{\partial}{\partial \mathbf{x}}\left(-\left(p + \frac{2}{3}\mu\nabla\cdot\mathbf{u}\right)\mathbf{I} + 2\mu\mathbf{D}\right) + \rho\mathbf{b} \tag{2.17}$$

For an incompressible fluid, $\nabla\cdot\mathbf{u} = 0$, and Eq 2.17 simplifies to

$$\frac{\partial \mathbf{u}}{\partial t} + (\mathbf{u}\cdot\nabla)\mathbf{u} = -\nabla p + \mu\nabla^2\mathbf{u} \tag{2.18}$$

$$\frac{\partial u_i}{\partial t} + v_j\frac{\partial u_i}{\partial x_j} = -\frac{\partial p}{\partial x i} + \mu\frac{\partial^2 u_i}{\partial x_j \partial x_j} \tag{2.19}$$

which are the well known Navier Stokes equations, the latter on index form, where repeated indices are summed 1-3.

Written out in cartesian coordinates, these equations take the form:

$$\frac{\partial u}{\partial t} + u\frac{\partial u}{\partial x} + v\frac{\partial u}{\partial y} + w\frac{\partial u}{\partial z} = -\frac{1}{\rho}\frac{\partial p}{\partial x} + \mu\left(\frac{\partial^2 u}{\partial x^2} + \frac{\partial^2 u}{\partial y^2} + \frac{\partial^2 u}{\partial z^2}\right) \tag{2.20a}$$

$$\frac{\partial v}{\partial t} + u\frac{\partial v}{\partial x} + v\frac{\partial v}{\partial y} + w\frac{\partial v}{\partial z} = -\frac{1}{\rho}\frac{\partial p}{\partial y} + \mu\left(\frac{\partial^2 v}{\partial x^2} + \frac{\partial^2 v}{\partial y^2} + \frac{\partial^2 v}{\partial z^2}\right) \tag{2.20b}$$

$$\frac{\partial w}{\partial t} + u\frac{\partial w}{\partial x} + v\frac{\partial w}{\partial y} + w\frac{\partial w}{\partial z} = -\frac{1}{\rho}\frac{\partial p}{\partial z} + \mu\left(\frac{\partial^2 w}{\partial x^2} + \frac{\partial^2 w}{\partial y^2} + \frac{\partial^2 w}{\partial z^2}\right) \tag{2.20c}$$

Together with Eq. 2.7, Eqs. 2.20 are the fundamental equations for fluid flow problems. These equations are capable of describing all incompressible flows. However, because of their complexity, analytical solutions have only been found for a very limited number of simple cases. The vast majority of real world fluid mechanics problems must be solved numerically.

### 2.1.3 Finite Volume Discretization and Pressure Correction

The finite volume method is a method for discretizing and solving the Navier Stokes equations numerically. It consists of dividing the computational domain into discrete cells, with nodes not necessarily corresponding to the boundaries. The conservation laws are applied on integral form to each cell. Thus, for the whole domain, the integrals can be added together, and as the

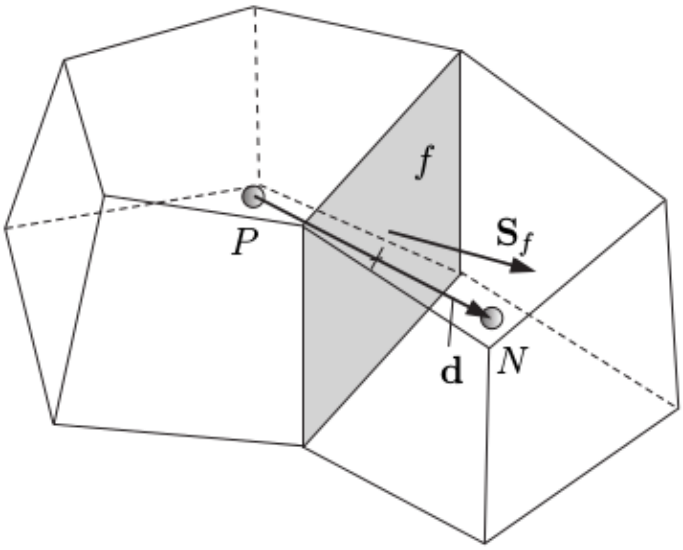


Figure 2.1: Control volume as defined in OpenFOAM. $P$ is the cell center, where the variables are stored. $d$ is the distance to the neighbour $N$, $f$ is the face of the cell and $S_f$ the outward normal vector of the cell surface.

internal surface integrals would cancel out, one would obtain the integral form of the conservation laws for the entire domain. This is one of the most desired property of the finite volume method for dealing with fluid problems, it is native mass conservant for the whole domain. The integral form does also allow discontinuities inside each cell, meaning, a shock wave for supersonic flow is captured by the equations. For the differential form, this would not be the case.

To evaluate the integrals in the governing equations, we use numerical integration. The simplest numerical integration takes the value at the node in the cell center and uses this as the mean for the cell. The integral is then easily computed as the mean value times the cell volume. Similar approximations can be made for surface integrals. The easiest version would be to let the mean of two neigbourhing nodes be the estimated mean on the surface, and multiply this with the surface area.

Most modern CFD codes relies on more advanced higher order interpolation techniques. In OpenFOAM, an open source CFD library [68] used exclusively for the 3D CFD simulations in this study, the user can benefit from a selection of dicretization and interpolation schemes. There are also the possibility to use different schemes for each term in the governing equation, i.e. discretizing a convective flux using one scheme and the pressure forces using another.

The common step for all CFD techniques is to transfer the governing partial differential equations to a system of algebraic equations, which are solved numerically. The size of the equation system will be the number of unknown nodes in the solution domain.

**SIMPLE pressure correction**

A drawback with the governing equations for incompressible flow is that the pressure does not enter the continuity equation. Thus, solutions to the three momentum equations does not necessarily satisfy continuity.

Various methods have been proposed for linking pressure to the continuity equation. In the solver used most frequently in this work, this is done by an implicit method, Semi-Implicit Method for Pressure Linked Equations (SIMPLE), presented by Patankar and Spalding [46]. The algorithm takes an initial guess for the pressure fields, and calculates an initial velocity field. Then, a pressure correction is calculated, and the pressure is updated. Then the velocity field is updated to satisfy the corrected pressure. This procedure is iterated until a prescribed tolerance is reached.

$$p = p^* + p' \tag{2.21a}$$

$$u_i = u_i^* + u_i' \tag{2.21b}$$

where $p^*$ and $u_i^*$ are the initial guesses for the pressure and velocity fields, respectively, and $p'$ and $u_i'$ are the corrections to satisfy the continuity equation.

To calculate the pressure correction, we need an equation linking the pressure to the continuity. Writing the steady state Navier-Stokes equations for an incompressible fluid on component form, isolating pressure on one side.

$$\frac{\partial p}{\partial x_i} = -\frac{\partial}{\partial x_j}\left(\rho u_i u_j - T_{ij}\right) \tag{2.22}$$

The main idea is now to take the divergence of this momentum equation,

$$\frac{\partial}{\partial x_i}\left(\frac{\partial p}{\partial x_i}\right) = -\frac{\partial}{\partial x_i}\left[\frac{\partial}{\partial x_j}\left(\rho u_i u_j - T_{ij}\right)\right] \tag{2.23}$$

By assuming constant viscosity and a divergence free velocity field, the viscous term is zero, and we are left with

$$\frac{\partial}{\partial x_i}\left(\frac{\partial p}{\partial x_i}\right) = -\frac{\partial}{\partial x_i}\left[\frac{\partial \rho u_i u_j}{\partial x_j}\right] \tag{2.24}$$

This elliptic equation can be solved numerically, and this is done for each pressure correction in the SIMPLE pressure loop, until the pressure update gets below a prescribed tolerance. Both Versteeg and Malasakera [66] and Ferziger and Peric [22] stresses the importance that the discretization used for the terms in the pressure equation must be consistent with the discretization of the equivalent terms in the momentum and the continuity equation.

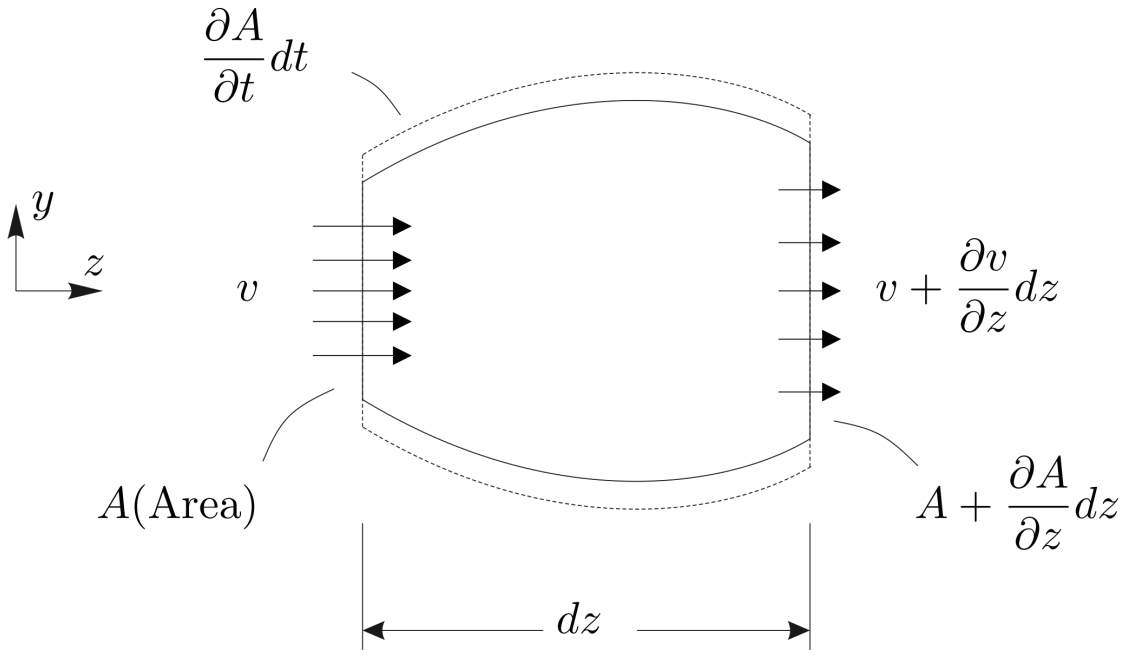


Figure 2.2: A one-dimensional control volume for compliant pipe flow.

## 2.2 1D Modeling of the Arterial Network

The conservation of mass and momentum for a 1D control volume in a compliant vessel as the one showed in figure 2.2, can be written as stated by Sherwin et al. [55]

$$\frac{\partial A}{\partial t} + \frac{\partial Q}{\partial z} = 0 \tag{2.25}$$

$$\frac{\partial Q}{\partial t} + \frac{\partial \alpha Q^2/A}{\partial z} = -\frac{A}{\rho}\frac{\partial p}{\partial z} + \frac{f}{\rho} \tag{2.26}$$

where $f$ accounts for all friction forces. The quantity $\alpha$ is introduced to account for the shape of the velocity profile, as this generally differs from a flat profile, (i.e. the no slip condition at the

walls must be satisfied). In the case of a theoretical, flat profile, $\alpha = 1$. This quantity is defined through

$$\int_A \rho u^2 \mathrm{d}A = \alpha \rho \bar{u}^2 \tag{2.27}$$

Where $u$ is the local velocity and $\bar{u}$ the cross sectional mean velocity.

As the flow in vessels is not limited to Poseuille flow or known Womersley profiles, one often defines a general polynomial velocity profile on the form

$$u(z,r,t) = \bar{u}\Phi(\gamma) = \bar{u}\frac{\gamma+2}{\gamma}\left(1-\left(\frac{r}{R}\right)^{\gamma}\right) \tag{2.28}$$

where $\gamma$ are the order of the polynomial , $R$ the radius and $r$ the radial coordinate. $\gamma = 2$ corresponds to a Poseuille (parabolic) profile. The cross sectional integral of Eq. 2.28 will allways be equal to 1, and the no-slip condition at the vessel wall holds, ie ($u(r = R, z) = 0$). As the velocity profile is continous and differentiable, we can compute the wall shear stress using Eq. 2.43. The friction force on the control volume will be $f = \tau_w 2\pi R$. Differentiating, we get

$$f = -\mu\bar{u}(\gamma+2)2\pi \tag{2.29}$$

By evaluating the cross sectional integral in Eq. 2.27, and substituting Eq. 2.28, we can express our correction factor $\alpha$ as

$$\alpha = \frac{\gamma+2}{\gamma+1} \tag{2.30}$$

Writing the variables as a vector $\mathbf{u} = [p\ q]^T$, the governing equations can be written in matrix notation as

$$\frac{\partial \mathbf{u}}{\partial t} + \mathbf{M}(\mathbf{u})\frac{\partial \mathbf{u}}{\partial z} = \mathbf{b}(\mathbf{u}) \tag{2.31}$$

with **M** given as:

$$\mathbf{M} = \begin{bmatrix} 0 & \frac{1}{C} \\ C(c^2 - \alpha\bar{u}^2) & 2\alpha\bar{u} \end{bmatrix} \tag{2.32}$$

with $c$ the wave speed given as $c = \sqrt{A/(\rho C)}$. **b** is given as:

$$\mathbf{b} = \begin{bmatrix} 0 \\ -2\pi(\gamma+2)\nu\bar{u} \end{bmatrix} \tag{2.33}$$

**Implementation in STARFiSh**

In STARFiSh, an acronym for Stochastic Arterial Flow Simulations, a python based network solver developed at department of structural engineering at NTNU, a framework for solving the governing equations in 1D arterial network is implemented.

The implementation uses an explicit MacCormack scheme to discretize the governing equations. The system is written in a conservative form, using

$$\mathbf{M} = \frac{\partial \mathbf{F}}{\partial \mathbf{U}} \tag{2.34}$$

The implementation is a predictor-corrector method, with the predictor $\hat{\mathbf{u}}$ defined as in Eq. 2.35a, and the corrector given by Eq. 2.35b.

$$\hat{\mathbf{u}}_i = \mathbf{u}_1^n - \frac{\Delta t}{\Delta x}\left[\mathbf{F}_{i+1}^n - \mathbf{F}_i^n\right] + \Delta t\mathbf{b}\left(\mathbf{u}_i^n\right) \tag{2.35a}$$

$$\mathbf{u}_i^{n+1} = \frac{\mathbf{u}_i^{n+1} + \hat{\mathbf{u}}_i}{2} - \frac{\Delta t}{2\Delta x}\left[\hat{\mathbf{F}}_i - \hat{\mathbf{F}}_{i-1}\right] + \frac{\Delta t}{4}\left[\mathbf{b}\left(\hat{\mathbf{u}}_i\right) + \mathbf{b}\left(\mathbf{u}_i^n\right)\right] \tag{2.35b}$$

The predictor consists of forward Euler differences in both space and time for the value at $t_{i+1}$, while the corrector step uses backward differences with a time step of $\Delta t/2$, where the value at $t_{i+1/2}$ is approximated as $u_{i+1/2} = \frac{u_i + \hat{u}_{i+1}}{2}$.

As the scheme is explicit in time, the Courant-Friedrich-Lewy [15] criteria for stability must be satisfied, meaning that information cannot travel further than one cell length per iteration. Formally, this criteria is given as

$$\text{CFL} = \frac{u_{max}\Delta t}{\Delta x} \leq 1 \tag{2.36}$$

For wave propagation problems, $u_{max}$ will be the maximum flow velocity plus the wave speed, $u_{max} + c$.

## 2.3 2D Pipe Flow

A special simplification can be done of Eqs. 2.20 when we are considering an axisymmetric pipe. Rewriting the Navier Stokes equations in cylindrical coordinates and simplifying, we obtain the following expression for the momentum balance in the $z$-direction, which we let be parallel to the pipe axis. The continuity equation for an incompressible fluid is also included in cylindrical coordinates, for reference.

$$\frac{1}{r}\frac{\partial}{\partial r}(r u_r) + \frac{1}{r}\frac{\partial u_\theta}{\partial \theta} + \frac{\partial u_z}{\partial z} = 0 \tag{2.37}$$

$$\rho\left(\frac{\partial u_z}{\partial t} + u_r\frac{\partial u_z}{\partial r} + \frac{u_\theta}{r}\frac{\partial u_z}{\partial \theta} + u_z\frac{\partial u_z}{\partial z}\right) = -\frac{\partial p}{\partial z} + \mu\left[\frac{1}{r}\frac{\partial}{\partial r}\left(r\frac{\partial u_z}{\partial r}\right) + \frac{1}{r^2}\frac{\partial^2 u_z}{\partial \theta^2} + \frac{\partial^2 u_z}{\partial z^2}\right] + \rho g_z \tag{2.38}$$

If we now assume a steady state flow, the transient terms disappear. By symmetry, all derivatives with respect to $\theta$ will be zero, as well as all terms including $u_r$ and $u_\theta$. Thus, we can simplify Eq. 2.38 to

$$\frac{1}{r}\frac{\partial}{\partial r}\left(r\frac{\partial u_z}{\partial r}\right) = \frac{1}{\mu}\frac{\partial p}{\partial z} \tag{2.39}$$

Two times integration yields the general solution

$$u_z = \frac{1}{4\mu}\frac{\partial p}{\partial z}r^2 + C_1 \ln r + C_2 \tag{2.40}$$

Where $C_1$ and $C_2$ are integration constants. By requireing that $u_z$ is not infinity at $r = 0$, we see that $C_1 = 0$. By further imposing a no slip condition at the pipe wall, (i.e $u_z(r = R) = 0$), where $R$ is the pipe radius, we get

$$C_2 = -\frac{1}{4\mu}\frac{\partial p}{\partial z}R^2 \tag{2.41}$$

yielding the well known parabolic velocity profile

$$u_z = -\frac{1}{4\mu}\frac{\partial p}{\partial z}\left(R^2 - r^2\right) \tag{2.42}$$

As we have assumed a Newtonian fluid, we can then calculate the shear stress on the wessel wall as

$$\tau_w = \mu\frac{\partial u_z}{\partial r}\bigg|_{r=R} = \frac{1}{2}\frac{\partial p}{\partial z}R \tag{2.43}$$

We can also integrate the velocity profile over the cross section, to get the volumteric flow rate. This takes the form

$$Q = \int_A v_z(r)\,\mathrm{d}A = 2\pi\int_0^R -\frac{1}{4\mu}\frac{\partial p}{\partial z}\left(R^2 - r^2\right) r\,\mathrm{d}r = -\frac{\pi}{8\mu}\frac{\partial p}{\partial z}R^4 \tag{2.44}$$

Substituting Eq. 2.44 in Eq. 2.43 we find that

$$\tau_w = \mu\frac{2Q}{\pi R^3} = \mu\frac{16}{\pi}\frac{Q}{d^3} = 2\frac{Q}{A}\frac{\mu}{R} \tag{2.45}$$

where $d = 2R$ is the pipe diameter. noting that $Q/A = \bar{u}$, we can also write the shear stress as

$$\tau_w = \frac{2\mu}{R}\bar{u} \tag{2.46}$$

By introducing the Reynolds' number

$$\mathrm{Re} = \frac{\rho \bar{u} d}{\mu} \tag{2.47}$$

we can write the shear stress as

$$\tau_w = \frac{\mathrm{Re}\,\mu^2}{\rho R^2} \tag{2.48}$$

For a pipe segment of uniform cross-section, we can also integrate the wall shear stress along the pipe wall to get the friction force.

$$F_{visc} = \int_0^L \int_0^{2\pi} \tau_w R \,\mathrm{d}\theta \,\mathrm{d}z = \mu \frac{32Q}{d^2} L \tag{2.49}$$

By the relation $\Delta p = F/A$, we can write the pressure drop for a uniform pipe segment as

$$\Delta p = \frac{F_{visc}}{A} = \frac{128}{\pi}\frac{\mu L Q}{d^4} \tag{2.50}$$

### 2.3.1 Leaking Pipe Wall

The motivation for this section is the fact that the number of outlets seen from a CT-image of the coronary arteries are far below the real number, because of the limited resolution of these images, and challenges in the segmentation process. One way of approximating these discrete outlets could be a continuous leak model. The phenomenon of leaky pipes has been studied by numerous investigators. Analytical solutions was first proposed for small values of suction or injection, kept constant along the pipe wall in both the circumferential and the axial direction, by Berman in 1953 [5]. Terrill and Thomas [59] extended the work in 1969, including a discussion of stability based on the cross flow Reynolds' number $Re_w = \frac{v_w D}{\nu}$. Later, the theory was

extended to allow variable wall suction by Galowin et al. [25], but still, the leakage had to be explicitly specified. However, if one assume that collateralization, the formation of small arteriole branches, is strongly dependent on the local pressure, it is desirable to incorporate Darcy's porosity law to control the radial outflow. Darcy's porosity law reads:

$$\frac{Q_w}{A} = v_w = -\frac{k}{e\mu}\nabla p \tag{2.51}$$

Where $Q_w$ is the permeate flow rate, $A$ the total pipe wall area, $v_w$ the permeate radial velocity, $k$ a porosity constant, $e$ the pipe wall thickness and $\mu$ the kinematic viscosity.

Karode et al. [31] showed in 2001 analytical results for both channel and pipe flow with constant wall permeabilities and constant wall suction, based on a perturbation of the Poseuille solution for non-leaking pipes. His derivations were only showed for channel flow. The same approach of perturbing the solutions for is used here for pipe flow.

Repeating Eq. 2.44, given for a infinitesimal pipe segment $dz$, leading $\Delta p/dz \rightarrow \frac{\partial p}{\partial z}$:

$$Q = \frac{8\pi R^4}{\mu}\frac{\partial p}{\partial z} \tag{2.52}$$

Differentiating with respect to z, we get

$$\frac{\partial Q}{\partial z} = \frac{8\pi R^4}{\mu}\frac{\partial^2 p}{\partial z^2} \tag{2.53}$$

Now introducing the volumetric loss as $u_R 2\pi R dz$, we get

$$\frac{8\pi R^4}{\mu}\frac{\partial^2 p}{\partial z^2} = u_R 2\pi R \tag{2.54}$$

For the case of a constant wall velocity (i.e $u_R = \text{const}$), we transform equation 2.54 to an ODE, by the assumption that the pressure is constant across the pipe cross section, thus only dependent on $z$. Two times integration yields

$$p(z) = \frac{4\mu u_R}{\pi R^3}\left(\frac{z^2}{2} + C_1 z + C_2\right) \tag{2.55}$$

The boundary conditions will be:

$$p(0) = p_i, \tag{2.56a}$$

$$\left.\frac{\partial p}{\partial z}\right|_{z=0} = \frac{Q_i \mu}{8R^4} \tag{2.56b}$$

Where $Q_i$ is the incoming flow at $z = 0$ and $p_i$ the pressure at the same location. Evaluation of the integration constants yields the following expression for the pressure in the streamwise direction:

$$p(z) = \frac{8\mu Q_i z}{\pi R^4}\left(1 - \frac{2\pi R z u_R}{2Q_i}\right) \tag{2.57}$$

If we instead assume constant wall permeability, then $u_R$ is modeled by applying Darcy's law to a one-dimensional membrane, $u_R = k(p - p_0)$ where $p$ is the pressure at the membrane wall and $p_0$ is the surrounding pressure. Then we have

$$\frac{8\pi R^4}{\mu}\frac{\partial^2 p}{\partial z^2} = k(p - p_0)2\pi R \tag{2.58}$$

Setting $p' = p - p_0$, and isolating the second derivative, we obtain

$$\frac{\partial^2 p'}{\partial z^2} = \frac{k\mu}{4R^3}p' \tag{2.59}$$

Again we assume constant pressure in all cross sectional planes. Equation 2.59 then degenerates to a second order ODE. Setting $\lambda^2 = \frac{k\mu}{4R^3}$, we can write the general solution as

$$p'(z) = C_1 e^{\sqrt{\lambda}z} + C_2 e^{-\sqrt{\lambda}z} \tag{2.60}$$

The boundary conditions for Eq. 2.59 are

$$p'(0) = p_i - p_0, \tag{2.61a}$$

$$\left.\frac{\partial p'}{\partial z}\right|_{z=0} = \frac{Q_i \mu}{8R^4} \tag{2.61b}$$

Yielding the expression

$$p(z) = p_i - \frac{\mu Q_i}{\pi R^4 \lambda}\left(e^{\lambda z} - e^{-\lambda z}\right) + (p_i - p_0)\left(1 - \frac{1}{2}\left(e^{\lambda z} + e^{-\lambda z}\right)\right) \tag{2.62}$$

for the streamwise pressure drop.

Equations 2.57 and 2.62 will be used for validation of simulations of leaky vessels in chapter 5.

## 2.4 Murray's Law

Murray's law relates the radii of mother and daughter branches in bifurcating blood vessels, and the radius to the volumetric flow rate in the vessel. The law was proposed by Cecil Murray as early as in 1926 [43]. The basic idea is that the body wishes to autoregulate the vessel dimensions to minimize the overall power required by the circulatory system. The idea is a trade off between large volume of blood and large vessels, with increased metabolism, or smaller vessels and less blood, leading to increased pumping power for the heart. Murray's original energy demand rate equation reads

$$E = \Delta p Q + b V_{blood} = \frac{Q^2 l 8\mu}{\pi r^4} + b l \pi r^2 \tag{2.63}$$

where $b$ is a constant for the energy demand of keeping blood and tissue alive, $Q$, the volumetric flow rate, $L$ the vessel length and $\Delta p$ the pressure loss over the vessel, here expressed for Poseuille flow. The cost function is then differentiated with respect to the vessel radius, and set equal to zero to find the minimum required energy. Assuming $b$ to be a constant, Murray's law for branches will then after Zamir et al [77] take the form

$$r_m^c = r_1^c + r_2^c + \cdots + r_n^c \tag{2.64}$$

Where $m$ denotes the mother branch, and $1, \ldots n$ denotes the daughter branches. The parameter $c$ is known as Murray's constant. This constant takes the value 3 for laminar *Poseuille* flow, while a value of $7/3$ has been proposed for turbulent flows [54].

A corollary from Murray's law is proposed by Murray in the original paper

$$Q = kd^3, \quad \rightarrow Q \propto d^3 \tag{2.65}$$

This can be seen as a local interpretation of the body's autoregulation mechanism, and by comparing equation 2.45 to equation 2.65, we see that for Poseuille flow, Murray's autoregulation corresponds to a constant shear stress in the vessel wall. This was also emphasized by Zamir in [76, 75], and proposed to be a more physiologically correct way of interpreting the relationship from the original Murray's law. Shear stress can be sensed by the endothelial cells, and give appropriate feedback to the autoregulation system.

## 2.5 Lumped Models for Stenosis

In this section, three lumped models for computing the pressure drop over a stenosis is presented. A schematic of typical constriction geometries used in these models is shown in figure 2.3.

**Stetteler et al**

Stettler et al [57] proposed an equation for the stenotic pressure drop, based on a consideration of the Borda-Carnot effect and the viscous friction on the form:

$$\Delta p = \frac{\rho}{2} {v_1}^2 \left( \frac{A_0}{A_e} - 1 \right)^2 + 8\pi\mu L v_1 (A_0/A_e)^2 \tag{2.66}$$

where $A_0$ is the cross sectional area in the unconstricted region, and $A_e$ the *effective* area of the stenosis. This is taken as the lumen cross sectional area at the constriction, minus the area occupied by the boundary layer.

This model is given for short stenoses only, where the flow is not fully developed at the end of the stenosis. The relation can be compared to the empirical relations for flow through an orifice.

**Young and Tsai**

Young and Tsai [74] proposed lumped stenosis models for both steady and transient flow, in a series of papers in the 1970's. Their steady state experiments considered an axisymmetric stenosis on the form

$$\frac{r}{R_0} = 1 - \frac{\delta}{2R_0} \left( 1 + \cos\left( \frac{\pi z}{Z_0} \right) \right) \tag{2.67}$$

where $\delta$ is the plaque layer height measured from the vessel wall, $R_0$ the radius of the vessel upstream of the stenosis, and $z$ the cordinate in the vessel direction, limited by $-Z_0 < z < Z_0$.

For the non-symmetric stenoses, Young and Tsai modelled these as a cylindrical obstruction, whith the cylinder axis normal to the vessel centerline. Then, the radius $\zeta$ and the stenosis height $\delta$ was chosen to give corresponding reduction in lumen volume as the different axisymmetric models.

By a dimensional analysis, the pressure drop across the stenosis was modelled using a weighted sum of the expansion pressure drop and the turbulent pressure drop.

$$\frac{\Delta p}{\rho \bar{u}^2} = \frac{K_v}{Re} + \frac{K_t}{2} \left[ \frac{A_0}{A_1} - 1 \right]^2 \tag{2.68}$$

In equation 2.68, $A_0$ denotes the unconstricted cross sectional area, $A_1$ the minimal lumen cross sectional area, and $\bar{u}$ the mean velocity in the unconstricted section. $K_v$ and $K_t$ are empirical

constants, to be determined.

Young and Tsai performed experiments with various constriction ratios, for Reynolds' numbers ranging from 100 to 4000. For this range they proposed a value for $K_t = 0.9$, while the viscous constant $K\nu$ was highly dependent on the constriction ratio, taking a value of 700 for a 56 % area reduction and a value of 4500 for a 89 % area reduction. This value was the same for both a stenosis length of 4 and 8 times the vessel diameter, indicating the key parameter to be the area reduction.

#### Lee and Fung

Lee and Fung [36] investigated an axi-symmetric constriction, using a bell-curve for the constriction, given by the function

$$\frac{r}{a_0} = 1 - b\exp\left(-\frac{cz^2}{{a_0}^2}\right) \tag{2.69}$$

They performed experimental studies on both local constrictions, stenosis , and local dilatations, which we today would call aneurysms.They considered Reynolds' numbers in the range $[0,25]$. Without proposing a lumped model, they delivered experimental data on both pressure drop and flow patterns around the stenosis. The range of Reynold's number they considered are below what one would expect for healthy coronary circulation, but their model is included for reference, as the geometry is very similar to the one used by Young and Tsai.

## 2.6 Image Segmentation - Level Set Method

Segmentation describes the transformation of medical images to three dimensional models suitable for computation. In this study, segmentation is done with vmtk -the vascular modeling toolkit, an open source library written by Luca Antiga [2]. A brief outline of the underlying method follows here, with focus on the parameters to specify when using the framework. CT datasets are black and white images of X -ray reflections, stacked together to form a three dimensional array of intensity values. The image can be described by the function

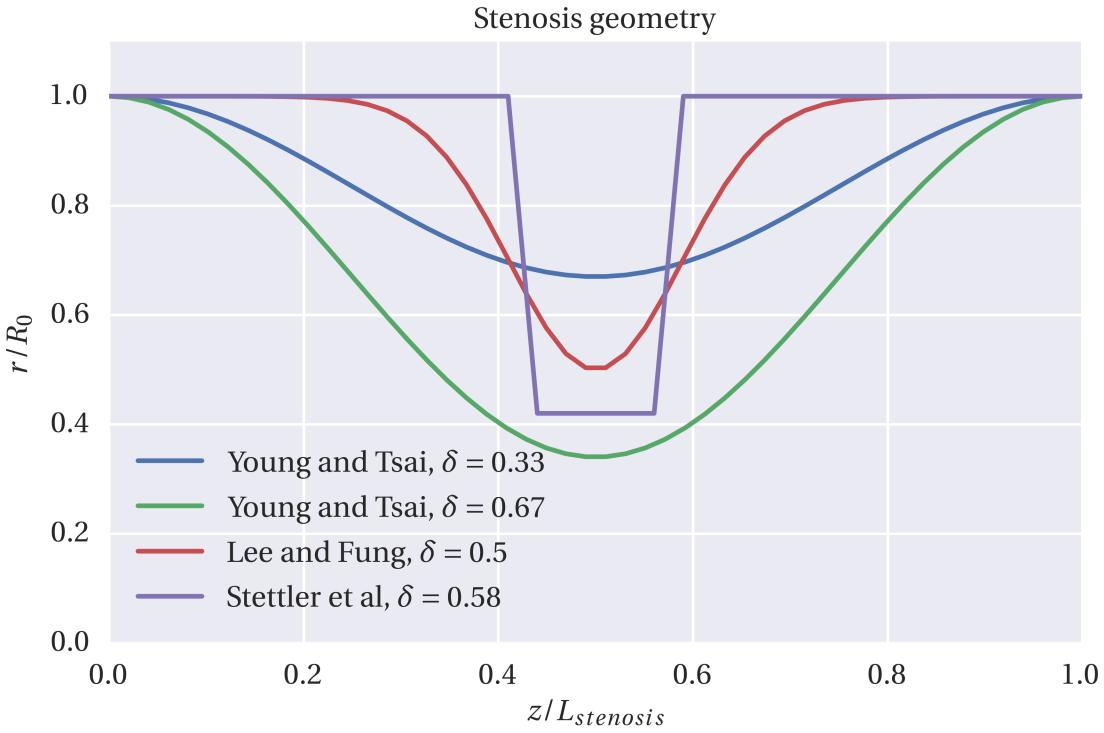


Figure 2.3: Non-dimensional stenosis geometries for the models of Young & Tsai and Lee & Fung for different values of the stenosis wall displacement, $\delta$.

$$I(\mathbf{x}),\ \mathbf{x} \in \mathbb{R}^3 \tag{2.70}$$

where $I$ is the scalar intensity value and $\mathbf{x}$ a cartesian coordinate vector.

Level set segmentation is based on the idea that there exist a function which will be 0 on all points on a surface $S$, strictly positive inside the surface, and strictly negative outside the surface.

$$S(t):\ \Phi(\mathbf{x}, t) = 0 \tag{2.71}$$

Allowing the surface to evolve in time makes us able to write a partial differential equation for the surface's temporal evolution.

$$\frac{\partial \Phi}{\partial t} = -w_1 G(\mathbf{x}) |\nabla \Phi| + w_2 2H(\mathbf{x}) |\nabla \Phi| - w_3 \nabla P(\mathbf{x}) \cdot \nabla \Phi \tag{2.72}$$

Here, $G(\mathbf{x})$ is the inflation speed. This acts in the opposite direction of the gradient, to increase the volume encapsuled by $S$. The function $H(\mathbf{x})$ describes a constraint on the smoothness of the surface, defined as the mean curvature of the surface, namely

$$H(\mathbf{x}) = \nabla \cdot \frac{\nabla \Phi}{|\nabla \Phi|} \tag{2.73}$$

$P(\mathbf{x})$ is a scalar function whose gradient accounts for the advection of the surface, equivalent to the advection terms in the Navier Stokes equation. $w_1$, $w_2$, and $w_3$ are weights that determine the contribution from each term on the surface's temporal movements. These three weights are specified for each short vessel segment analyzed in vmtk.

To obtain the final surface, Eq. 2.72 can be solved numerically, from an initial surface. This is done using a finite difference grid in vmtk, for every vessel segment that is extracted.

### Initialization

The initial surface can be created in a number of different ways. The method commonly used for tubular segment is called colliding fronts. With this method, the user specifies two end points. From these, the surface is marched with velocity proportional to the image intensity. The initialization stops when the two surfaces intercept, the idea being that the surfaces travel much faster in the parts of the image containing lumen, as this is filled with contrast agent giving a high radiodensity.

# Chapter 3

# Ideal Stenosis Geometry

In this chapter, a generic stenosis geometry was investigated. A number of simulations were run, and the results were validated against experimental results published by Young and Tsai [74]. Both 3D CFD with OpenFOAM and one-dimensional simulations in STARFiSH were run. A lumped model for the pressure jump was implemented in STARFiSh and was shown to improve the predictions from these simulations.

## 3.1 Setup

Domains consisting of cosine stenosess corresponding to an area reduction of 56 % and 89 % were modeled and simulated for various Reynolds' numbers considered to be physiologically relevant. A schematic of the geometry of the domain is shown in figure 3.1.The flow rates, the mean velocities and the Reynolds' numbers at the inlet and at the point of minimum cross sectional area are listed in table 3.1. Blood was modeled as a Newtonian fluid, with a kinematic viscosity $\mu = 3.5 \cdot 10^{-3}\ kg/ms$ and a density $\rho = 1050\ kg/m^3$.

### 3.1.1 OpenFOAM Configuration

#### Meshing

For the 3D simulations, a structured mesh of 350 000 hexahedral cells was created. The domain included uniform tubing 25 mm upstream and 115 mm downstream of the stenotic section, as

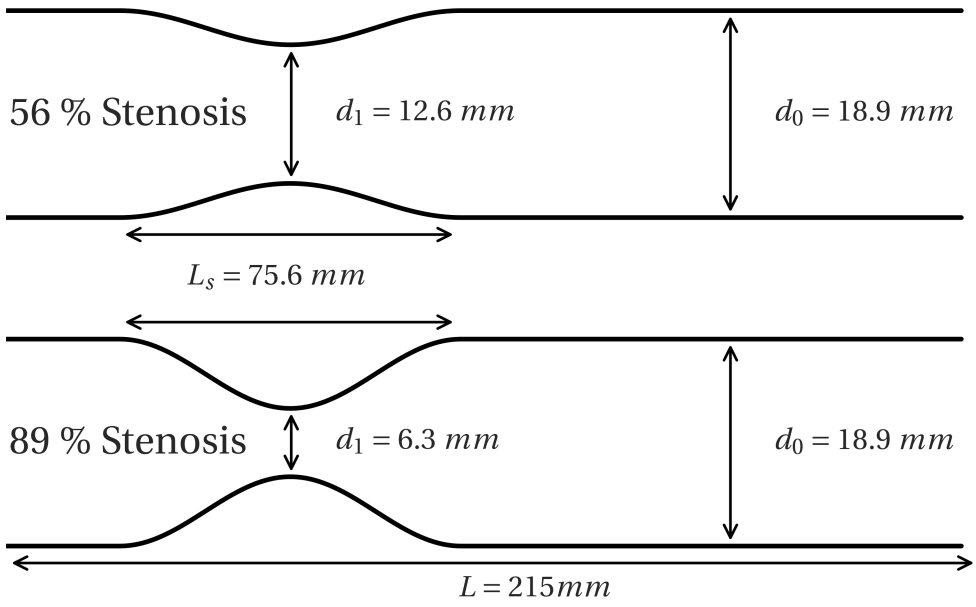


Figure 3.1: Schematic of an axial plane of the computational domains for CFD simulations.

indicated in figure 3.1. This was done to capture the pressure recovery all the way to the point 115 mm downstream, where Young and Tsai performed their pressure measurements, to ensure comparability between the results. Young and Tsai measured the pressure 115 mm upstream also. The straight section upstream of the stenose was only partially included in the computational domain, to save computational costs. An additional pressure drop was therefore necessary to compare simulations and experiments. Young and Tsai reported the flow to be laminar in this region, ensured experimentally by a long, smooth straight pipe section before the measurement section. By the laminar fully developed flow assumption, the additional upstream pressure drop was calculated by Eq. 2.50 in the present work.

**Boundary Conditions**

Rigid walls was assumed, as the glass tubes used in the experiments can be assumed rigid at the pressure ranges involved [20]. A parabolic velocity profile was specified at the inlet, as the flow is here believed to be fully developed. At the outlet, the gradient was specified to zero, a common

Table 3.1: Flow conditions at inlet and at minimum cross sectional area.

| | | | | | | |
|---|---|---|---|---|---|---|
| Inlet | $Re_{in}$ | 100 | 200 | 400 | 600 | 900 |
| | $u_{in}$ $(cm/s)$ | 1.76 | 2.65 | 3.53 | 7,05 | 17.6 |
| | $Q_{in}$ $(ml/s)$ | 4.95 | 7.42 | 9.90 | 19.8 | 49.5 |
| 56 % Stenosis | $Re_{stenosis}$ | 150 | 300 | 600 | 900 | 1350 |
| | $u_{stenosis}$ $(cm/s)$ | 3.97 | 7.94 | 15.9 | 23.8 | 35.7 |
| 89 % Stenosis | $Re_{stenosis}$ | 300 | 600 | 1200 | 1800 | 2700 |
| | $u_{stenosis}$ $(cm/s)$ | 15.9 | 31.7 | 63.5 | 95.2 | 143 |

outflow boundary condition [22], shown not to force the solution in the domain excessively. This condition is here assumed not to interfere with the upstream solution far from the outlet. At the wall a no-slip boundary condition was imposed by specifying all velocity components to be 0. For the pressure, a zero gradient was specified at the walls and at the inlet, while a reference value of 0 was set at the outlet. As the flow is only dependent on the pressure gradient, setting the reference value to 0 is common in incompressible CFD codes [22].

**Solver Configuration**

The OpenFOAM application simpleFoam was chosen, a steady state solver with capabilities of turbulence modeling. However, in this thesis, turbulence modeling was not pursued, as the simulation of transitional flows is a complex field on its own [33]. As the name of the solver implies, the SIMPLE pressure correction method is utilized, as described in section 2.1.3. The simulation case was built from the pitzDaily tutorial case available with the OpenFOAM distribution, using the default linear equations solvers and parameters, unless explicitly specified. The solution was initialized from a zero velocity field, and the solution was iterated until the residuals were below $10^{-3}$ for the velocity components, and $10^{-3}$ for the pressure. The iterations was under-relaxed with a factor of 0.7 for the velocity components and a factor 0.3 for the pressure. The OpenFOAM simulations of the mild stenosis did require between 0.5 and 1 CPU hour at 2.5 GHz, depending on the Reynolds' number. For the more severe stenosis, a refined mesh and a transient solver was employed, requiring 2-4 CPU-hours per second of simulation time.

### 3.1.2 STARFiSh

Simulations of the same test case was also performed using STARFiSh. Because the computational cost in 1D is lower compared with the 3D CFD, the entire test setup from Young and Tsai was modeled, including the complete tubing upstream of the constriction. Although the STARFiSh code has capabilities of simulations with compliant walls, rigid walls was specified to ensure comparability with the 3D and experimental results. The stenotic region was divided in 100 segments, and the uniform pipes up- and downstream were both discretized into 50 segments, later refined to 106 nodes from the CFL grid adaption in STARFiSh.

The incoming flow rate was specified as a ramped signal over the first two seconds of the simulation to increase stability. The solution was later iterated 8 seconds further. A temporal convergence down to $10^{-8}$ was observed after 6 seconds of simulations with constant boundary conditions.

As the frictional forces in the original STARFiSh code only enters through the wall friction from Eq. 2.43, the most straight-forward method to modify the viscous pressure drop, without changhing the viscosity in a STARFiSh simulation, is to change the value of $\gamma$ in Eq. 2.28. This approach was tested for both the mild and the severe constriction.

The simulations ran with STARFiSh required less than 5 minutes CPU time each, including the initialization time and the grid adaption.

## 3.2 Results

### 3.2.1 Mild Stenosis

From figure 3.2, we can see how the flow gets accelerated by the constriction, before redeveloping towards the parabolic velocity profile in the downstream region. The static pressure drops abruptly in the constriction, before being partially recovered downstream. For a Reynolds number of 100, the pressure recovers only in a short zone downstream of the stenosis, before the wall friction again dominates the deceleration of the flow, leaving the pressure to fall in the terminal part of the domain. This is also the case for a Reynolds' number of 200, although the redeveloping zone is noticeable longer than for Re = 100. For Reynolds' numbers above 400, the pressure

continues to recover in the entire section downstream, all the way to the outlet.

This gives the possibility of a continuing pressure recovery outside the domain considered.

The overall pressure drop is highly dependant on the flow rate through the constriction. At Re = 100, the pressure drop is below 2 kPa, while it is over 40 kPa for Re = 900. A value of 32 kPa for Re = 600 reveals the nonlinearity of the pressure drop with respect to flow rate, in contrast with the linear pressure-flow relation for uniform pipe sections, given in Eq. 2.50.

Young and Tsai reported a recirculation zone forming initially at Re = 195. Inspecting the velocity profiles in figure 3.2, or finding the Reynolds' number where a negative axial velocity first occurs, a recirculation zone is first observed at Re = 200 in the present study, in close agreement with the reported experimental results. For higher Reynolds' numbers, this recirculation zone will be longer and stretched out along the wall, contributing to the viscous dissipation by high velocity gradients.

The overall dimensionless pressure drops are shown for the mild stenosis in figure 3.5. 3D CFD results agree very well with the experimental findings for all Reynolds' numbers considered. The one-dimensional results are below the experimental results for $\gamma = 2$, for all Reynolds' numbers. Increasing $\gamma$ up to 9 makes it possible to capture the pressure drop for the mild stenosis, but no single value of $\gamma$ predicts the pressure well at all Reynolds' numbers.

As the pressure drop calculated with STARFiSh is linearly dependent on the flow, and increasing the gamma value also gives a linear increase in the pressure drop, as shown in figure 3.4. Other means of modeling this pressure drop was sought, through the implementation of a lumped model.

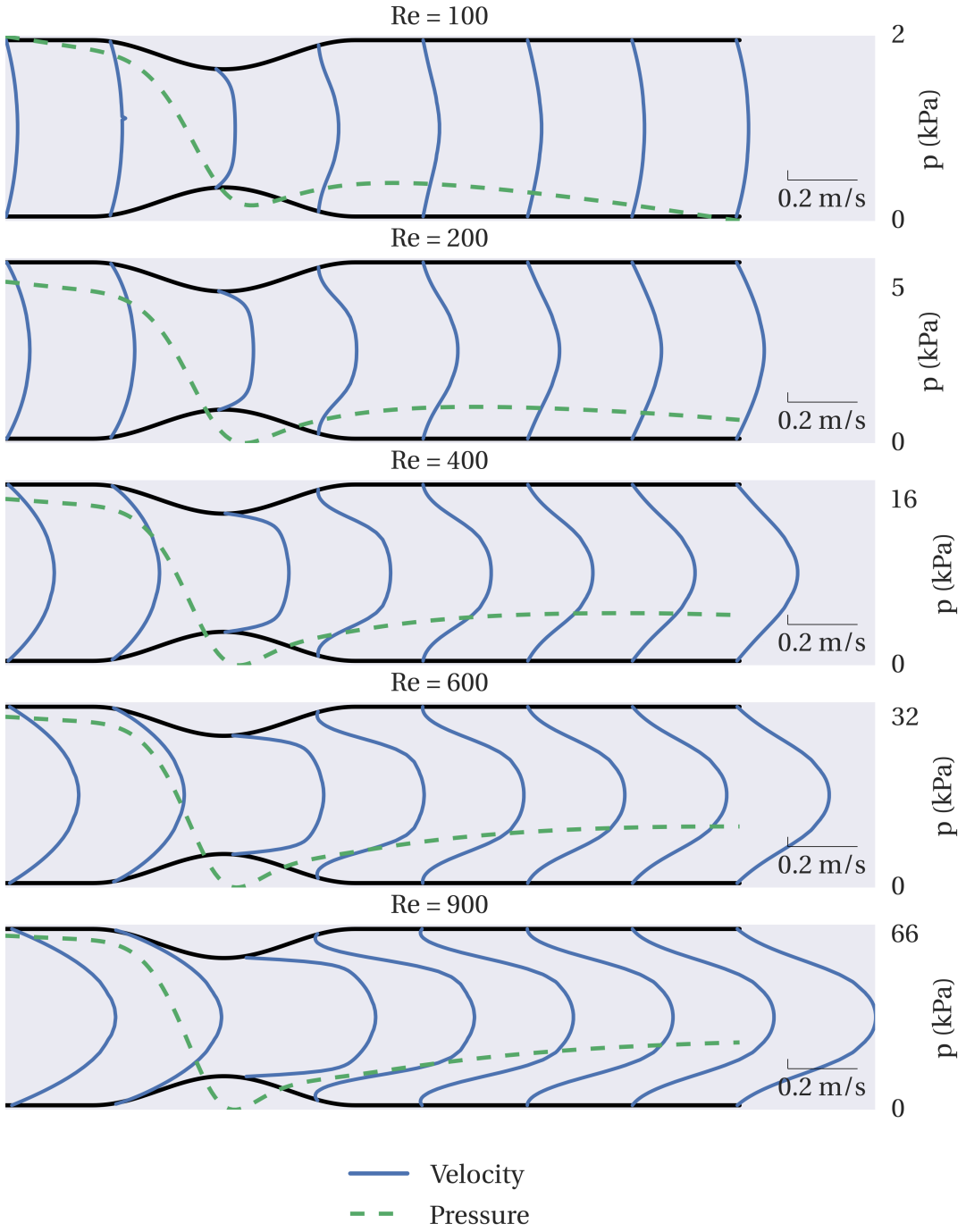


Figure 3.2: Velocityprofiles and pressure in mild (56 %) stenosis, from OpenFOAM simulations.

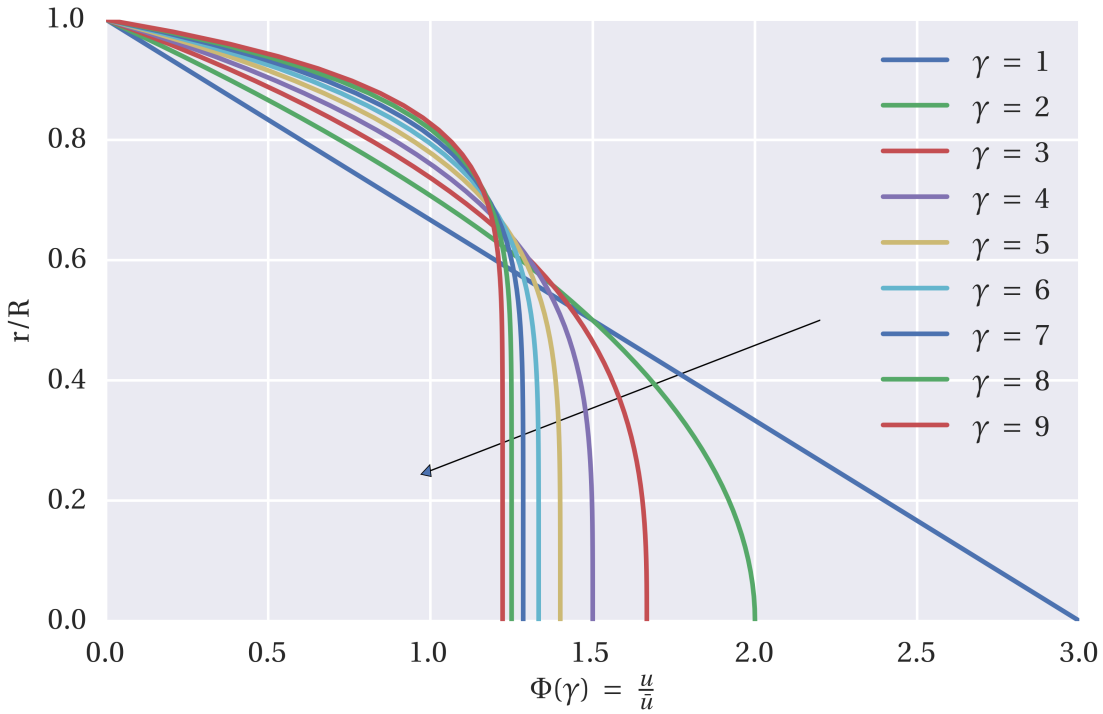


Figure 3.3: Velocityprofiles in use for one-dimensional modelling

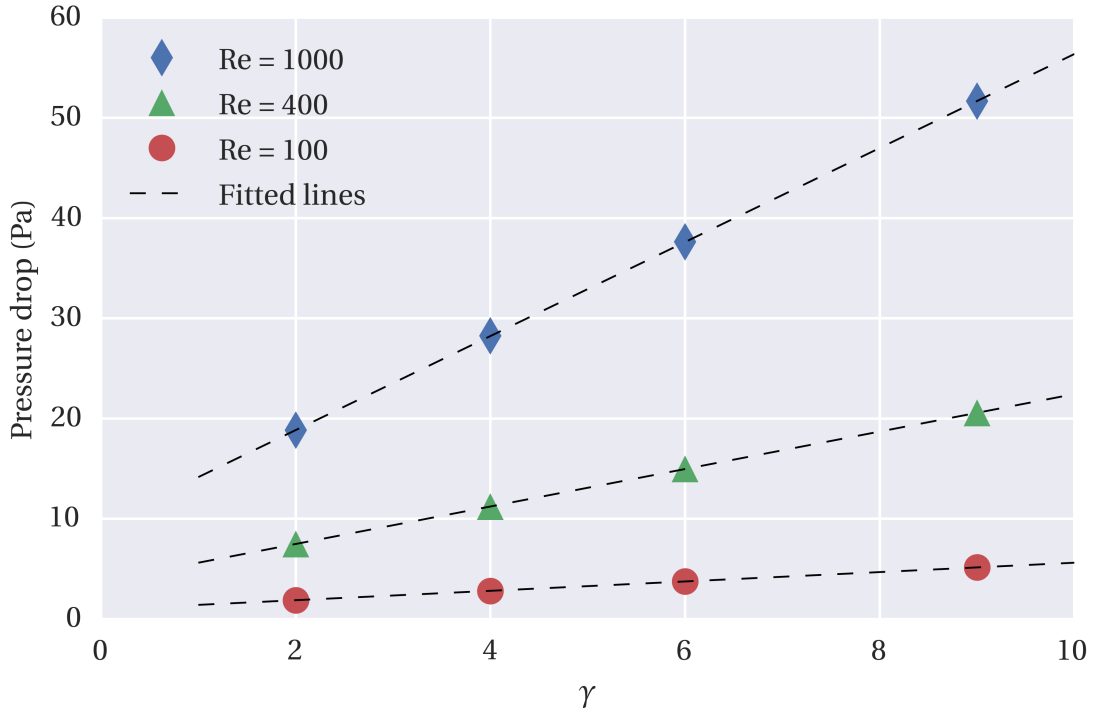


Figure 3.4: Pressure drop across stenosis for different velocityprofile assumptions in STARFiSh.

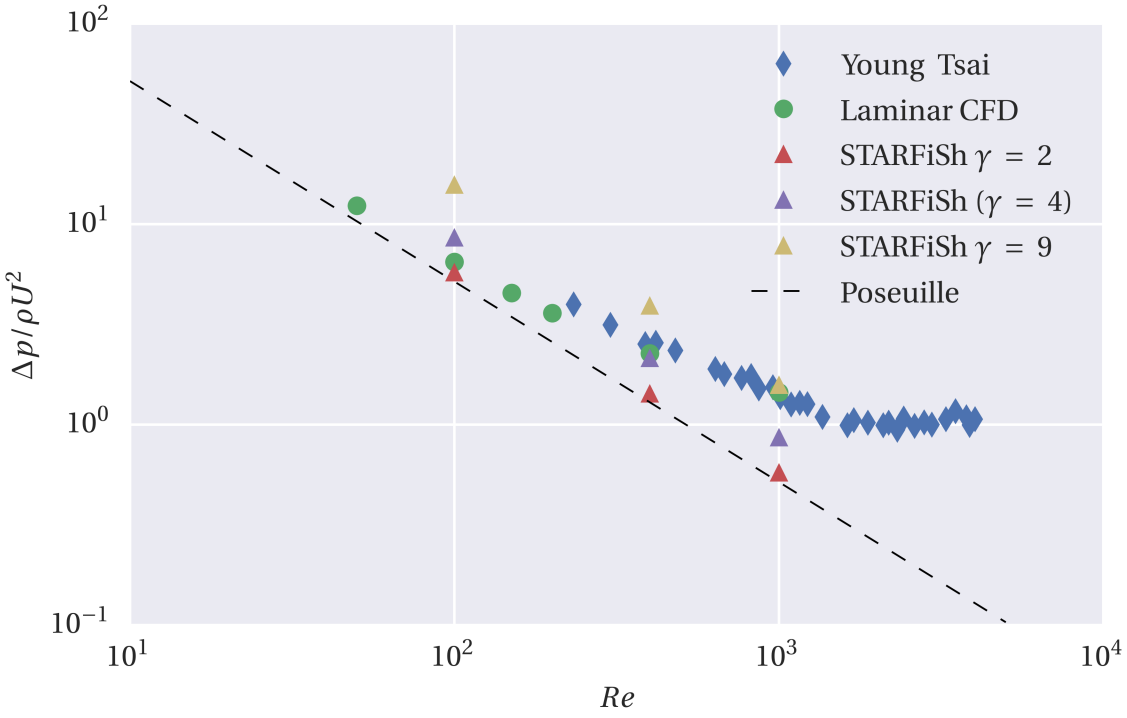


Figure 3.5: Dimensionless pressure drop plotted against Reynolds' number for a mild (56%) stenosis. Poseuille pressure loss for an unconstricted pipe is included, as well as results from STARFiSh simulations.

### 3.2.2 Severe Stenosis

For the more constricted stenosis, flow separation occurs even at Re = 100, compared to at Re = 200 for the mild stenosis. Velocity profiles and the static pressure is shown for various Reynolds' numbers in figure 3.6. The pressure drops for this case is around 20 times higher than for the mild stenosis, in agreement with the findings of Young and Tsai. This ratio also confirms the importance of the minimum lumen cross sectional area for accurate stenosis computations. For Reynolds' numbers ranging from 200 and upwards, the recirculation zones stretches out in the entire domain, causing back flow in the modeled outlet. For the cases of Reynolds' numbers of 400 to 900, a pronounced jet is formed at the constriction, partially decelerated for the case of Re = 400 and 600, and almost undisturbed in the entire domain for Re = 900. It is also noticeable how the recirculation zones gets narrower at higher Reynolds' numbers. This contributes to higher velocity gradients and more dissipation of energy, resulting in an increased pressure drop.

For Re > 500, no steady state solutions were found, even after refining the mesh to 1.5 million cells and applying heavy under-relaxation. Considering a Reynolds' number at the point of maximum constriction of 2700, this was no surprise. However, with a Re at the inlet of only 900, and a laminar flow in the entrance of the domain, the possibility of including a turbulence model was rejected. Instead, a transient laminar solver was employed on the refined mesh, and the solution marched in time from an initial velocity field of zero velocity. Unsteady vortex shedding was seen in the downstream region from the stenosis, comparable to the well known Von Karman vortex street seen for flow past cylinders. After three seconds of simulation time, the overall pressure drop fluctuations was however within 1 % of the mean, and within 5 % of the pressure drop reported by Young and Tsai. A temporal average over 20 saved timesteps has therefore been made for the case of Re = 600 and Re = 900, to produce the mean velocity profiles shown in figure 3.6.

For Re = 900, Young and Tsai reported pressure measurements at multiple locations along the constricted region. This was compared to the simulated results in figure 3.7. As we see, the temporal averaged CFD predicts the overall pressure drop within 5 %, with the main deviation being in the recovery zone downstream of the constriction, and some in the narrowing of the constriction. Young and Tsai did not report whether their pressure measurements is a temporal

average or an instantaneous measurement, being a possible source for the deviation here. Another possible source of error is the domain length and the outflow condition. Setting an outlet pressure of 0 when backflow and vorticing is present, may cause the solution near the outlet to suffer. The purely one-dimensional model fails to capture the pressure loss for this constriction. Increasing $\gamma$ to the frequently used value of 9 only partially improves the prediction.

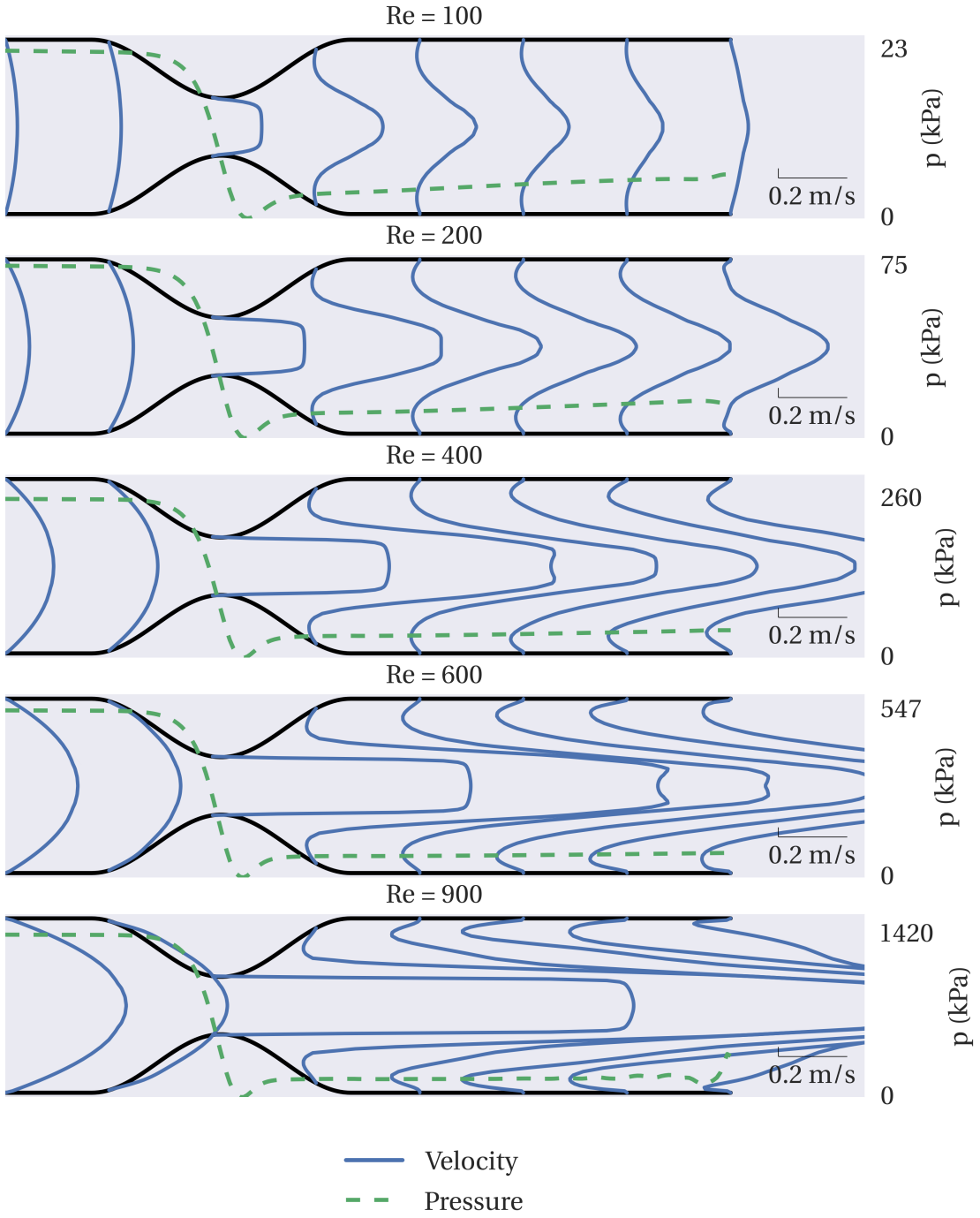


Figure 3.6: Velocityprofiles and pressure in severe (89 %) stenosis, from OpenFOAM simulations.

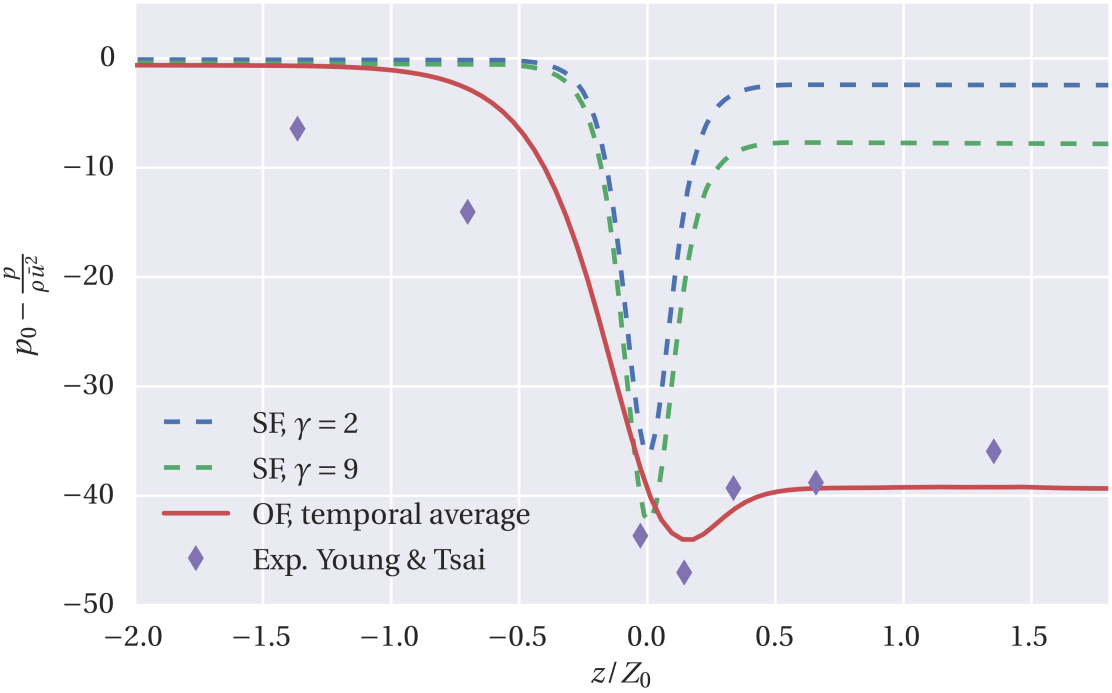


Figure 3.7: Dimensionless pressure drop plotted against axial location. Stenosis length is $2Z_0 = 8R_0$, and $z = 0$ is set at the location of the smallest cross sectional area.

## 3.3 Adding Lumped Model to STARFiSh

From the results in the previous section, it is clear that 1D analysis alone cannot accurately predict the pressure loss over a stenosis. Increasing gamma to flatten the velocity profile is not an acceptable method for cases where dissipation of energy is primarily due to other effects than wall friction.

However, for clinical practice, computational time is critical, and the one-dimensional computations run in a fraction of the time needed for a 3D CFD simulation. With this in mind, efforts were taken to improve the one-dimensional code. This was done by implementing a lumped model from section 2.5. For simplicity and coherence with the case studied in this chapter, the model proposed by Young and Tsai was chosen. Equation 2.68 has been implemented as an addition to the equations linking together two vessel segments in STARFiSh.

The basic idea is to modify the continuity of mass and pressure forces in the links by adding a computed pressure drop as:

$$p_1 + \frac{1}{2}\rho \bar{u}_1^2 = p_2 + \frac{1}{2}\rho \bar{u}_2^2 + \Delta p_{stenosis} \tag{3.1a}$$

$$Q_1 = Q_2 \tag{3.1b}$$

Where subscript 1 denotes the upstream vessel and subscript 2 denotes the downstream vessel.

In STARFiSh, the junctions are solved computed in a non-linear way, to also ensure continuity in the wave propagation. We let $\omega_1$ and $\omega_2$ represent the characteristic variable for each vessel. Superscript 1 indicates a forward propagating characteristic, while superscript 2 indicates a backwards traveling characteristic.

$$\omega_1^2(x_1, t^{n+1}) = \omega_1^2(x_1 - \Delta x_1, t^n) \tag{3.2a}$$

$$\omega_2^1(x_2, t^{n+1}) = \omega_2^1(x_2 + \Delta x_2, t^n) \tag{3.2b}$$

Equations 3.2 ensures the continuity of the propagating characteristic variables. For the steady solutions sought in the present study, these equations could have been neglected, but

are for consistency with the existing code included. Equations 3.1 and 3.2 now make up a system of four equations and four unknowns.

In STARFiSh, the pressure and flow equations are discretized using the characteristic variables, thus the number of unknowns reduces from four to two, namely $\omega_1^2$ and $\omega_2^1$. Using a **LR**-decomposition of the system matrix in Eq. 2.31, the pressure and the flow are discretized in the characteristic variables.

The equations to be solved at each vessel interface are then

$$Q_1 + R21_1\Delta\omega_1^1 + R22_1\Delta\omega_1^2 = Q_2^n - R21_2\Delta\omega_2^2 \tag{3.3}$$

for the continuity of mass, and

$$\begin{aligned} &p_1^n + R11_1\Delta\omega_1^1 + R12_1\Delta\omega_1^2 + \rho\frac{1}{2}\frac{\left(Q_1^n + R21_1\Delta\omega_1^1 + R22_1\Delta\omega_1^2\right)^2}{A_1^2} = \\ &p_2^n + R11_2\Delta\omega_2^1 + R12_2\Delta\omega_2^2 + \rho\frac{1}{2}\frac{\left(Q_2^n + R21_2\Delta\omega_2^1 + R22_2\Delta\omega_2^2\right)^2}{A_2^2} + \Delta p_{stenosis} \end{aligned} \tag{3.4}$$

for the continuity of the pressure, where $R11$, $R12$, $R21$ and $R22$ are the elements of the right decomposition matrix of the **LR** decomposition of the matrix **M** from Eq. 2.32.

$\Delta p_{stenosis}$ is calculated with Eq. 2.68, using the mean area of the upstream and downstream vessel to determine the mean velocity over the stenosis.

As Eqs. 3.4 are non-linear for $\omega_1, \omega_2$, they must be solved iteratively. In STARFiSh, this is done using Newton-Rhapson iterations. This worked fine for simulations with Reynolds' numbers up to approximately 400. Above this, the solution to the equation was not unique, and the iterations oscillated between two values. Adding an under-relaxation factor to the differentiated term in the Newton-Rhapson procedure solved this problem, although the maximum number of iterations had to be increased from 30 to 100 to ensure the desired accuracy of residuals below $10^{-4}$. This procedure was employed for all cases considered in the present study.

### 3.3.1 Hybrid Model Results

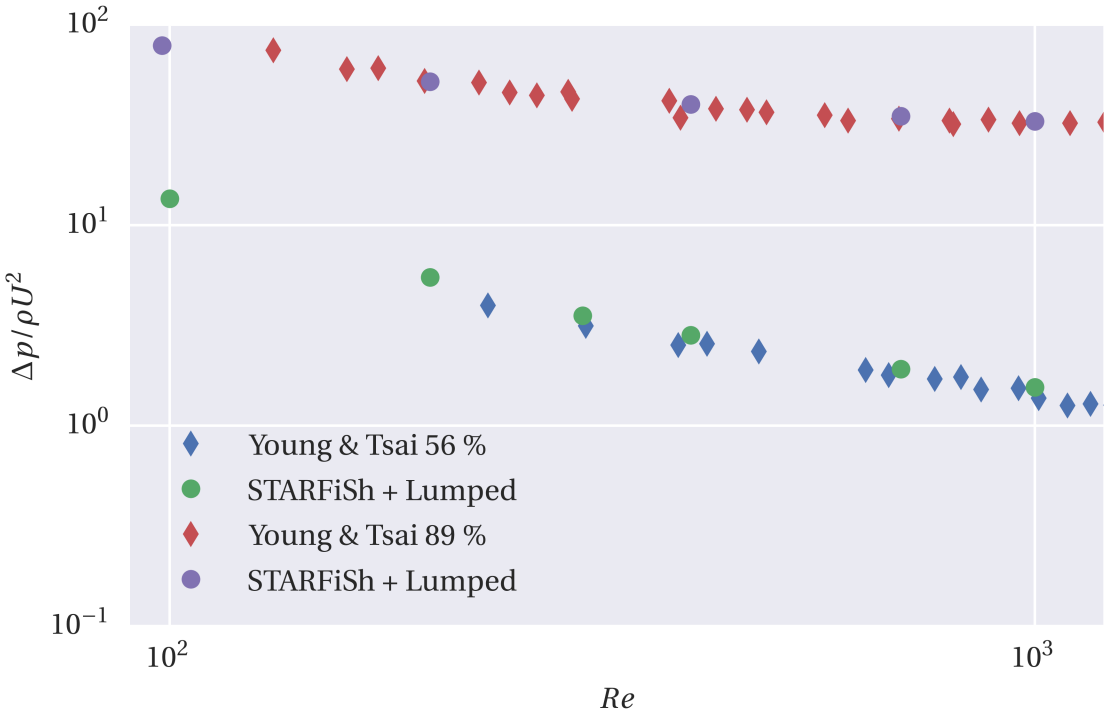


Figure 3.8: Dimensionless pressure drop across stenosis, for both mild (56 %) and severe (89 %) stenoses, after adding a lumped model to STARFiSh.

From figure 3.8, the improved correlation to experimental results is prominent, comparing with figure 3.5. Note that all simulations here were run in STARFiSh with a shape parameter of 2, corresponding to a Poseuille profile. The shear stress in the tubes upstream of the stenosis is then correctly predicted, while the stenotic pressure jump and the recovery zone down stream is captured by the lumped approximation. This result is very much expected, as the lumped model included in STARFiSh was the empirical correlation given by Young and Tsai for the presented experimental data. However, it is critical to validate new implementations, and this results show that the implementation is correct for the Reynolds' numbers considered. The implementation did not increase the computational time significantly, all the time only one stenotic link was studied.

## 3.4 Summary and Discussion

### Summary

One-dimensional modeling of stenotic flows can be feasible for low and moderate Reynolds numbers when the stenotic regions are long and diffuse, where the wall friction gives the dominating contribution to the pressure drop. For more abrubtly changing geometries and or with higher Reynolds' numbers, will the pressure loss be underestimated, as energy dissipation in vortices and separated regions is not accounted for. This can be included in the one-dimensional analysis as a lumped model for the pressure jump across the stenosis, with a normal 1D approach on each side. This has been demonstrated for both a mild and a severe stenosis, for a range of Reynolds' numbers, and shown to agree very well with experimental results reported in the literature.

3D CFD gives accurate pressure drops compared with the experimental findings, but for the severly restricted stenosis, the laminar flow hypothesis is somewhat violated in the region downstream of the stenosis.

### Discussion

The way of changing $\gamma$ to achieve desired wall friction may seem like imposing strict assumptions on the flow. However, changing this parameter is common in the literature, where values ranging from 1 to 9 have been proposed [3, 7]. In these studies, however, the viscous pressure drop has not been the primary interest. Formaggia et al. [24] suggests decoupling the friction from the momentum correction, giving each vessel a viscous resistance equal to the Poseuille resistance, and specifying a value for $\gamma$ to give an adequate momentum correction. This decoupling indicates that a lumped pressure resistance model can be included without altering the wave characteristics of the system excessively.

Simulation of transitional flows are a complex field [**?** ], and in the present study, turbulence modeling of the stenotic flows where not pursuaded further, as the temporal averaging method yielded satisfactory correlation between the overall pressure drop for the simulation and the experimental data. For global intesive properties such as pressure, this can be sufficient. If,

on the other hand, a more detailed description of the flow field was sought, for instance the distribution of wall shear stress, a more advanced simulation would be required.

Grid refinements could have been done beyond the 1.5 million cells mesh, but as the overall pressure drop was the variable of interest, showing little variance from the coarser meshes at low Reynolds' numbers, and good agreement with experimental data for higher Reynolds' numbers, this was not pursued further.

However, the computational domain could have been extended to avoid the backflow in the domain, which causes an unknown forcing of the solution in the domain. However, it is not such an extension would need to be at least twice as long as the existing geometry, according to reattatchmenth lengths for disturbed flows at Reynolds numbers similar to the ones in the present study, reported by Back and Roschke [4]. As fairly good agreement with the experimental results was obtained with the approach taken, such an extension was not tested.

# Chapter 4

# Patient Specific Geometry

In this chapter, the coronary arteries from a 68-year-old male subject are analyzed. First, the segmentation of the CT image to produce geometric models for numerical simulations is presented. Later, the physiological conditions that form the boundary conditions are discussed. The model parameters used in STARFiSh and OpenFOAM are then listed, and the preparation of the geometry for use in the one-dimensional and the hybrid model is elaborated. Finally, the results are presented and discussed.

## 4.1 Segmentation

Segmentation describes the process of transforming medical images into 3D models suitable for meshing and computation. The procedure is described briefly in this section.

Anonymous CT-images of the coronary anatomy was received from the St. Olav's University Hospital in Trondheim. Images were acquired using a flash protocol, where the entire chest region is captured in the same diastole period, without the need of merging pictures from different heart cycles. Images reconstructed using two distinct algorithms, filtered back projection (FBP) and iterative reconstruction (IR) were received.

In this study, the images using iterative reconstruction are used for the analysis. The decision to use IR-images was based on very promising iso-surfaces extracted from these pictures, shown in figure 4.1. The IR image captures more details of the LAD and CX, and even daughter branches of these, while the FBP only identifies the main branch of the LCA. The IR image did, however,

contain more grainy noise, and a clutter removal filter has been applied to the isosurface shown in the right panel of figure 4.1.

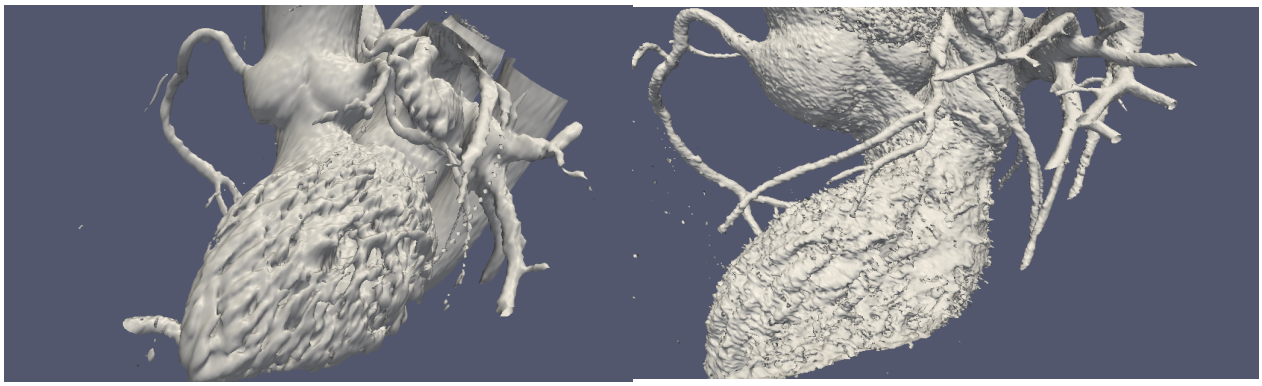

Figure 4.1: Isosurfaces of CT images using FBP (left) and IR (right).

Segmentation was done in VMTK - The Vascular Modeling Toolkit. The segmentation process relies on level set segmentation, as described briefly in section 2.6. Initialization was performed with the colliding fronts algorithm. The algorithm showed capable of initializing vessel segments of approximately 5-10 mm, without collapsing the surface. Thus, a number of such initializations were performed, before the final surface was created by solving the level set surface propagation equation, Eq. 2.72.

The author of VMTK, Luca Antiga, gives recommendations for the parameters, both in his thesis [1] and in the online tutorial [67]. Values of 0, 0 and 1 for the weights $w_i$ in Eq. 2.72 are recommended and are default values in VMTK. This is equivalent to prescribe no model inflation, no limitation on curvature, and only advection scaling by a function inversely proportional to the image intensity. These settings are claimed by Antiga to give a robust and accurate segmentation surface.

For the IR images segmented in this study, those settings did not give satisfactory results. This might be due to the grainy noise, where small regions gets unphysical values of image intensity. Basing the segmentation only on the advection of the image intensity, led the segments to collapse and caused irregular shapes, which in turn resulted in bad quality meshes, if meshing was even possible at all.

To overcome this, the advection weighting was set to 0.8, while the curvature and the inflation scaling was increased from 0 to 0.3 and 0.2 respectively. This caused the segmentation to

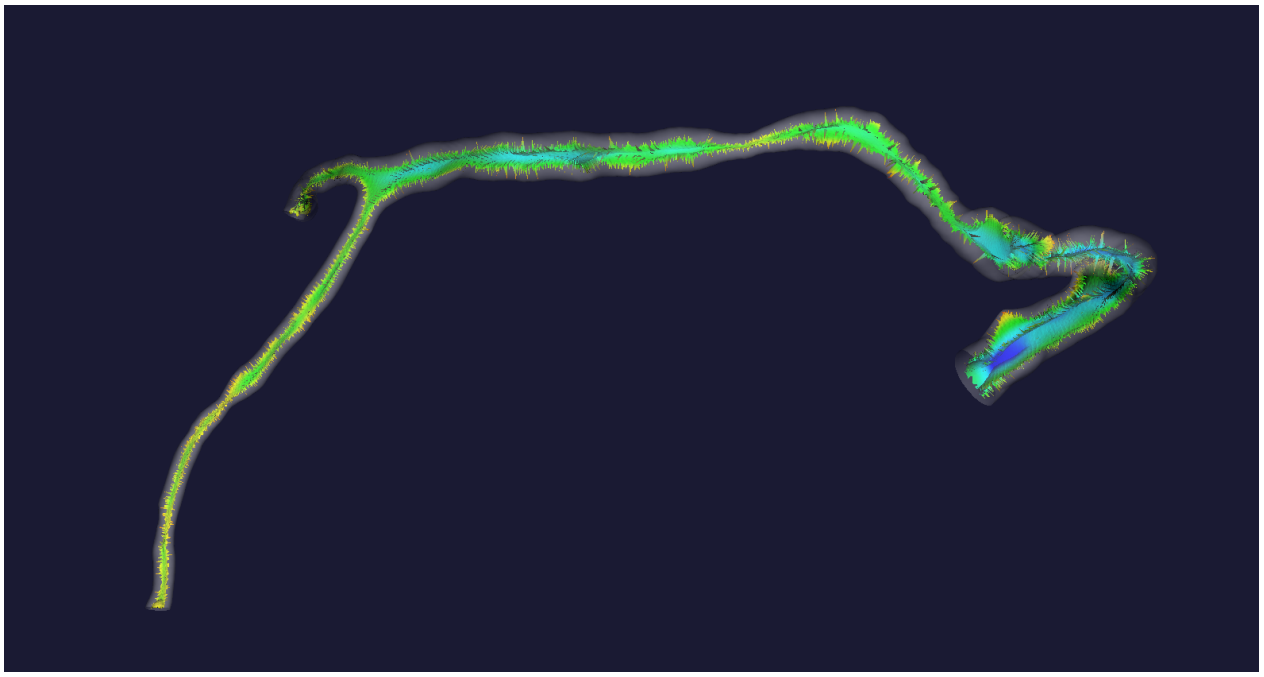

Figure 4.2: Voronoi diagram of a RCA, showing the maximum inscribed sphere radius at all points along the centerlines. The centerlines in turn are computed as the center of the maximum inscribed sphere at all points. Notice the irregularity of the radius.

be much more robust, but does introduce more smoothing, with the possibility that significant geometrical features get lost. Comparing the surfaces reconstructed in this study with those shown in multicenter diagnostics studies, shown for instance in Taylor's 2013 paper [58], or the models shown by Secchi et al. [53], the smoothing induced by the curvature and inflation scaling in the present work does not seem excessive.

After reconstructing the 3D vascular segment, the centerlines was computed as the line through the centers of all inscribed spheres of maximum radius in the segment. The radius data along the centerline was extracted to be used for the 1D simulations. VMTK provides functionality to perform all these operations, in addition to surface preparation and meshing for CFD. Figure 4.2 shows a segmented RCA, with an inscribed centerline and a voronoi diagram showing the radius of the maximum inscribed sphere at all points.

## 4.2 Physiology

After the segmentation, the geometry of the computational domain is known. However, no measurements of the physiological flow conditions have been made. The flow rate in each vessel must therefore be estimated. Using empirical data found in the literature, estimates for the flow rates in the three main branches of the coronary circulation can be made.

In resting conditions, the cardiac circulation comprises around 5 % of the total cardiac output [49]. Cardiac output is dependent on body mass, sex, age and other factors. In this study, a value of 5 L/min is used, in agreement with the literature for men's average cardiac output at higher ages [39]. Thus, a total coronary circulation of 250 ml/min is obtained for all the branches. Ross et al [52] reports a mean flow split of 55 % in the LCA and 45 % in the RCA, and these values are used in the present study. For the flow division between the LAD and the CX the literature showed more variance, but all of the consulted references had measured a higher flow rate in the LAD compared to the CX.

Initially, Murray's law on the form of Eq. 2.64 was applied to the entire LCA tree, with a constant $c$ equal to 3. This gave however a flow rate division between the CX and LAD of 70 % in the CX and 30 % in the LAD. As no support for this distribution was found in the literature, this approach was rejected.

The source of error in this estimation method may be due to more arterioles branching off the LAD into the myocardium wall, which are not included in the segmentation, and/or that the image gradients in the CX led to an unrealistic surface inflation here, yielding outlets larger than in reality.

Reducing the Murray constant did reduce the difference in flow rates, but even at the lowest value found in the literature, $c = 2.27$ [64], more than 60 % of the flow was predicted in the CX. To overcome this, the flow rate was specified to be evenly distributed between the two branches. As simulations will be performed at multiple flow rates, such a split gives a straightforward way of finding the explicit flow in the main branch of the LAD and the CX respectively.

Murray's law was then applied to both the CX and the LAD separately, to calculate the intra-branch flow divisions, again with constant $c = 3$. For the RCA, Murray's law was applied directly.

Flow rates at resting conditions are now established. However, the body's response to vasodi-

lation shows huge individual variance, as described in section 1.3. As the response is unknown, the flow rate is essentially also unknown. In the present study, simulations will be performed under resting conditions, and with flow rates equal to 2, 3 and 4 times the flow rates at rest, keeping the flow division between the branches equal to the resting state. The method of keeping flow division constant and increasing the total flow rate is reported by Taylor et al. [58] in the scientific basis for three of the largest multicenter studies using CT-FFR [35, 40, 45] presented to date.

Then, knowing the invasively measured FFR, the correct flow rate can be estimated as the flow rate giving the FFR prediction closest to the measured FFR. This is the case for the LAD where in invasive FFR measurement has been done. For the RCA, no such measurement has been done.

The vasodilation response in RCA was shown in section 1.3 to be 2.9 times the resting flow rate. However, applying such a flow rate to the RCA in question would lead to Reynolds' numbers approaching $10^4$ in the stenosis, and FFR values below 0.2 was calculated for this response. With this in mind, the empirical flow rate for the RCA was taken as non-physiological. As QCA had been reported on this branch, yielding a 40 % DS, regarded to be non-significant, the FFR value of 0.2 is clearly unrealistic.

Instead, the predicted flow rates were divided by two. This approach led to calculated FFR values ranging from 0.9 to 0.2. The reasons for the errors associated with literature flow rate values can be several, and will be discussed in the end of this chapter.

Although the physiological realism of the flow conditions in the RCA are unclear, simulations performed on this geometry will provide useful validation of the lumped model, as the selected flow rates and Reynolds' numbers will be representative for the CT-FFR problem.

A summary of the volumetric flow rates and the Reynolds' numbers at the branch inlet and at the point of smallest cross section is tabulated in table 4.1. This is done for conditions at rest, and for the case of severe hyperemia corresponding to a hyperemic flow rate four times the resting flow rate, and represents the extremities of the flow rates investigated in the present study.

| Branch | $d_{in}$ (mm) | $d_{st}$ (mm) | State | Flow rate (ml/min) | $Re_{in}$ | $Re_{st}$ |
|---|---|---|---|---|---|---|
| LAD | 3.4 | 1.43 | R | 68.8 | 409 | 972 |
| | | | H | 275.0 | 2045 | 3885 |
| CX | 3.55 | 1.78 | R | 68.8 | 125 | 249 |
| | | | H | 275.0 | 498 | 994 |
| RCA | 2.25 | 1.14 | R | 56.3 | 505 | 996 |
| | | | H | 225.0 | 2020 | 3984 |

Table 4.1: Branch dimensions, flow rates and Reynolds' numbers for resting (R) and maximal hyperemia (H), set equal to 4 times the resting flow rate. Subscript *st* denotes the minimum (stenotic) diameter on the main branches.

## 4.3 Setup

### 4.3.1 OpenFOAM

#### Meshing

The 3D segments was meshed with a radius dependent mesh, using tetrahedral cells. A grid size of 2.3 million cells was chosen for the LCA, for which the pressure along the centerline differed less than 0.5 % from a simulation with 7.2 million cells. A resolution of 2.3 million cells was chosen as sufficient to achieve grid independent solution for the pressure field.

The RCA was similarly meshed with a total of 1.5 million cells, sufficient to get pressure data along the centerline within 0.5 % from the results from a simulation with a refined mesh of 5.7 million cells.

The grid independency simulations were run for a flow rate equal 412.5ml/min in the LCA, and a flow rate of 225 ml/min in the RCA.

#### Boundary Conditions

At the outlets, a parabolic velocity profile was specified, corresponding to the flowrates for resting and hyperemic conditions as described in section 4.2. The parabolic outlet is justified by the fact that the segmented artery has been extended at all outlets, to keep boundary condition influence small in the domain of interest. The extensions evolve to uniform pipe segments, so a parabolic velocity profile does not induce slip conditions or other artifacts at the outlet. A proximal pressure of 100 mmHg was specified at the inlet, while a zero-gradient condition

was specified at each outlet. At the wall, a zero-gradient was set for the pressure, and a no-slip condition applied for the velocity.

#### Solver Configuration

The solver employed was the OpenFOAM application simpleFoam, a steady state solver, using the SIMPLE pressure correction method described in section 2.1.3. A linear central space scheme using Gauss integration points was used for the laplacian terms and the gradient terms, and a second order upwind scheme for the divergence terms. The solution was initialized from a zero velocity field, and the iterations under-relaxed by a factor of 0.7 for the velocity and 0.3 for the pressure. The solution was iterated until all residuals was below $10^{-3}$.

The required computational time ranged from around 1 CPU hour for the normal simulations, and up to 7 CPU hours for the grid independency simulations. This is a faster solution time per cell than for the generic stenosis geometries, and can be due to OpenFOAM's built in method for renumbering the mesh, which searches to minimize bandwith in the final matrix of the algebraic equation system. For long, tubelike structures such as blood vessels, this is more effective than for the relatively shorter and wider domain used in Chapter 3.

### 4.3.2 STARFiSh

For the one-dimensional simulations, only the cross sectional area and the arc length of the vessel centerline is needed. They are extracted from the 3D surface using VMTK's built in functions, as vectors containing radius and abscissa data. As the sampled signal is very irregular, as it is seen from figure 4.2, a VMTK's bulit in smoothing function was applied to the centerlines. This function uses a simple moving average filter to remove small variations. As STARFiSh requires a equispatial grid for the axial coordinates, the radius vector is interpolated to a uniform grid. Both the main trunk of the LCA and the LAD main branch is included. This will result in a flow rate in the common LCA only half of the real flow rate, but as the pressure loss is minimal in this segment even in 3D simulations at maximum hyperemia, no intolerable error is induced by this simplification.

To ensure comparability with the results from 3D CFD, rigid walls were prescribed in STARFiSh, but it is emphazised again that STARFiSh contains effective models for wall compliance, and in

1D, the additional computational cost associated with including fluid-structure interaction effects is affordable.

As boundary conditions, the incoming volumetric flow rate was presicribed as a ramped sine signal, and at the outlet, a simple flow resistance was prescribed. When running rigid wall simulations in STARFiSh, the flow will, as in incompressible CFD simulations, only be dependent on the pressure gradients, and thus, the magnitude of the rpesure in the domain is not important. In the postprocessing, the pressure drop was calculated and a FFR value was computed, using an assumed proximal aortic pressure of 100 mmHg as the reference.

The STARFiSh simulations on patient specific geometry required around 5 min of CPU time to converge to a steady solution, with 30 % of this time being used to simulate the ramping of the incoming flow, and the last 70 % reaching a steady state solution.

### 4.3.3 STARFiSh with lumped model

From the promising results of adding a lumped model to STARFiSh for the generic geometries, the same approach was taken on the patient specific geometry. For these simulations, somewhat higher CPU-times was needed, as more iterations in the linking equations loop was necessary. Still, the total simulation time including initialization was below 10 minutes for all cases, on a 2.5 GHz processor.

In contrast to the purely one-dimensional simulations, in which the fully patient specific geometry was used, a simpler parametric approach were taken in the hybrid cases. Upstream and downstream of the stenosis, uniform pipes with the mean diameter of the upstream and downstream segments was modeled, a strong simplification. The flow rate was varied, and as the stenosis is in the link between two vessel segments of different cross sectional area, the mean bulk velocity of the two vessels was used in the pressure drop equation implemented. In the future, the two modeling methods can be joined togehter, but this was not possible in the present study. Still, the results are compared, as they both treat the same coronary arteries, building the computational domain from geometrical parameters.

**Stenosis detection**

For the hybrid simulations combining 1D and lumped models, stenosis parameters has to be extracted from the diameter data. To ensure consistency and repeatability, this was done automatically, by an own-developed method.

1. Local maxima and minima were extracted from the diameter vector. All local minima was treated as candidate stenoses.

2. In the case of fewer local maxima than minima, the endpoints were either disregarded as minima, or included as maxima. This ensured that the number of maxima was one above the number of minima.

3. The stenosis degree for all candidate constrictions was then calculated as the ratio of the local minimum cross sectional area to the average cross sectional area of the two neighboring maxima.

4. Only stenoses with a reduction in cross sectional area larger than 56 % was considered relevant for lumped modelling, as this was the smallest stenosis degree validated by Young and Tsai.

The stenosis length was calculated as half the distance between the two neighboring maxima. The healthy segments was modelled using the mean radius of the segment. As Young and Tsai only provided equation coefficients for two cases, namely 56 % and 89 % area reduction, a simple linear interpolation was used to get constants for the cases in between.

For the LAD in question, the above presented analysis led to one significant stenosis, with an area-reduction of 68 %, and a stenosis length of 7.6 times the mean of the upstream and downstream healthy radiuses, respectively.

For the RCA, a two significant stenoses was detected by this method, one with an area reduction of 56.6 % and a length of 3.8, and another at 64.1 % area reduction and a length of 3.4.

An illustrative plot of the method can be found in figure 4.3 for the LAD and in figure 4.4 for the RCA. Corresponding tables listing the properties of the candidate stenoses are shown in table 4.2 and 4.3 for the LAD and RCA, respectively.

The stenosis lengths was here in the same range as the ones considered by Young and Tsai.

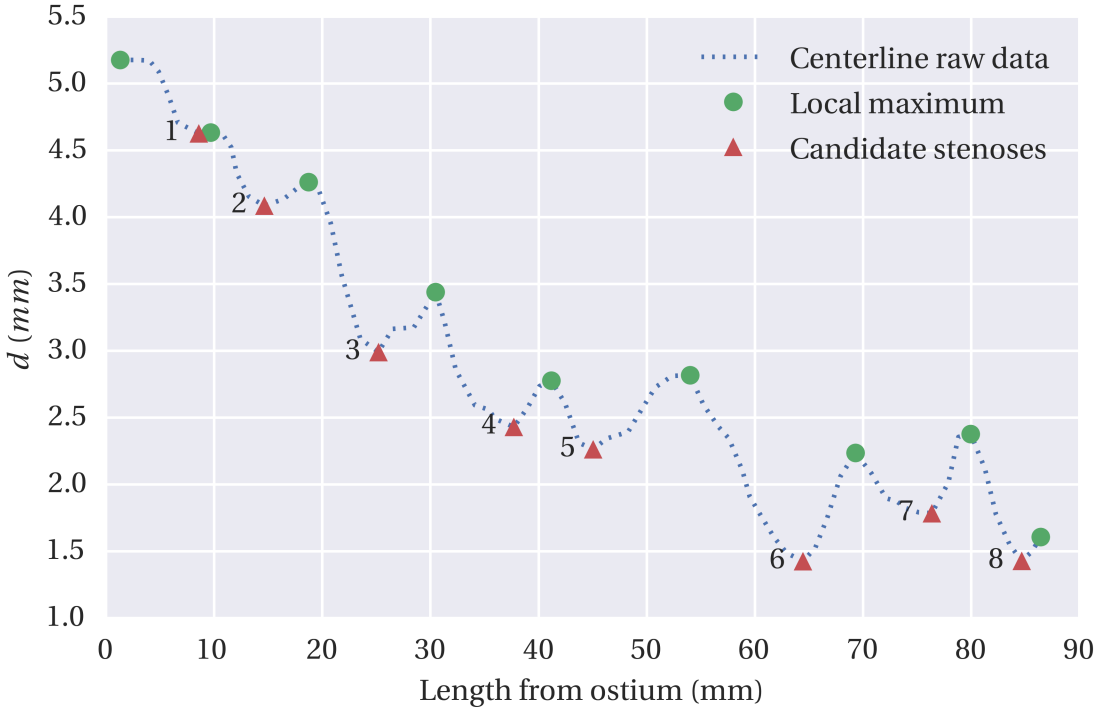


Figure 4.3: Extracted centerline diameter data with candidate stenoses in the LAD.

| Nr | $d_0$ (mm) | $d_{st}$ (mm) | AS (%) | LS/$d_0$ |
|---|---|---|---|---|
| 1 | 4.90 | 4.63 | 11.0 | 4.2 |
| 2 | 4.45 | 4.08 | 15.7 | 4.5 |
| 3 | 3.85 | 2.99 | 39.7 | 5.9 |
| 4 | 3.11 | 2.43 | 38.9 | 5.3 |
| 5 | 2.80 | 2.26 | 34.6 | 6.4 |
| 6 | 2.53 | 1.43 | 68.2 | 7.6 |
| 7 | 2.31 | 1.78 | 40.2 | 5.3 |
| 8 | 1.99 | 1.43 | 48.6 | 3.2 |

Table 4.2: Parameters for candidate stenoses in LAD. $d_0$ is calculated as the mean of the two surrounding maximas, $d_{st}$ is the local minimum diameter. Area Stenosis (AS) is the relative cross sectional area reduction, and LS the stenosis length, calculated as half the distance between the two surrounding maximas, here tabulated normalized to $d_0$.

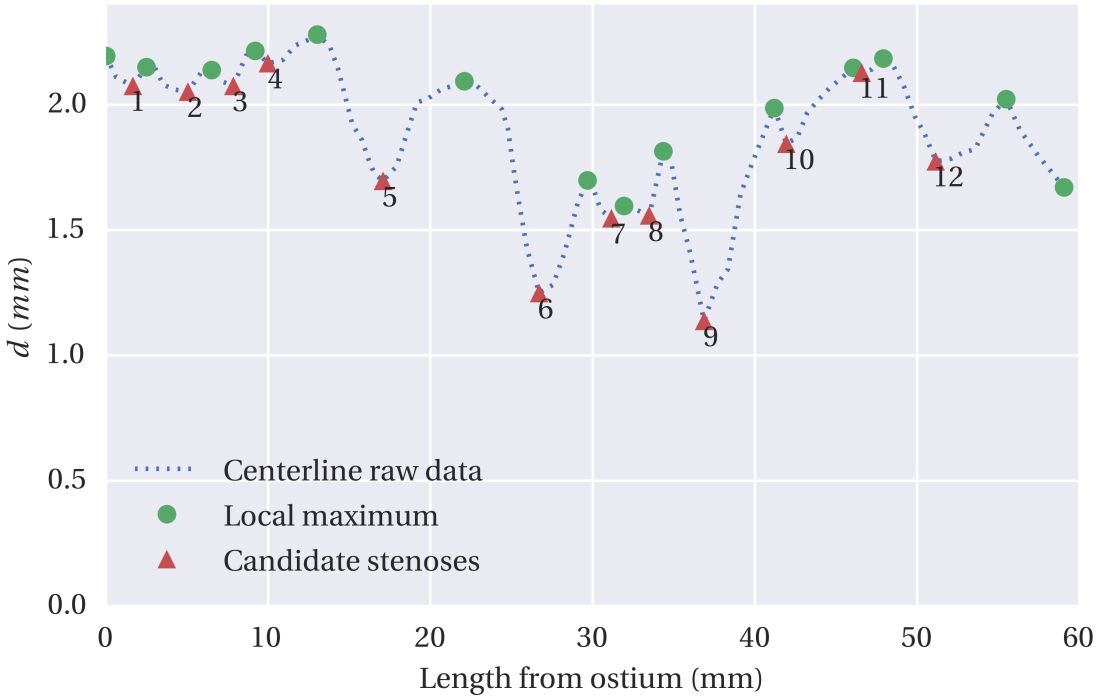


Figure 4.4: Extracted centerline diameter data with candidate stenoses in the RCA.

| Nr | $d_0$ (mm) | $d_{st}$ (mm) | AS (%) | LS/$d_0$ |
|---|---|---|---|---|
| 1 | 2.17 | 2.08 | 8.8 | 1.2 |
| 2 | 2.14 | 2.05 | 8.4 | 2.0 |
| 3 | 2.18 | 2.08 | 9.1 | 1.3 |
| 4 | 2.25 | 2.17 | 7.2 | 1.9 |
| 5 | 2.19 | 1.70 | 39.9 | 4.5 |
| 6 | 1.90 | 1.25 | 56.6 | 3.8 |
| 7 | 1.65 | 1.55 | 11.8 | 1.1 |
| 8 | 1.71 | 1.56 | 16.6 | 1.2 |
| 9 | 1.90 | 1.14 | 64.1 | 3.4 |
| 10 | 2.07 | 1.85 | 20.4 | 2.4 |
| 11 | 2.17 | 2.13 | 3.5 | 0.9 |
| 12 | 2.10 | 1.77 | 28.8 | 3.8 |

Table 4.3: Parameters for candidate stenoses in the RCA. $d_0$ is calculated as the mean of the two surrounding maximas, $d_{st}$ is the local minimum diameter. Area Stenosis (AS) is the relative cross sectional area reduction, and LS the stenosis length, calculated as half the distance between the two surrounding maximas, here tabulated normalized to $d_0$.

## 4.4 Results

The main results in this section are the computed FFR values downstream of the stenoses detected and described in the previous section. Three modeling strategies are compared. The 3D CFD are here taken as the ground truth, as the method yielded very close agreement with experimental data on similar geometries in chapter 3, and yielded a physiologically realistic flowrate for the FFR measured in the LCA. For the RCA, the physiological flow rates obtained from the literature resulted in FFR values well below what is called ischemia causing, meaning a stroke would occur. Thus, the RCA was simulated using flow rates that resulted in FFR calues spanning from 0.92 to 0.30 in the 3D CFD case, and used to compare the different simulation strategies against each other.

| Vessel | Q (ml/min) | $FFR_{OF}$ | $FFR_{Hybrid}$ | $FFR_{SF}$ |
|---|---|---|---|---|
| LAD | 68.80 | 0.96 | 0.96 | 0.96 |
| | 137.50 | 0.91 | 0.91 | 0.94 |
| | 206.25 | 0.83 | 0.83 | 0.88 |
| | 275.00 | 0.74 | 0.76 | 0.84 |
| RCA | 56.25 | 0.92 | 0.90 | 0.95 |
| | 112.50 | 0.76 | 0.78 | 0.89 |
| | 168.75 | 0.54 | 0.64 | 0.84 |
| | 225.00 | 0.30 | 0.49 | 0.79 |

Table 4.4: Predicted FFR values downstream of most severe stenosis in the two branches analyzed. Threshold for invasive treatment is normally set at FFR = 0.8.

### 4.4.1 Left Coronary Artery

The computed FFR for the Left Coronary artery is shown in figure for different flow conditions. The FFR distal to the lesion in the main branch is almost 1 for resting conditions, decreasing to 0.75 for a flow rate four times the resting flow rate. The clinically measured FFR for this branch was 0.85, indicating that the flow in the whole LCA would be around 400 ml/min at the time of measurement, or a response to vasodilation resulting in an increased flow approximately three times the resting flow. This response is in agreement with values from the literature, presented in section 1.3.

One-dimensional simulation results are plotted together with the hybrid model prediction. STARFiSh alone predicts a FFR value of 0.96, 0.93, 0.89 and 0.84, for resting conditions and flow rates increases of 2, 3 and 4 times the resting flow rate, respectively. Including the lumped model on the simplified parametric geometry of the vessel, gives a prediction that follows the 3D CFD predictions closely, except for the case of maximum flow rate, where the hybrid model overpredicts the FFR value with a magnitude of 0.02.

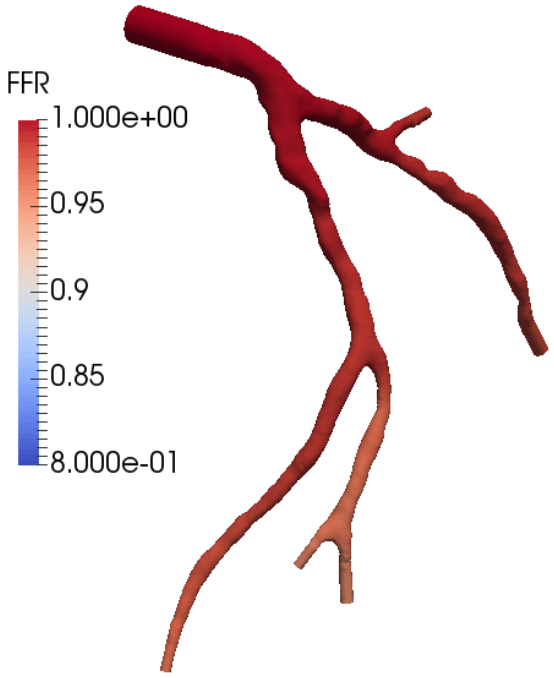


(a) $Q = Q_{rest}$

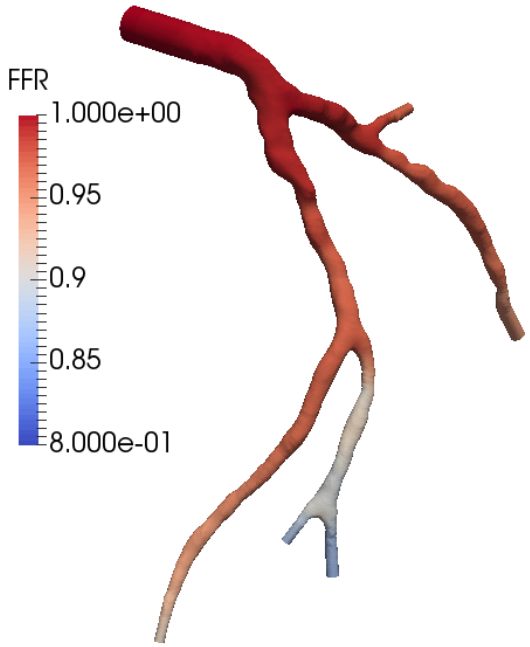


(b) $Q = 2Q_{rest}$

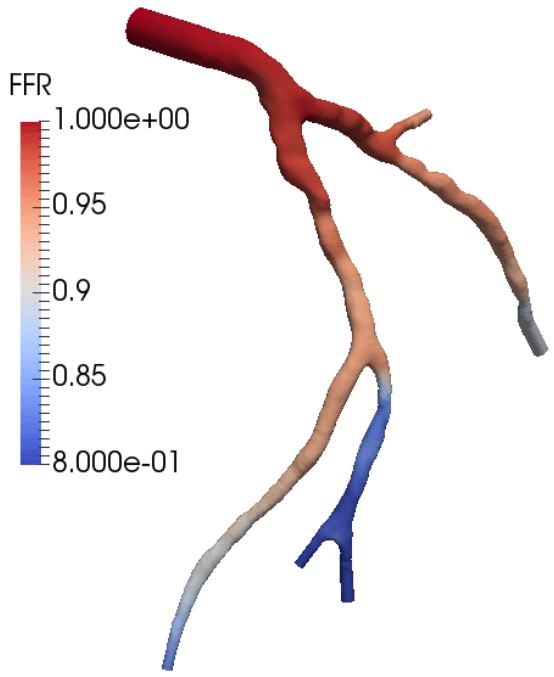


(c) $Q = 3Q_{rest}$

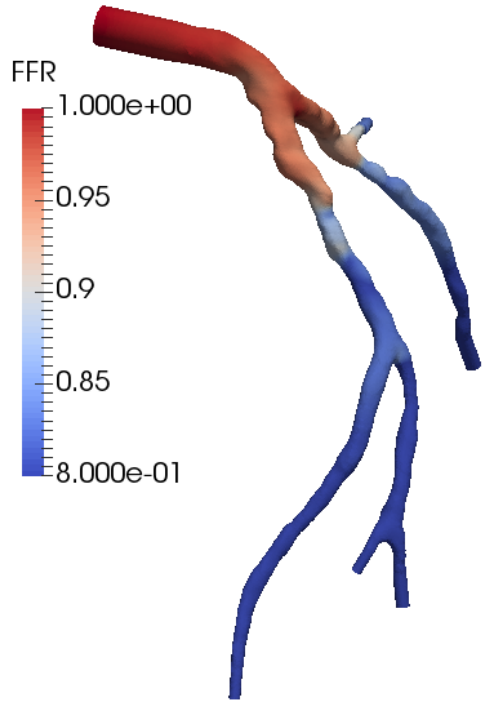


(d) $Q = 4Q_{rest}$

Figure 4.5: FFR in LCA branches at different flow conditions.

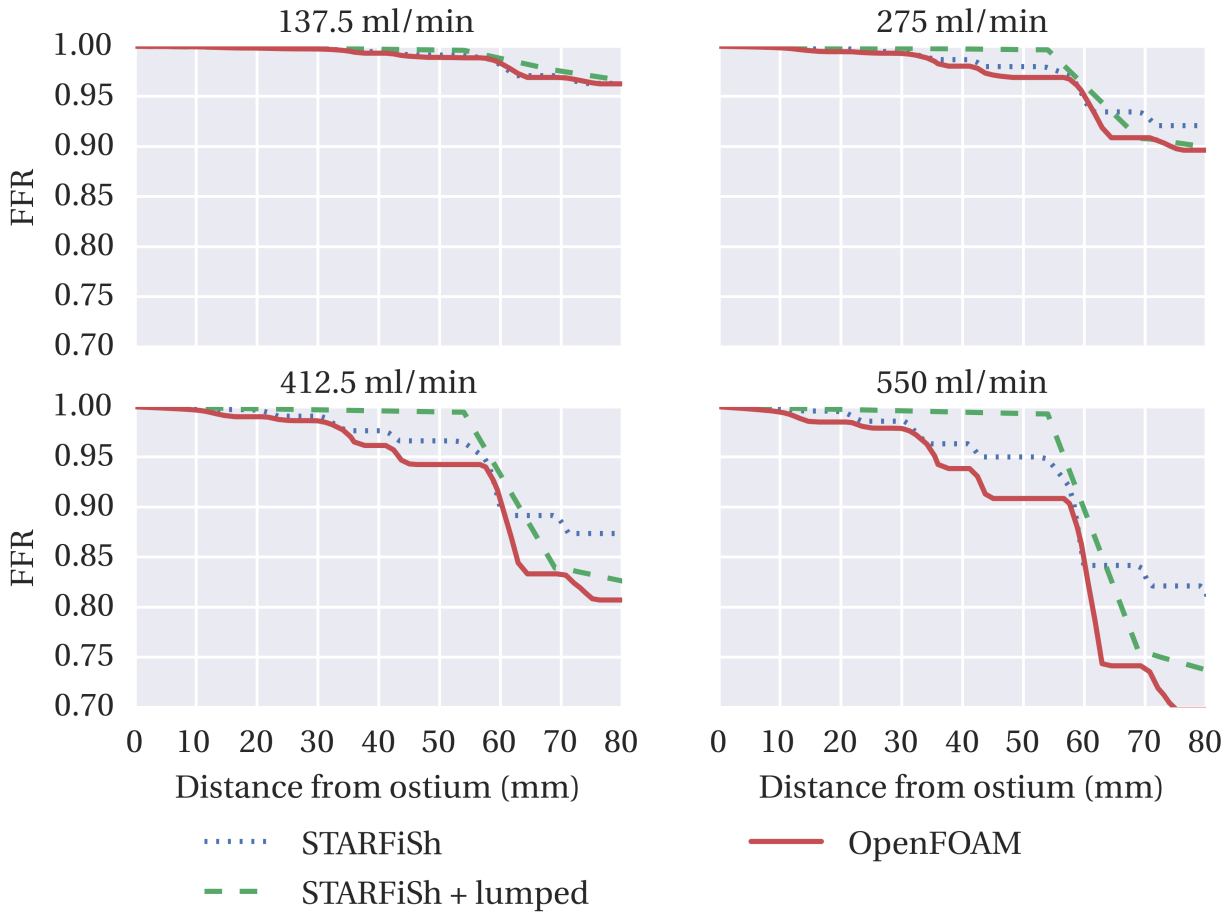


Figure 4.6: Computed FFR in main branch of LAD for different flow conditions, using both 3D CFD, STARFiSh with patient-specific geometry and a hybrid method

### 4.4.2 Right Coronary Artery

A three-dimensional mapping of the FFR values computed in the RCA is shown in figure 4.8. It is noticeable how the FFR value drops abruptly in the visible constriction. For the point right downstream of the most severe stenosis in the right coronary artery, a FFR value of 0.92, 0.76, 0.54 and 0.30 was computed for flow rates equal to 56.25 ml/min, 112.5 ml/min, 168.75 ml/min and 225 ml/min, respectively. Also here, the one-dimensional analysis follows the 3D CFD closely for low flow rates, but fails to capture other dissipative effects than the wall friction.

The lumped model seems to underpredict the first stenosis, while the second is slightly over-predicted. This is more prominent in the two cases of higher flow rates. These flow rates must be regarded as extremities, as a FFR value of below 0.5 is rare in borderline cases typical for CT-FFR. The lumped model does however outperform the 1D model even in these cases, if regarding a FFR value of 0.8 as the limit for whether invasive treatment should be used, then the hybrid model gives the same diagnostic predictions as 3D CFD.

A clinical visual assessment from quantitative coronary angiography suggested a 40 % diameter stenosis, equal to a 64 % area stenosis for a circular vessel. From table 4.3, this is in very close agreement with the most severe of the two significant stenoses detected by the automated criteria, and can support the accuracy of the segmentation.

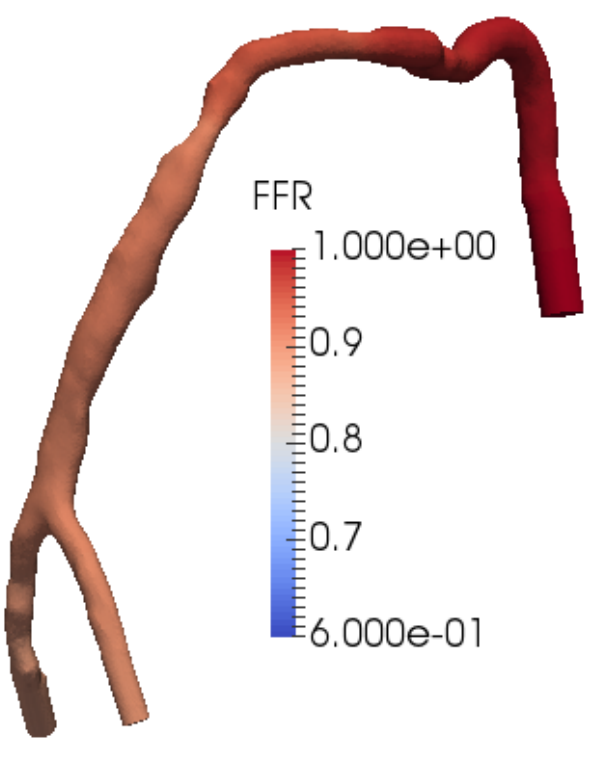


(a) $Q = 0.5Q_{rest}$

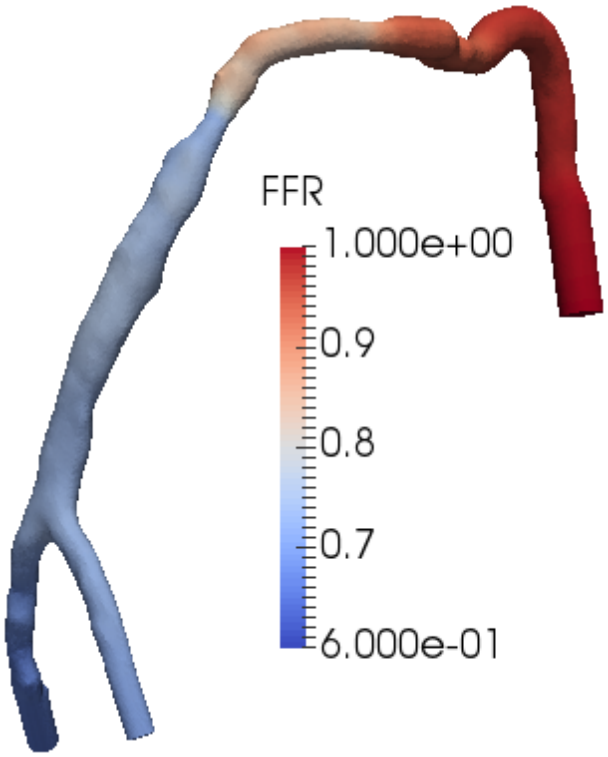


(b) $Q = Q_{rest}$

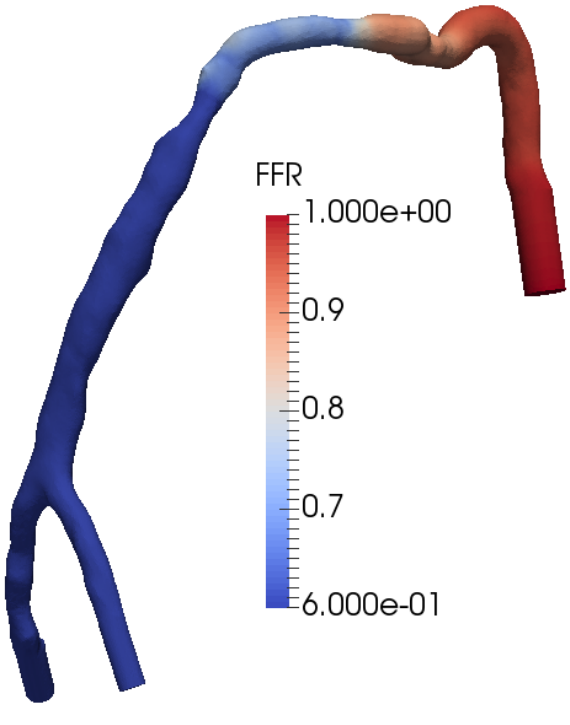


(c) $Q = 1.5Q_{rest}$

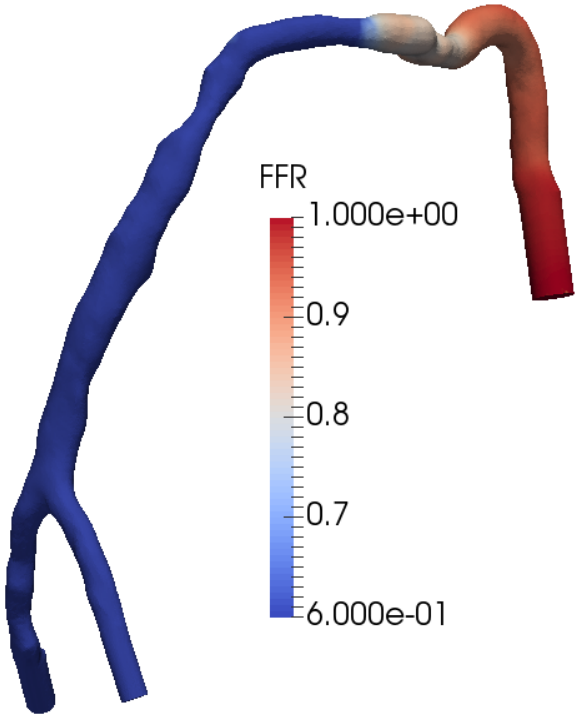


(d) $Q = 2Q_{rest}$

Figure 4.7: FFR in RCA branches at different flow conditions.

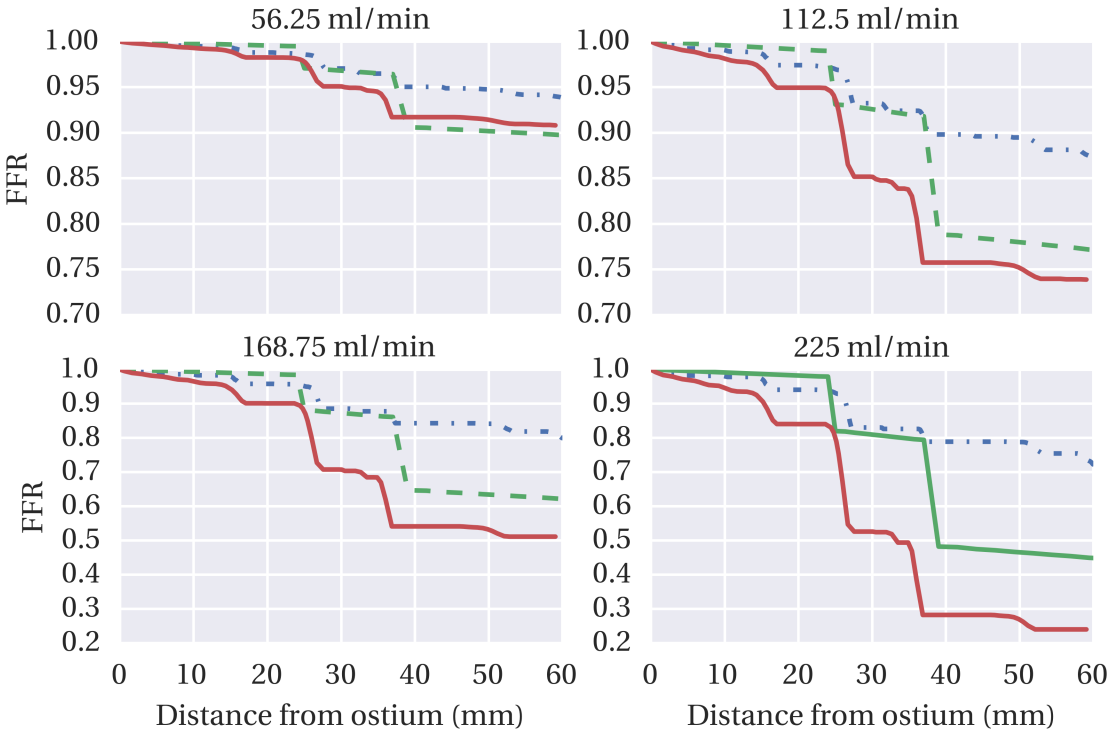


Figure 4.8: Computed FFR in main branch of RCA for different flow conditions, using both 3D CFD, STARFiSh with patient-specific geometry and a hybrid method

## 4.5 Summary and Discussion

**Summary**

In this chapter, the coronary arteries of a male subject was analyzed. As the FFR in the LAD was known a priori from invasive measurements, the incoming flow rate was varied to analyze the vasodilation response of the patient. For the measured FFR of 0.85, a corresponding flow rate of approximately 400 ml/min in the LAD main trunk was found, corresponding to a vasodilation flow rate increase of just be three times the resting flow rate. This is within the ranges reported in the literature.

The one-dimensional hybrid model predicts the pressure drop in the artery remarkably well, using the CFD predictions as a ground truth validated to invasive measurements. This is despite the parametric geometry used in the hybrid simulations being a rough approximation to the vessel geometry.

Combining one-dimensional patient specific vessel data with lumped models for the most severe stenoses looks like a promising strategy for fast and accurate FFR prediction based on CT-imaging. The dependence on the boundary conditions, such as the flow rate, has a greater impact on the FFR prediction than including all three-dimensional effects.

For the RCA, with two stenosis detected by the model, the correlation between the 3D CFD results and the hybrid model was not as good as for the LAD. It seems as the pressure loss in the less severe stenosis is overpredicted, while the loss in the most severe stenosis in underpredicted. This tendency is more prominent in the cases where the 3D CFD simulations yielded a FFR value below 0.5. This is however a flow rate and a pressure loss not likely to be diagnosed by computational FFR, referring to the patients expected in section 1.1.3.

### Discussion

The validity of the results in this section are subject to discussion. First, a convergence criteria of $10^{-3}$ may be regarded as too loose convergence to ensure a fully steady state solution. However, as the

The approximation of blood as a Newtonian fluid induces simplification errors. However, Cho and Kensey [10] reports how pressure drop in arterial vessels are unaffected by non-Newtonian

effects at Reynolds numbers larger than 100. This is supported by the findings from Johnston et al [29, 30], who studied both steady state and transient flow in a right coronary artery, concluding that non-Newtonian effects were only signinficant for a short period of time in the transient solution, in the late diastole where the flow is decellerated and reversed, yielding low velocities and low local Reynolds' numbers.

The assumption of rigid walls is another simplification made, that can have an influence on the solution. Malvé et al [38] claims this to be important for wall shear stress computations, less so for the pressure loss, especially at steady state simulations. This is also supported by Torii et al [61].

No FFR validation was available for the RCA, but a FFR value at hyperemia of 0.2 seemed unlikely. The operator had diagnosed the stenosis to be non-significant, and a value of 0.2 means a stroke or severe ischemia. Flow rates was specified to cover pressure losses corresponding to FFR values of 0.9 to 0.2. Although clinically wrong, the simulations and the corresponding correlations with the STARFiSh results provides useful insights in the performance of the lumped-hybrid model.

The reasons for why literature flow values can agree with the observed results in one coronary branch, but not in another, are multiple. First of all, coronary anatomy shows large inter-subject variability [19]. This means that this patient may have a well developed CX, bigger even than the LAD, to supply the back right wall of the heart, an area normally supplied by the RCA [8].

The segmentation procedure can also lead to significant errors in the vessel diamete. If the image gradients in the area of the RCA were to diffuse, the segmented vessel may have a lumen volume far below the real vessel's volume. As no expert consensus was sought in the segmentation process, and the open source software applied does not contain functions to draw lumen contours manually, this is not fully examined.

# Chapter 5

# Leaky Vessels

This chapter is based on the difference in number of outlets modelled from coronary arteries in state of the art simulations, such as Taylor et al [58], and the number of side branches visible on a angiogram, as the one in figure 1.2. The number of small arteries and arterioles branching off the main coronary arteries is confirmed by Kassab's *ex vivo* study [32], where a cast of polymers was injected into the coronary arteries of pigs. They then presented detailed data of segments and branches for the three main coronary arteries. For the RCA, they reported 44 small branches, while Taylor's study included 6 and 13 branches for the two cases presented, respectively. No simulation including more outlets than 13 was found, many of the examples demonstrated as late as in Secchi et al's 2016 review [53], uses 2 or 3 outlets for the right coronary artery, the same number used in the present work.

Thus, there exists many arterioles which are not seen on a CT-image, due to the limitation in image resulution, which for coronary CT typically lies around 1 mm. With this in mind, and the fact that the body has an autoregulation mechanism, which after Murray's law searches to minimize the energy consumption of the circulatory system by remodelling the arteries. The process of increasing arteriole size upstream of a stenosis is called collateralization. Patiens with high degree of collateral flow can able to maintain sufficient blood supply to the myocardium even with a severe stenosis in one of the main branches [13].

As shown in the earlier chapters, the pressure drop in a vessel segment or across a single stenose is highly dependant on the flow rate through the segment. For this reason, an investigation is made in this chapter on how to predict the correct flow rate in a vessel segment,

accounting for the outlets unseen from a normal resulution CT image. Then an effort has been made to model these losses in three dimensional simulations, and the results from these efforts are presented.

## 5.1 Flow Prediction from Murray's Law

In this section the LCA analyzed in chapter 4 is analyzed to find a prediction for the flow rate at all points in the vessel.By using Murrays law, and the autoregulation principled for remodeling blood vessels in the body, we can assume that a healthy blood vessel will adapt to the volumetric flow to keep the wall shear stress constant. This process takes from 10-14 days to complete after disturbances, according to van Royen et al. [65].

By Murray's law, the vessel will at all points have an optimal flow rate which ensures the correct wall shear stress level. However, as the flow exiting at branches goes off to supply the myocardium, we do not expect the collateral flow to reenter the vessel. With these limitations, we can search a flow distribution which minimizes the error from fulfilling Murray's law.

As the flow must be strictly decreasing in the arteries, higher order traditional regression will not give applicable results in stenotic regions. Instead, monotonic regression can be used. monotonic regression is a bounded regression, finding a least-squares fit $\mathbf{x}$ to a vector $\mathbf{a}$, subject to the condition that $x_i \leq x_j$ for $i < j$. The problem can be stated formally as:

$$\min \sum_{i=1}^{n} w_i (x_i - a_i)^2, \;\; x_i \leq x_j \text{ for all } i < j \tag{5.1}$$

where $w_i$ are strictly positive weights. We obtain the problem formulation for a decreasing fit by turning one of the the inequality signs in Eq. (5.1).

Note that the shape of $\mathbf{x}$ is aribitrary, as we do not assume anything about the functional relationship between $\mathbf{x}$ and the spatial coordinate.

By finding the ideal flow at each vessel segment, to fulfill the hypothesis of constant walls shear stress, we can now rule out the unphysical refilling of the vessel downstream, by performing a strictly decreasing regression. The Python library `scikit-learn` contais an implementa-

tion of the above described problem, using a method described by Chakravarti [9]. The result of such an analysis is shown in figure **??**. A flow of 120 ml/min was prescribed at the inlet, and the mean radius of the first 5 mm of the vessel was used to find the proportionality constant in Murray's law, equivalent to say that the tissue in the first part of the RCA is healthy, and remodelled to a optimal shear stress.

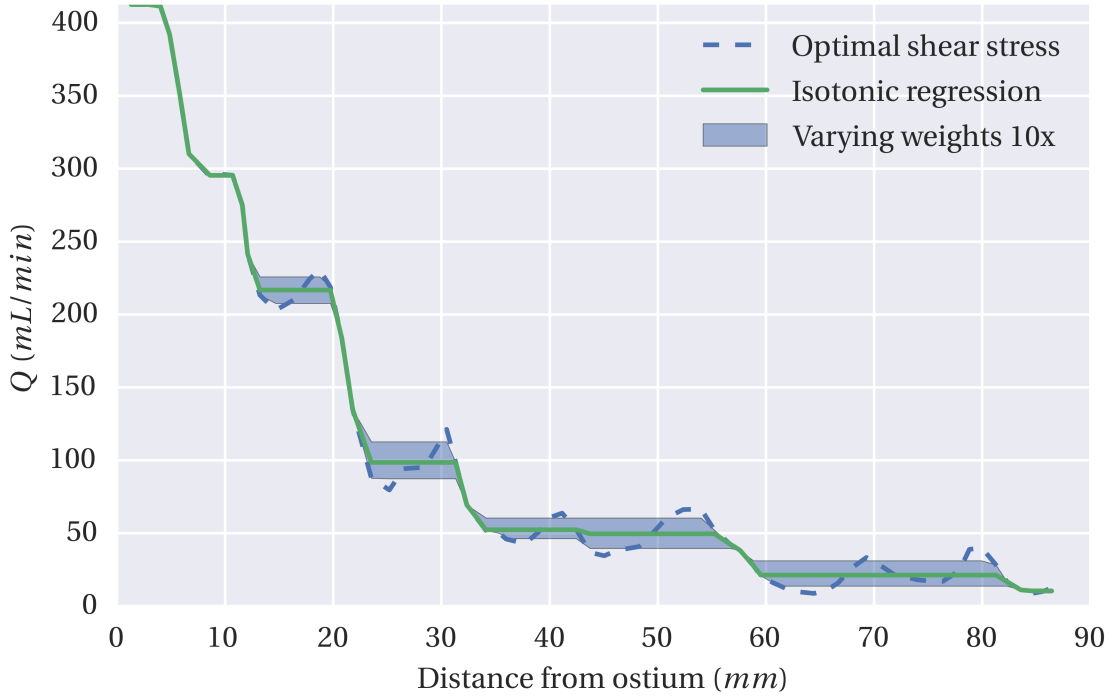


Figure 5.1: Predicted flow in the LCA

Looking at Murray's original derivation of his law, one would predict that the sensitivity to increased flow or increased diameter for an originally tuned vessel would not be the same. Therefore, one can imagine assigning weights to the isotonic regression, to pay closer attention to the regions where the wall shear stress is too high or regions where the vessel diameter is too big. Weighting the cost of maintaining vessel tissue and blood volume ten times higher than pumping power, and weighting the pumping power ten times more than the metabolic power requirement, alters the flow prediction very little.

For the prescribed incoming flow of 412.5 ml/min, about half of it is expected to be gone after 30 mm of the vessel, just where the CX artery branches off. The flow prediction made here can

Table 5.1: Summary of parameters for the straight pipe cases tested in OpenFOAM. All cases shared the same mesh dimensions from the text.

| Case number: | 1 | 2 | 3 | 4 |
|---|---|---|---|---|
| Inlet mean velocity (m/s) | 0.03 | 0.03 | 0.03 | 0.03 |
| Cross flow velocity (m/s) | 4e-4 | 2e-4 | 1e-4 | 5e-5 |
| Wall Reynolds' number, $Re_t$ | 0.08 | 0.038 | 0.019 | 0.0095 |
| Leak fraction (%) | 69.7 | 34.8 | 17.4 | 8.7 |

therefore justify the flow rate division specified in chapter 4. At the point of the significant stenosis identified in section **??**, the predicted flow rate is only about 25 % of the flow rate specified for the non-leaking case. This will change a FFR prediction dramatically, with the non-linearity of the pressure-flow relation confirmed in section 3.2.1 in mind.

## 5.2 Three-dimensional Modeling of Leaks

In this section, different boundary conditions for leaky vessels are tested for a straight pipe section, corresponding to the unobstructed test section from Young and Tsai. The pipe has a radius $r = 9.45$mm, and a length $L = 250$mm. For this mesh a structured grid was generated, consisting of 570 000 hexahedral cells, skewed towards the pipe wall and with a uniform grid in the cell core to avoid singularities.

The pipe has dimensions slightly larger than normal coronary arteries, but the length to diameter ratio $L/D$ is of the same order of magnitude as in healthy coronary arteries [19].

### 5.2.1 Constant Wall-normal Velocity

One method to model the volumetric loss is to prescribe a wall normal velocity at the vessel wall. This is easily accomplished in most existing CFD codes.

When modelling a pipe with a constant wall normal velocity, analytic solutions exists for validation. The most famous is Berman's solution, but also Karode has presented a variation, as outlined in section 5.2.1. A Reynolds number of 175 is chosen to be representative for flow in the coronary arteries at rest, leading to a mean velocity of the pipe of 0.03 m/s, considering blood viscosity to be $\mu = 3.3 \cdot 10^{-3}$. A summary of the different boundary conditions can be found in table 5.1.

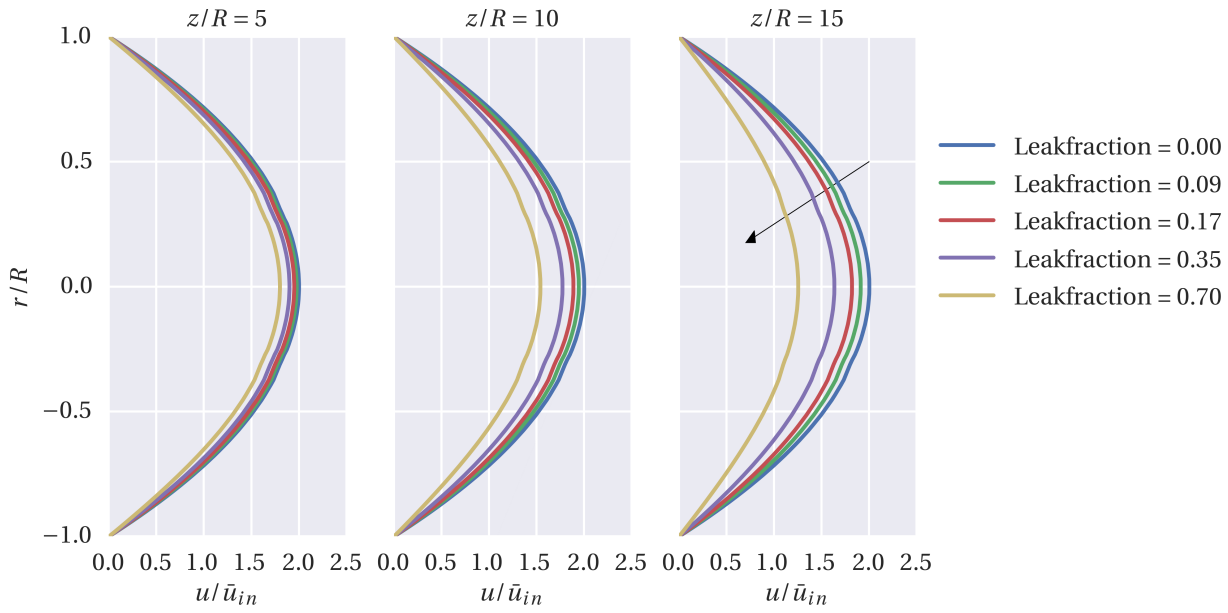


Figure 5.2: Axial velocity profiles at different streamwise locations, for different leakfractions. Velocities are normalized to the inlet mean velocity.

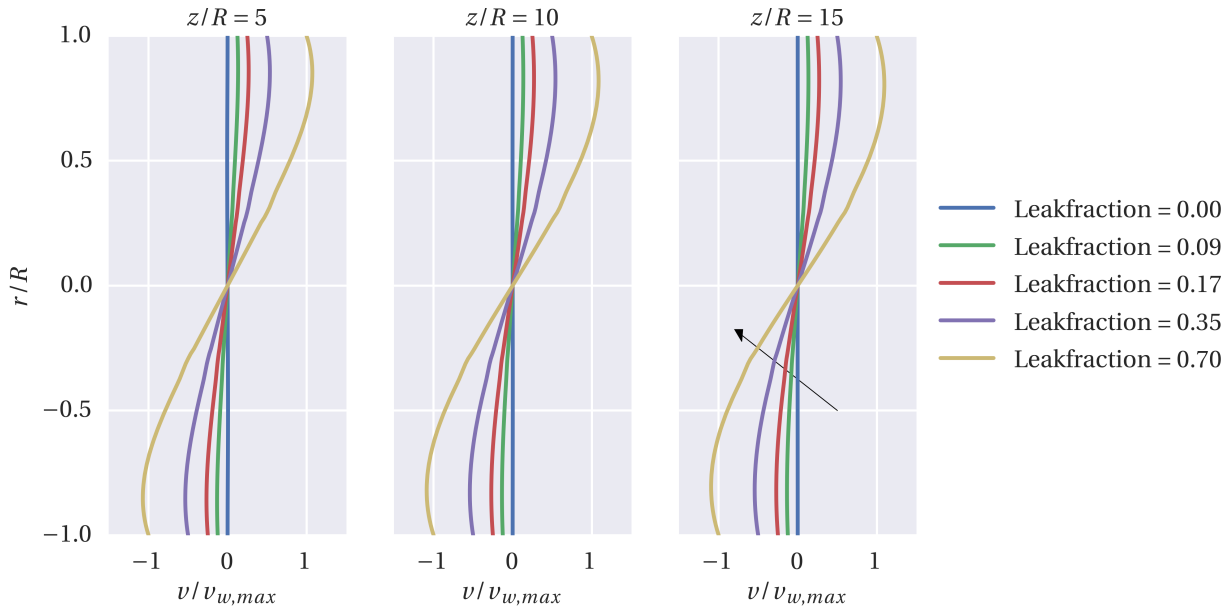


Figure 5.3: Radial velocity along diameter lines at 3 different streamwise locations, normalized to the maximum prescribed radial wall velocity, $v_w = 0.04$ mm/s.

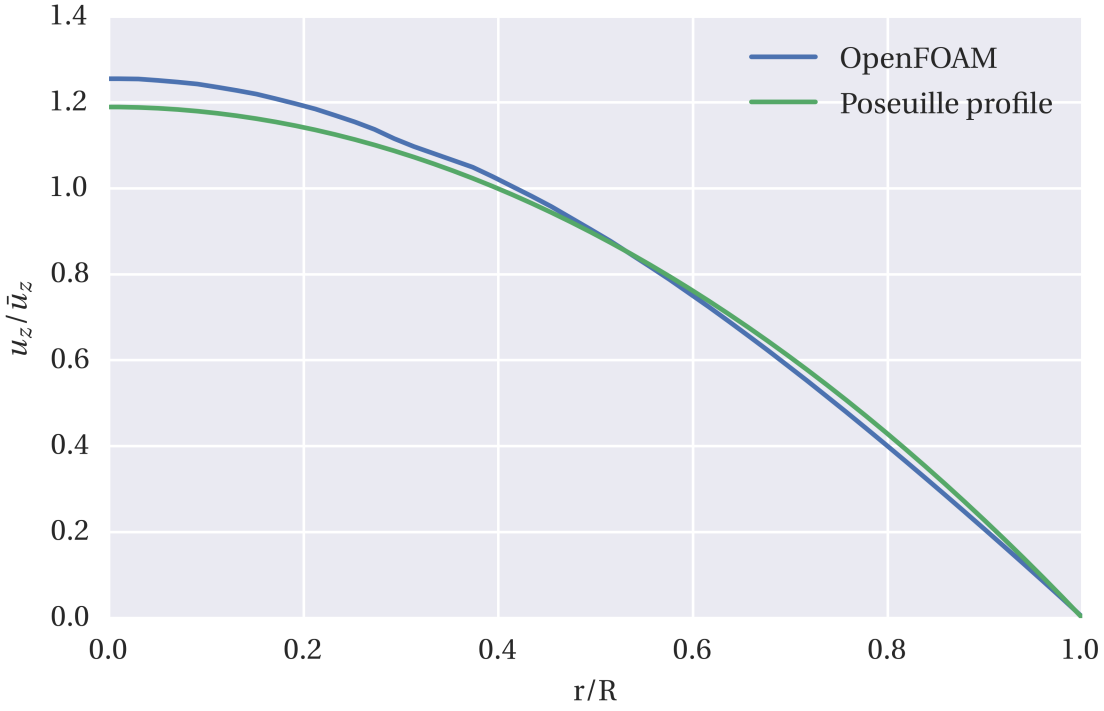


Figure 5.4: Velocity profile for highest leakfraction at $z/R = 10$. A Poseuille profile for a similar flow rate is plotted for reference.

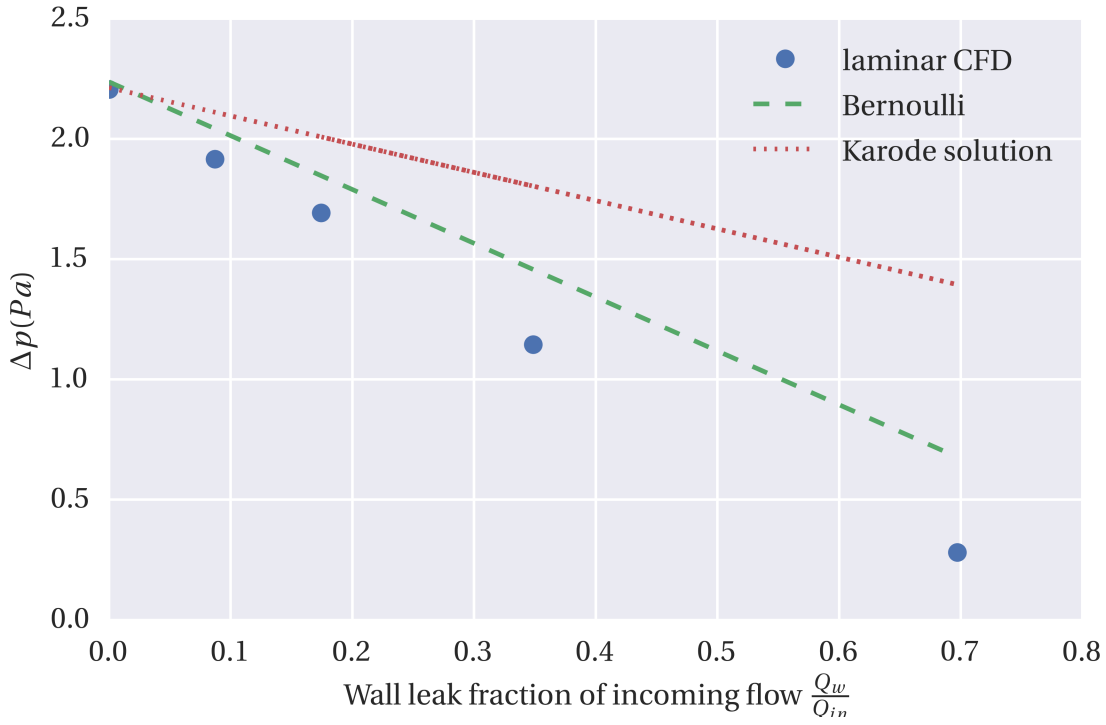


Figure 5.5: Pressure loss over entire pipe for different leakages, specified as constant velocity leaks. Compared with Karode's analytical solution, and the Poseuille pressure drop for a constant flow rate equal the mean flowrate in the pipe.

The pressure loss over the enitire pipe section is plotted in figure **??**. The simulation results are compared to the analytical solution presented by Karode, and given in equation 2.57. The Poseuille pressure drop for the mean flow is also shown. From the figure, we note a significantly lower pressure drop than the Poseuille drop with mean flow. This can be explained by the deceleration of the incoming flow, where dynamic pressure is converted to static pressure.

Figure 5.2 show the axial deceleration of the flow at three streamwise locations. The deceleration is more severe for higher leak fractions, as expected. In figure 5.3, the radial velocities are plotted at the same cross sections. Here we see how the velocity increases from the center of the pipe. An examination of the velocityprofile for the extreme case of a leakfraction of 0.7 is shown in figure **??**, and compared to a Poseuille profile for the same flow rate. From this image it is clear that the profile alters very little, and this suggests that the perturbation method proposed by Karode, shown in section , can be used, without violating the assumption of a parabolic profile. However, the pressure losses did not coincide with the theory proposed. One reason for this can be the inlet conditions, where velocity only in the axial direction is specified, causing the flow to develop its radial components.

### 5.2.2 Pressure-dependent Leaks as Boundary Conditions

A more sophisticated way of modelling the outflow from the small arterioles and arteries not visible on a CT-image, would be a pressure dependent outflow. This will reduce the flow through the artery to a flow through a pipe with porous walls, were the radial flow is a function of the pressure difference across the pipe. Such a model would incorporate some of the body's autoragulation mechanism, with higher collataralization rates proximally of a stenosis, and nearly no arterioles forming downstream of a stenosis, where the vessel is larger than optimal for the flowrate.

When solving CFD problems, as the incompressible Navier Stokes equations 2.20 only depends on pressure gradients, not the value itself, it is customary to assign a 0 pressure condition at the outlet of the domain. Thus, in the following analysis, a pressure driven outflow is prescribed at the boundary, with the pressure difference between the local pressure and the distal downstream pressure. In the body, the proximal pressure would be constant, the diastolic blood pressure, but the pressure downstream of a stenosis would be lower. Thus, This BC applies a vol-

umetric outflow through the vessel wall as a function of the local pressure versus the pressure drop for the entire segment, and as the outflow velocity is calculated, the volumetric outflow does also depend on the vessel perimeter at the site.

The boundary condition with a pressure dependent leakage was modeled in two ways in OpenFOAM. However, the simulations performed were only able to converge for very small values of the permeability, yielding leakfractions of less than 1 % over the entire pipe length. Different measures were taken to increase convergence

- The mesh was refined to a final resolution of 4 million hexahedral cells.
- Impermeable walls were specified near the inlet and the outlet.
- The permeability was ramped in time, using an exponential functional.
- Different solvers were applied, where memory allowed it, a coupled solver that solves for all three velocity components was employed, without improvements.
- A converged solution for a small permeability value was used as the initial condition.

By inspection of the residuals, the continuity equation seemed to be the cause of the trouble. A few cells near the pipe walls takes extreme values of radial outflow. This challenge was not fully overcome.

## Summary and Discussion

In this chapter, flow rate in a single segmented vessel segment was estimated, accounting for small unseen outlets, and using Murray's law. For the LAD segment analyzed, and assuming that the overall remodeling of the artery fulfilled the Murray corollary of constant shears stress, a significant flow rate decrease of 80 % of the incoming flow rate was estimated at the point of the significant stenosis.

Efforts to model leaks in 3D CFD simulations were taken. A straight pipe case was set up with wall constant normal velocity and compared to analytical solution from literature. The velocity profiles showed very little deviations from the Poseuille velocity profile even at severe

leaks. However, the pressure drop in the leaky pipe did not coincide with the analytical solution. This can be due to the high leak fractions and short pipe lengths considered here. For validating his analytical solution, Karode performed CFD on channels with $L/h = 5000$, with $L$ being the channel length and $h$ the channel height.

For the pressure dependent leaks, no convergence was obtained for physiologically significant leak values. This could have been investigated further, maybe simplifying the problem to a 2D axisymmetrical simulation, allowing for further mesh refinements in the critical regions without increasing computational times.

The general coupling of Darcy's membrane law to the Navier-Stokes equations for numerical simulations is not straightforward. Nassehi [44] blames the absence of second derivatives in Darcy's law to cause nonlinearities, and reports problems of finding unique solutions for high porosity values. The pressure correction in section 2.1.3 is violated by the direct coupling of pressure gradient to velocity. In particular, in the case of specifying the wall penetrating velocity as a boundary condition, this can violate the continuity equation. Means to deal with this includes adding a second derivative to Darcy's equation, as

$$\frac{\partial p}{\partial x} = -\frac{\mu}{k}q - \frac{\rho}{k_1}q^2 \tag{5.2}$$

where $k_1$ is known as the inertial permeability, as the latter term on the right hand side is included to capture inertial effects for high leak fractions. Equation 5.2 is called the Darcy-Forchheimer law [23]. Other Authors, including Terrill and Thomas [59] does also report dual solutions for higher cross flow Reynolds' numbers.

# Chapter 6

# Summary and Recommendations for Further Work

In this chapter, a brief summary of the main results will be given. Then the validity and the strengths and weaknesses in the methodology applied will be discussed, before suggestions for further work are presented.

## 6.1 Summary and Conclusions

The overall goal of comparing one- and three-dimensional simulations was approached by investigating both generic and patient specific geometries. In Chapter 3, the pressure loss over an idealized constriction was investigated in both 1D and 3D. For mild constrictions, with an area reduction of 56 %, the one-dimensional model performed well for Re<500. For a more severe stenosis of 89 % area reduction, or higher Reynolds' numbers for the 56 % stenosis, the pressure drop was severely underestimated by the one-dimensional analysis. A lumped model for stenotic pressure loss was added to the one-dimensional model. This was done in the equations linking together vessel segments in the network solver. With this simple lumped model, the pressure loss predictions from the new hybrid model were within 1 % from experimental data. Three-dimensional CFD analysis with mesh resolutions up to 1.5 million cells provided an equally good correlation with experimental data.

In Chapter 4, the same three simulation methodologies was applied to all main coronary

arterial branches of a 68 year old male subject. For the LAD, a measured ground truth was known a priori, and flow rates was varied to give a FFR prediction in agreement with the measurement. This was found at a flow rate of 200 ml/min in the LAD main branch, corresponding to three times the resting flow rate. This was in good agreement with the average flow conditions found in the literature.

For the RCA analyzed, literature flow values did not provide realistic FFR values, and lower flow rates were used to give FFR values in the range typically seen in CT-FFR cases [40].

Chapter 5 investigated the effect of small arterial branches unseen on a CT-image. Flow predictions were done on the LAD analyzed in Chapter 4. With the assumption of arterial remodeling to adapt to a constant wall shear stress, a flow rate reduction in the LAD equal to more than 50 % of the flow rate in the non-leaking case was found, by a minimizing the error of Murray's law for the entire segment. This prediction showed very little sensitivity to both terms in the energy function that was minimized.

In the same chapter, efforts were taken to model these unseen outlets as continuous wall perforating velocities in 3D CFD. A modeling approach based on the pressure difference across the arterial wall was undertaken, but did not yield stable solutions for physiologically relevant leaks. A simpler approach of modeling leaks as constant wall-normal velocity was shown, and radial and axial velocity profiles examined for various cases. Even for severe leaks did the velocity profile differ very little from the Poseuille profile, indicating that a one-dimensional approach including sink terms in the solver can be appropriate while assuming Poseuille profiles in all nodes.

## 6.2 Discussion

The main limitations of the results in Chapter 3 are the violation of the laminar flow hypothesis for the high Reynolds' cases, and the temporal averaging of the transient solution. However, as extensive experimental data was available, and the simulation results wheren in close agreement with the experiments, the approach can be justified.

The implementation of the simple lumped model in STARFiSh has not been validated for the conservation of propagating characteristics, only for pressure losses across stenoses at steady

state simulations, where the agreement with experiments was prominent. This is off course no surprise, as the lumped model itself is based on correlations for the experimental data. However, the closely correlated simulation results do validate the implementation of the model, and that the fundamental properties of the model is conserved in the implementation.

As the experimental results for the generic stenoses were reported with rigid walls and water, which behaves as a Newtonian fluid in this setting, no significant error was induced by also specifying these properties in the simulations.

In Chapter 4, the Newtonian assumption is subject to more debate, as the measured FFR prediction is made for blood as it behaves in reality. The Newtonian assumption is however reasonable in larger arteries, where the Reynolds' number is above 100 [10].

Only steady state simulations are performed for the patient specific geometries. The commercially available CT-FFR solution from HeartFlow inc uses transient simulations to simulate entire cardiac heart cycles. However, as FFR is measured in the period of the diastole where the pressure and flow is the most constant in the heart cycle, a steady approach can be feasible [29, 30]. As the technology behind the soon commercially Siemens CT-FFR software is not fully known, it is not certain whether steady state or transient simulations are performed here, but it is reported by [17] that their model uses a combination of reduced order models and 3D CFD for problematic regions.

The flow rates found in literature agreed very well with the measured FFR value in the LAD, indicating that the vasodilation response can be normal for this vessel. This was not the case with the RCA. The reasons for the disagreement between the estimated flow rate and the one giving adequate FFR values can be segmentation errors, that will constantly give to small lumen volume in the region of the RCA. Anatomical factors can also have a significance, as the size relationship between coronary arteries can have large inter-subject variations [19]. The effects of unseen outlets can also interfere with these results, as including leaks would lead to lower flow rate across the stenoses, leading to a lower pressure drop and a higher FFR value for a given incoming flow rate.

The segmentation itself is not only a source of error for the flow rates, but also for the flow field calculated, as the reconstruction of the vascular segments are prone to operator characteristics and errors. Small geometrical features can alter the flow significantly. No expert consen-

sus was sougth in determining the lumen boundaries, and the software applied does not allow manual drawing of the lumen border. This makes it unclear how well the lumen boundaries are estimated. However, the vessel diameters are in agreement with values reported in the literature, but as the pressure drop is very sensitive to the lumen diameter, the correctness of the segmentation can not be fully validated.

As a part of the "KoronarFlow" project, students at the Department of Computer and Information Science have worked on an automated segmentation algorithm. Tests compairing the automated segmentation to the semi-automated segmentation performed in this study were initiated, but the results not yet obtained.

The importance of the assumption of rigid walls on the pressure field in steady state simulations are assumed to be small, supported by results from FSI-simulations of coronary arteries [38]. They found significance for the shear stress, but this is a differentiated quantity, while the pressure is a primary variable.

For the configuration of the hybrid and the one-dimensional model in Chapter 4, the diameter at the centerline was taken to be two times the radius of the maximum sized inscribed sphere. This is a simple approach, which does not account very well for eccentricity and smaller plaques. A more novel approach would be to calculate the cross sectional area and the circumfrence of the vessel in planes normal to the centerline tangent vector, and calculate the hydraulic diameter from this data, or use the areas directly in the one-dimensional approach. As STARFiSh assumes circular cross sections, this will be equivalent.

A more novel approach could have been taken in the stenosis detection. Using data from healthy tapered vessels to create cone-like shapes of the healthy segments. Linear interpolation of the viscous constant is a simplification. Little theory was however found in the literature concerning the extraction of reduced order parameters from CT images. As solutions are reported to use this methodology, as the Siemens CT-FFR software, it will be very valuable to see a published scientific basis for their solution. However, using the method, good agreement was found for the flow in the LAD, both with the purely one-dimensional model for resting flow conditions, and with the hybrid model at the flow rates resembling hyperemic flow conditions.

For the chapter with leaky vessels, more actions could have been taken to stabilize the pressure driven outflow. Maybe could the problem been reduced to 2D for proofing the concept,

to allow for faster computation of high resolution meshes. The constant outflow could have been tested on the patient specific geometry, and flow rates measured along the centerline and compared to the results of the Murray flow prediction.

## 6.3 Recommendations for Further Work

Based on the findings in the present work, there are several directions worth exploring in the future. The most obvious is building further on the good FFR prediction developed by the simple lumped model proposed. This model can be refined in various ways. As it is implemented in a network solver, a natural extension would be to couple the lumped model with the possibility to read vessel geometries from files, allowing to create a network of patient specific vessels, separated by stenosis lumped models or ordinary junctions where applicable.

The stenosis model can then be refined, to a more advanced model utilizing more geometric parameters of the stenosis. Huo et al. [28] proposed an example of an advanced stenosis model based on 1D boundary layer theory, without empirical constants.

Introducing transient simulations with wave reflections and compliant walls can have significance for the predictions. It is also worth noticing that STARFiSh contains framework for simulations with stochastic distributed parameters. Thus, the sensistivity to segmentation errors or flow assumptions can be analyzed, and a confidence interval for a predicted FFR value established.

Looking a bit further, the exact flow rates in the coronary arteries at hyperemia are a unknown factor with a huge impact on the FFR computations. At least two different paths can be taken. One is to create models for the body's response to vasodilation. This can be done by estimating the volume of tissue supplied from an artery, or from measurements of gradients of contrast agent in the lumen volume, as in TAG. Another possibility is to use ultrasound. Although not feasible in large scale screening today, the St. Olavs university reported succesful measurements of flow velocities in coronary arteries using trans-thoracic doppler ultrasound during the work with this thesis. Unfortunately, this data was not available in time to be used in this thesis, but should form the basis for later work.

From the findings in the first part of chapter 5, it was shown that the flow rate may decrease

significantly in a vessel segment reconstructed from a normal resolution CT image. To quantify these leaks would mean vast improvements in the prediction quality of CT-FFR. To quantify those leaks, more advanced studies, either based on Murray's law, or on measured flow data at multiple locations in the same artery are needed.

If such a quantification is done, variable location sink terms can be included in the 1D code STARFiSh to account for these losses.

# Bibliography


[1] Luca Antiga. Patient-specific modeling of geometry and blood flow in large arteries. *Politecnico di Milano*, 2002.

[2] Luca Antiga, Marina Piccinelli, Lorenzo Botti, Bogdan Ene-Iordache, Andrea Remuzzi, and David A Steinman. An image-based modeling framework for patient-specific computational hemodynamics. *Medical & biological engineering & computing*, 46(11):1097–1112, 2008.

[3] Karim Azer and Charles S Peskin. A one-dimensional model of blood flow in arteries with friction and convection based on the womersley velocity profile. *Cardiovascular Engineering*, 7(2):51–73, 2007.

[4] LH Back and EJ Roschke. Shear-layer flow regimes and wave instabilities and reattachment lengths downstream of an abrupt circular channel expansion. *Journal of Applied Mechanics*, 39(3):677–681, 1972.

[5] Abraham S Berman. Laminar flow in channels with porous walls. *Journal of Applied physics*, 24(9):1232–1235, 1953.

[6] Colin Berry, Kanarath P Balachandran, Philippe L L'Allier, Jacques Lespérance, Raoul Bonan, and Keith G Oldroyd. Importance of collateral circulation in coronary heart disease. *European heart journal*, 28(3):278–291, 2007.

[7] David Bessems, Marcel Rutten, and Frans Van De Vosse. A wave propagation model of blood flow in large vessels using an approximate velocity profile function. *Journal of Fluid Mechanics*, 580:145–168, 2007.

[8] J Gordon Betts, Peter DeSaix, Eddie Johnson, and Jody E Johnson. *Anatomy and Physiology*. OpenStax College, 2013.

[9] Nilotpal Chakravarti. Isotonic median regression: a linear programming approach. *Mathematics of operations research*, 14(2):303–308, 1989.

[10] Young I Cho and Kenneth R Kensey. Effects of the non-newtonian viscosity of blood on flows in a diseased arterial vessel. part 1: Steady flows. *Biorheology*, 28(3-4):241–262, 1991.

[11] Jin-Ho Choi, James K Min, Troy M Labounty, Fay Y Lin, Dorinna D Mendoza, Dae Hee Shin, Nikki S Ariaratnam, Sunaina Koduru, Juan F Granada, Thomas C Gerber, et al. Intracoronary transluminal attenuation gradient in coronary ct angiography for determining coronary artery stenosis. *JACC: Cardiovascular Imaging*, 4(11):1149–1157, 2011.

[12] Adriaan Coenen, Marisa M Lubbers, Akira Kurata, Atsushi Kono, Admir Dedic, Raluca G Chelu, Marcel L Dijkshoorn, Frank J Gijsen, Mohamed Ouhlous, Robert-Jan M van Geuns, et al. Fractional flow reserve computed from noninvasive ct angiography data: diagnostic performance of an on-site clinician-operated computational fluid dynamics algorithm. *Radiology*, 274(3):674–683, 2014.

[13] MARC Cohen and K PETER Rentrop. Limitation of myocardial ischemia by collateral circulation during sudden controlled coronary artery occlusion in human subjects: a prospective study. *Circulation*, 74(3):469–476, 1986.

[14] Wikimedia Commons. Coronary arteries. Url: `https://upload.wikimedia.org/wikipedia/commons/9/93/Blausen_0256_CoronaryArteries_02.png`, 2013. Last visited: 31.03.2016.

[15] Richard Courant, Kurt Friedrichs, and Hans Lewy. Über die partiellen differenzengleichungen der mathematischen physik. *Mathematische Annalen*, 100(1):32–74, 1928.

[16] Bernard de Bruyne, Jozef Bartunek, Stanislas U Sys, Nico HJ Pijls, Guy R Heyndrickx, and William Wijns. Simultaneous coronary pressure and flow velocity measurements in humans feasibility, reproducibility, and hemodynamic dependence of coronary flow velocity

reserve, hyperemic flow versus pressure slope index, and fractional flow reserve. *Circulation*, 94(8):1842–1849, 1996.

[17] Jakob De Geer, Mårten Sandstedt, Anders Björkholm, Joakim Alfredsson, Magnus Janzon, Jan Engvall, and Anders Persson. Software-based on-site estimation of fractional flow reserve using standard coronary ct angiography data. *Acta Radiologica*, page 0284185115622075, 2015.

[18] Song-Bai Deng, Xiao-Dong Jing, Jing Wang, Chuan Huang, Shuang Xia, Jian-Lin Du, Ya-Jie Liu, and Qiang She. Diagnostic performance of noninvasive fractional flow reserve derived from coronary computed tomography angiography in coronary artery disease: A systematic review and meta-analysis. *International journal of cardiology*, 184:703–709, 2015.

[19] JT Dodge, B Greg Brown, Edward L Bolson, and Harold T Dodge. Lumen diameter of normal human coronary arteries. influence of age, sex, anatomic variation, and left ventricular hypertrophy or dilation. *Circulation*, 86(1):232–246, 1992.

[20] FM Ernsberger. Mechanical properties of glass. *Journal of Non-Crystalline Solids*, 25(1):293–321, 1977.

[21] FDA. Marketing grant HeartFlow inc. v1.4. `http://www.accessdata.fda.gov/cdrh_docs/reviews/DEN130045.pdf`, 2013.

[22] Joel H Ferziger and Milovan Peric. *Computational methods for fluid dynamics*. Springer Science & Business Media, 2012.

[23] Philipp Forchheimer. Wasserbewegung durch boden. *Z. Ver. Deutsch. Ing*, 45(1782):1788, 1901.

[24] Luca Formaggia, Daniele Lamponi, and Alfio Quarteroni. One-dimensional models for blood flow in arteries. *Journal of engineering mathematics*, 47(3-4):251–276, 2003.

[25] LS Galowin, LS Fletcher, and MJ DeSantis. Investigation of laminar flow in a porous pipe with variable wall suction. *AIAA Journal*, 12(11):1585–1589, 1974.

[26] TIMI Study Group et al. The thrombolysis in myocardial infarction (timi) trial: phase i findings. *N. Engl. J. Med.*, 312:932–936, 1985.

[27] Godfrey Newbold Hounsfield. Method of and apparatus for examining a body by radiation such as x or gamma radiation. Technical report, 1975.

[28] Yunlong Huo, Mark Svendsen, Jenny Susana Choy, Z-D Zhang, and Ghassan S Kassab. A validated predictive model of coronary fractional flow reserve. *Journal of The Royal Society Interface*, 9(71):1325–1338, 2012.

[29] Barbara M Johnston, Peter R Johnston, Stuart Corney, and David Kilpatrick. Non-newtonian blood flow in human right coronary arteries: steady state simulations. *Journal of biomechanics*, 37(5):709–720, 2004.

[30] Barbara M Johnston, Peter R Johnston, Stuart Corney, and David Kilpatrick. Non-newtonian blood flow in human right coronary arteries: transient simulations. *Journal of biomechanics*, 39(6):1116–1128, 2006.

[31] Sandeep K Karode. Laminar flow in channels with porous walls, revisited. *Journal of Membrane Science*, 191(1):237–241, 2001.

[32] Ghassan S Kassab, Carmela A Rider, Nina J Tang, and Yuan-Cheng Fung. Morphometry of pig coronary arterial trees. *American Journal of Physiology-Heart and Circulatory Physiology*, 265(1):H350–H365, 1993.

[33] RR Kerswell. Recent progress in understanding the transition to turbulence in a pipe. *Nonlinearity*, 18(6):R17, 2005.

[34] Ahmed Khashaba, Ayman Mortada, and Azza Omran. Intracoronary versus intravenous adenosine-induced maximal coronary hyperemia for fractional flow reserve measurements. *Clinical Medicine Insights. Cardiology*, 8:17, 2014.

[35] Bon-Kwon Koo, Andrejs Erglis, Joon-Hyung Doh, David V Daniels, Sanda Jegere, Hyo-Soo Kim, Allison Dunning, Tony DeFrance, Alexandra Lansky, Jonathan Leipsic, et al. Diagnosis of ischemia-causing coronary stenoses by noninvasive fractional flow reserve computed

from coronary computed tomographic angiograms: results from the prospective multicenter discover-flow (diagnosis of ischemia-causing stenoses obtained via noninvasive fractional flow reserve) study. *Journal of the American College of Cardiology*, 58(19):1989–1997, 2011.

[36] Jen-shih Lee and Yuan-cheng Fung. Flow in nonuniform small blood vessels. *Microvascular Research*, 3(3):272–287, 1971.

[37] Antonio Maria Leone, Italo Porto, Alberto Ranieri De Caterina, Eloisa Basile, Andrea Aurelio, Andrea Gardi, Dolores Russo, Domenico Laezza, Giampaolo Niccoli, Francesco Burzotta, et al. Maximal hyperemia in the assessment of fractional flow reserve: intracoronary adenosine versus intracoronary sodium nitroprusside versus intravenous adenosine: the nasci (nitroprussiato versus adenosina nelle stenosi coronariche intermedie) study. *JACC: Cardiovascular Interventions*, 5(4):402–408, 2012.

[38] M Malvè, A García, J Ohayon, and MA Martínez. Unsteady blood flow and mass transfer of a human left coronary artery bifurcation: Fsi vs. cfd. *International communications in heat and mass transfer*, 39(6):745–751, 2012.

[39] John McMichael and EP Sharpey-Schafer. Cardiac output in man by a direct fick method: Effects of posture, venous pressure change, atropine, and adrenaline. *British heart journal*, 6(1):33, 1944.

[40] James K Min, Jonathon Leipsic, Michael J Pencina, Daniel S Berman, Bon-Kwon Koo, Carlos van Mieghem, Andrejs Erglis, Fay Y Lin, Allison M Dunning, Patricia Apruzzese, et al. Diagnostic accuracy of fractional flow reserve from anatomic ct angiography. *Jama*, 308(12):1237–1245, 2012.

[41] Paul D Morris, Desmond Ryan, Allison C Morton, Richard Lycett, Patricia V Lawford, D Rodney Hose, and Julian P Gunn. Virtual fractional flow reserve from coronary angiography: modeling the significance of coronary lesions: results from the virtu-1 (virtual fractional flow reserve from coronary angiography) study. *JACC: Cardiovascular Interventions*, 6(2):149–157, 2013.

[42] SL Murphy, J Xu, KD Kochanek, and BA Bastian. Deaths: Final data for 2013. *National vital statistics reports: from the Centers for Disease Control and Prevention, National Center for Health Statistics, National Vital Statistics System*, 64(2):1–119, 2016.

[43] Cecil D Murray. The physiological principle of minimum work i. the vascular system and the cost of blood volume. *Proceedings of the National Academy of Sciences*, 12(3):207–214, 1926.

[44] V Nassehi. Modelling of combined navier–stokes and darcy flows in crossflow membrane filtration. *Chemical Engineering Science*, 53(6):1253–1265, 1998.

[45] Bjarne L Nørgaard, Jonathon Leipsic, Sara Gaur, Sujith Seneviratne, Brian S Ko, Hiroshi Ito, Jesper M Jensen, Laura Mauri, Bernard De Bruyne, Hiram Bezerra, et al. Diagnostic performance of noninvasive fractional flow reserve derived from coronary computed tomography angiography in suspected coronary artery disease: the nxt trial (analysis of coronary blood flow using ct angiography: Next steps). *Journal of the American College of Cardiology*, 63(12):1145–1155, 2014.

[46] Suhas V Patankar and D Brian Spalding. A calculation procedure for heat, mass and momentum transfer in three-dimensional parabolic flows. *International journal of heat and mass transfer*, 15(10):1787–1806, 1972.

[47] Nico HJ Pijls, Bernard de Bruyne, Kathinka Peels, Pepijn H van der Voort, Hans JRM Bonnier, Jozef Bartunek, and Jacques J Koolen. Measurement of fractional flow reserve to assess the functional severity of coronary-artery stenoses. *New England Journal of Medicine*, 334(26):1703–1708, 1996.

[48] Nico HJ Pijls, William F Fearon, Pim AL Tonino, Uwe Siebert, Fumiaki Ikeno, Bernhard Bornschein, Marcel van't Veer, Volker Klauss, Ganesh Manoharan, Thomas Engstrøm, et al. Fractional flow reserve versus angiography for guiding percutaneous coronary intervention in patients with multivessel coronary artery disease: 2-year follow-up of the fame (fractional flow reserve versus angiography for multivessel evaluation) study. *Journal of the American College of Cardiology*, 56(3):177–184, 2010.

[49] Tamilselvi Ramanathan and Henry Skinner. Coronary blood flow. *Continuing Education in Anaesthesia, Critical Care & Pain*, 5(2):61–64, 2005.

[50] Matthias Renker, U Joseph Schoepf, Rui Wang, Felix G Meinel, Jeremy D Rier, Richard R Bayer, Helge Möllmann, Christian W Hamm, Daniel H Steinberg, and Stefan Baumann. Comparison of diagnostic value of a novel noninvasive coronary computed tomography angiography method versus standard coronary angiography for assessing fractional flow reserve. *The American journal of cardiology*, 114(9):1303–1308, 2014.

[51] O Reynolds. Papers on mechanical and physical subjects, by osborne reynolds reprinted from various transactions and journals. vol. 1, 1900.

[52] Richard S Ross, Keiji Ueda, PAUL R LICHTLEN, J Russell Rees, Redden Redden, and Christa Kaelber. Measurement of myocardial blood flow in animals and man by selective injection of radioactive inert gas into the coronary arteries. *Circulation research*, 15(1):28–41, 1964.

[53] Francesco Secchi, Marco Alì, Elena Faggiano, Paola Maria Cannaò, Marco Fedele, Silvia Tresoldi, Giovanni Di Leo, Ferdinando Auricchio, and Francesco Sardanelli. Fractional flow reserve based on computed tomography: an overview. *European Heart Journal Supplements*, 18(suppl E):E49–E56, 2016.

[54] Thomas F Sherman. On connecting large vessels to small. the meaning of murray's law. *The Journal of general physiology*, 78(4):431–453, 1981.

[55] SJ Sherwin, V Franke, J Peiró, and K Parker. One-dimensional modelling of a vascular network in space-time variables. *Journal of Engineering Mathematics*, 47(3-4):217–250, 2003.

[56] Michael L Steigner, Dimitrios Mitsouras, Amanda G Whitmore, Hansel J Otero, Chunliang Wang, Orla Buckley, Noah A Levit, Alia Z Hussain, Tianxi Cai, Richard T Mather, et al. Iodinated contrast opacification gradients in normal coronary arteries imaged with prospectively ecg-gated single heart beat 320-detector row computed tomography. *Circulation: Cardiovascular Imaging*, 3(2):179–186, 2010.

[57] JC Stettler, P Niederer, and M Anliker. Theoretical analysis of arterial hemodynamics including the influence of bifurcations. *Annals of biomedical engineering*, 9(2):145–164, 1981.

[58] Charles A Taylor, Timothy A Fonte, and James K Min. Computational fluid dynamics applied to cardiac computed tomography for noninvasive quantification of fractional flow reserve: scientific basis. *Journal of the American College of Cardiology*, 61(22):2233–2241, 2013.

[59] RM Terrill and PW Thomas. On laminar flow through a uniformly porous pipe. *Applied Scientific Research*, 21(1):37–67, 1969.

[60] Pim AL Tonino, Bernard De Bruyne, Nico HJ Pijls, Uwe Siebert, Fumiaki Ikeno, Marcel vant Veer, Volker Klauss, Ganesh Manoharan, Thomas Engstrøm, Keith G Oldroyd, et al. Fractional flow reserve versus angiography for guiding percutaneous coronary intervention. *New England Journal of Medicine*, 360(3):213–224, 2009.

[61] Ryo Torii, Nigel B Wood, Nearchos Hadjiloizou, Andrew W Dowsey, Andrew R Wright, Alun D Hughes, Justin Davies, Darrel P Francis, Jamil Mayet, Guang-Zhong Yang, et al. Fluid–structure interaction analysis of a patient-specific right coronary artery with physiological velocity and pressure waveforms. *Communications in numerical methods in engineering*, 25(5):565–580, 2009.

[62] Neal G Uren, Tom Crake, David C Lefroy, Ranil de Silva, Graham J Davies, and Attilio Maseri. Reduced coronary vasodilator function in infarcted and normal myocardium after myocardial infarction. *New England Journal of Medicine*, 331(4):222–227, 1994.

[63] Kristian Valen-Sendstad and DA Steinman. Mind the gap: impact of computational fluid dynamics solution strategy on prediction of intracranial aneurysm hemodynamics and rupture status indicators. *American Journal of Neuroradiology*, 35(3):536–543, 2014.

[64] Alina G Van der Giessen, Harald C Groen, Pierre-André Doriot, Pim J De Feyter, Antonius FW Van der Steen, Frans N Van de Vosse, Jolanda J Wentzel, and Frank JH Gijsen. The influence of boundary conditions on wall shear stress distribution in patients specific coronary trees. *Journal of biomechanics*, 44(6):1089–1095, 2011.

[65] Niels van Royen, Jan J Piek, Wolfgang Schaper, and William F Fulton. A critical review of

clinical arteriogenesis research. *Journal of the American College of Cardiology*, 55(1):17–25, 2009.

[66] Henk Kaarle Versteeg and Weeratunge Malalasekera. *An introduction to computational fluid dynamics: the finite volume method*. Pearson Education, 2007.

[67] VMTK. The Vascular Modelling Toolkit. `www.vmtk.org`, 2016.

[68] Henry G Weller, G Tabor, Hrvoje Jasak, and C Fureby. A tensorial approach to computational continuum mechanics using object-oriented techniques. *Computers in physics*, 12(6):620–631, 1998.

[69] World Health Organization (WHO et al. A global brief on hypertension: silent killer, global public health crisis. *World*, 2015.

[70] RF Wilson, K Wyche, BV Christensen, S Zimmer, and DD Laxson. Effects of adenosine on human coronary arterial circulation. *Circulation*, 82(5):1595–1606, 1990.

[71] CHRISTOPHER J Wolfkiel, JL Ferguson, EV Chomka, WR Law, IN Labin, ML Tenzer, M Booker, and BH Brundage. Measurement of myocardial blood flow by ultrafast computed tomography. *Circulation*, 76(6):1262–1273, 1987.

[72] Dennis T L. Wong, Brian S. Ko, James D. Cameron, Nitesh Nerlekar, Michael C H. Leung, Yuvaraj Malaiapan, Marcus Crossett, Darryl P. Leong, Stephen G. Worthley, John Troupis, Ian T. Meredith, and Sujith K. Seneviratne. Transluminal attenuation gradient in coronary computed tomography angiography is a novel noninvasive approach to the identification of functionally significant coronary artery stenosis: a comparison with fractional flow reserve. *J Am Coll Cardiol*, 61(12):1271–1279, Mar 2013.

[73] Roh-Eul Yoo, Eun-Ah Park, Whal Lee, Hackjoon Shim, Yeo Koon Kim, Jin Wook Chung, and Jae Hyung Park. Image quality of adaptive iterative dose reduction 3d of coronary ct angiography of 640-slice ct: comparison with filtered back-projection. *The international journal of cardiovascular imaging*, 29(3):669–676, 2013.

[74] Donald F Young and Frank Y Tsai. Flow characteristics in models of arterial stenoses. part i. steady flow. *Journal of biomechanics*, 6(4):395IN3403–402410, 1973.

[75] M Zamir. Optimality principles in arterial branching. *Journal of Theoretical Biology*, 62(1):227–251, 1976.

[76] M Zamir. The role of shear forces in arterial branching. *The Journal of general physiology*, 67(2):213–222, 1976.

[77] M Zamir. Shear forces and blood vessel radii in the cardiovascular system. *The Journal of general physiology*, 69(4):449–461, 1977.